



The University of
Nottingham

**Changes in Microstructure and
Mechanical Properties of P91 Weld
Metal during Creep**

Yan Zhang, BEng, MSc

**Thesis submitted to the University of Nottingham
for the degree of Doctor of Philosophy**

June, 2009

Contents	i
Abstract	v
Acknowledgements	vii
Abbreviations	viii
Chapter 1 Introduction	1
Chapter 2 Literature review	4
2.1 Development of power plant steels	4
2.2 P91 steels	8
2.2.1 Composition of P91 parent metal	8
2.2.2 Effect of alloying elements	8
2.2.3 Microstructural features of P91 steel	13
2.2.4 Characteristics of precipitates	17
2.3 P91 weld metal	21
2.3.1 Welding process for P91 pipework	21
2.3.2 Microstructural features of welds	23
2.3.2.1 <i>Heat-affected zone (HAZ)</i>	24
2.3.2.2 <i>Weld metal (WM)</i>	25
2.3.2.3 <i>Weld interface region</i>	26
2.3.3 Inhomogeneity of element distribution in welds	27
2.3.3.1 <i>Solidification of welds</i>	27
2.3.3.2 <i>Solute partition during weld solidification</i>	32
2.4 Creep properties of P91 and 9-12% chromium steels and welds	36
2.4.1 Introduction to creep	36
2.4.2 Evolution of microstructure and material properties during creep	39
2.4.2.1 <i>Precipitates</i>	39
2.4.2.2 <i>Recovery of martensite and dislocations</i>	41
2.4.2.3 <i>Softening / Hardness</i>	43
2.4.3 Creep failure mechanism of P91 welds	45
2.4.3.1 <i>Type IV cracking in ICHAZ</i>	46
2.4.3.2 <i>Type I weld metal failure</i>	48

2.4.3.3 <i>Type IIIa weld interface failure</i>	49
2.4.3.4 <i>Inter-bead boundary creep failure (weld bead to weld bead)</i>	52
2.4.4 Mechanism of carbon diffusion in dissimilar welds	53
2.4.5 Thermodynamic modelling of carbon diffusion in dissimilar welds	57
2.5 Summary	59
Chapter 3 Experimental work	60
3.1 Materials and weld preparation	60
3.1.1 SUPERGEN P91 MMA weld pad	60
3.1.2 P91 TIG weld	62
3.2 Creep tests of SUPERGEN P91 weld metal	64
3.3 Characterisation methods	65
3.3.1 Sample preparation	65
3.3.2 Optical microscopy	65
3.3.3 Micro-hardness measurement	65
3.3.4 Strain measurement of analysis	66
3.3.5 Scanning electron microscope (SEM)	67
3.3.6 Laser induced breakdown spectroscopy (LIBS)	68
3.3.7 Electron backscatter diffraction (EBSD)	69
3.3.8 Transmission electron microscopy (TEM)	70
3.3.8.1 <i>Sample preparation</i>	70
3.3.8.2 <i>TEM imaging and EDX</i>	71
3.3.8.3 <i>Selected area electron diffraction patterns (SADP)</i>	71
3.4 Modelling method	74
Chapter 4 Experimental results	76
4.1 Characterisation of P91 weld metal	76
4.1.1 Type M P91 weld rod	76
4.1.2 Microstructure features	77
4.1.3 Hardness	79
4.2 Characterisation of creep tested P91 weld metal	80
4.2.1 Anisotropic creep behaviour	80
4.2.2 Features of creep tested samples and the fracture surface	81
4.2.3 Features of creep fractures	83
4.2.4 Precipitates	88

4.2.5 Hardness and strain	90
4.3 Characterisation of white-bands in P91 weld metal	93
4.3.1 Microstructural features of white-bands	93
4.3.2 Precipitates	99
4.3.3 Hardness	105
4.3.4 Element distribution	107
4.3.4.1 EDX results	107
4.3.4.2 LIBS results	113
4.3.5 Development of white-bands by aging of as-welded P91 weld metal	116
4.3.6 Mechanism of white-band formation	119
4.4 Characterisation of the P91 TIG weld metal	121
Chapter 5 Modelling of white-band formation in P91 weld metal	129
5.1 Modelling of solute partition during P91 weld solidification	131
5.1.1 P91 phase content at different temperatures	131
5.1.2 Solute partition during weld solidification	131
5.2 Modelling of carbon diffusion out of the white-band regions	133
5.2.1 Modelling strategies	133
5.2.2 Carbon activity in P91 weld metal	134
5.2.3 Limiting carbon concentration in white-bands	138
5.2.4 Carbide precipitates	139
Chapter 6 Discussion	143
6.1 Microstructure and properties of P91 weld metal	145
6.1.1 Microstructural features	145
6.1.2 Hardness degradation	146
6.1.3 Precipitate coarsening	147
6.2 Creep fracture modes and their role in anisotropic creep behaviour of P91 weld metal	149
6.2.1 Creep fracture modes of p91 weld metal	149
6.2.2 Anisotropic creep behaviour of P91 weld metal	150
6.3 Mechanism of white-band formation	153
6.3.1 Features of white-bands	153

6.3.2	Inhomogeneity of alloying element distributions in as-welded state	154
6.3.2.1	<i>Poor mixing</i>	154
6.3.2.2	<i>Solute partition during weld solidification</i>	155
6.3.2.3	<i>Summary</i>	158
6.3.3	Carbon diffusion out of the alloy-depleted regions	158
6.4	Use of thermodynamic modelling to understand white-band formation	161
6.4.1	Solute partition during weld solidification of P91 weld metal	161
6.4.2	Parameters affecting the carbon activity in P91 weld metal	163
6.4.3	Carbon and carbide depletion in white-bands during heat exposure	165
6.4.4	Summary	167
Chapter 7 Conclusion		168
References		171

Abstract

Creep failure of the weld structure in P91 steel components in high temperature power plant applications is often a key factor limiting the lifetime of the components. Whilst creep failure in weld heat-affected zone (HAZ) regions has been studied widely, the creep properties of the weld metal itself have been less well documented. In this work, the creep response of P91 weld metal in isolation was investigated in terms of microstructural evolution and mechanical properties.

The microstructural examination of P91 multi-pass weld metal revealed a typical weld metal structure including columnar regions and refined regions. The columnar region exhibited high hardness whilst the refined region exhibited lower hardness. The anisotropic creep behaviour of P91 weld metal was observed in creep tests of both longitudinal and transverse specimens at 650°C and various stress levels. This behaviour can be correlated with the microstructural anisotropy observed, where longitudinal specimens with banded columnar regions and refined regions parallel to the stress axis had longer creep life than transverse specimens with overlapped typical-shape beads. Longitudinal weld specimens showed higher strain to failure than transverse specimens.

The microstructural investigation of creep tested P91 weld metal revealed two primary modes of creep fractures. In addition to creep fractures along columnar grain boundaries (typical of weld metal creep failure), creep fractures were also found along creep-weak white-bands which had formed at the inter-bead boundaries. The white-band regions consisted of material where the $M_{23}C_6$ carbides had dissolved during creep testing; the loss of carbides had allowed recrystallisation of the martensitic structure to ferrite and consequently this material was much softer than the bulk weld metal. The element mapping over the weld metal by laser-induced breakdown spectroscopy (LIBS) demonstrated that there was significant inhomogeneity in the distribution of certain elements, most significantly, chromium, manganese and molybdenum. This inhomogeneity resulted in strong activity gradients in carbon (even though the carbon concentration was homogeneous following welding) resulting in carbon loss from the alloy-depleted regions, the associated dissolution of carbides and the

recrystallisation that accompanied this, and thus the poor mechanical properties which resulted in creep failure.

The inhomogeneity in the distribution of certain alloying elements can be partially attributed to the solute partition of alloying elements during weld solidification which has been confirmed with examination of simulation P91 TIG welds. However, the homogeneity of weld metal in this case required mixing of a base steel (the core rod in the weld consumable) and particles of various ferro-alloys (delivered into the weld pool from the flux). It is argued that poor mixing in the stagnant layer (unmixed zone) at the solid-liquid interface during weld solidification also makes a significant contribution to the formation of alloy-depleted regions.

The formation of white-bands has been modelled using Thermo-Calc based on the understanding of the formation mechanism involving solute partition and subsequent carbon diffusion out of the alloy-depleted region. A good correlation to experimental results has been shown in the prediction of limiting carbon concentration and $M_{23}C_6$ carbide content in white-bands. In addition, it was also suggested that depletion of carbides and carbon are strongly linked and that depletion of alloying elements only above a critical value will result in total carbide loss and thus recrystallisation into a white-band.

Acknowledgements

I would like to take this opportunity to express my respect and gratitude to my supervisors, Prof. Philip Shipway and Prof. Tom Hyde for their continued support and guidance. I am especially grateful to Prof. Philip Shipway for his outstanding support, encouragement and guidance throughout my MSc and PhD studies. I would also like to thank Dr. Wei Sun and Dr. Anas Yaghi for their immense support and contribution during my studies.

I thank the EPSRC and University of Nottingham for the financial support, and the following companies; Alstom Power Ltd., Corus, E.ON, Doosan Babcock, National Physical Laboratory, QinetiQ, Rolls-Royce, RWE npower, Sermatech and Siemens Industrial Turbomachinery for their practical support.

I thank Prof. Rachel Thomson, Prof. Graham McCartney, Dr. David Allen and Dr. Steve Brett for their support and help during my research. Sincere thanks to Dr. Fabienne Boue-Bigne in Corus for the LIBS work and Dr. Juan Sanchez-Hanton for the EBSD work. Many thanks to Mr. Brian Webster for creep testing and to Mr. Keith Dinsdale for TEM training and support. I would also like to thank Mr. Graham Malkinson, Mr. Stuart Branston, Mr. Tom Buss, Mr. Martin Toe, Dr. Nigel Neate, and Ms. Julie Thornhill for lab and workshop assistance.

I would also like to express my thanks to the friends I have made in Nottingham for support and help in my life. They are: Yi Ding, Yining Zhang, Ning Ding, Yu Fan, Sheetal Patel and Min Chen.

Most importantly, the unconditional love, support and care of my parents, brothers and my husband have been unsurpassed at all times; for this I am eternally indebted.

Abbreviations

BSE	back scattered electrons
CGHAZ	coarse-grained heat-affected zone
CMM	coordinate measuring machine
EBSD	electron backscatter diffraction
EDX	electron dispersive x-ray
FGHAZ	fine-grained heat-affected zone
FIB	focused ion beam
HAZ	heat-affected zone
ICHAZ	intercritical heat-affected zone
LIBS	laser induced breakdown spectroscopy
MMA	manual metal arc
OES	optical emission spectroscopy
OM	optical microscopy
PM	parent metal
PWHT	post-weld heat-treated
SADP	selected area diffraction pattern
SE	secondary electrons
SEM	scanning electron microscopy
TIG	tungsten inert gas
TEM	transmission electron microscopy
WM	weld metal
wt%	weight percent

Chapter 1

Introduction

Fast world economic growth and environmental concerns in recent decades have led to a growing demand for energy with sources ranging from renewables, nuclear power, gas, oil and coal. Although it has been demonstrated that conventional coal-fired power generation can be completely and effectively replaced in favour of other sources, owing to the currently availability of coal, fossil fuels will maintain a dominant share of the market as newer technologies are introduced, in spite of the fact that in developed countries much effort is being devoted to increasing the proportion of power generated from renewable sources. Therefore, it is essential that the conventional power plants must undergo continued development in order to safely extend the life of such plants beyond their original design lives.

In addition to more efficient management of salvage and repair operations in service, construction of new more efficient plant and/or improvement of thermal efficiency of current plants would be beneficial in terms of reduced greenhouse gas emissions and improved economics.

Increase in the thermal efficiency of a power plant can be most effectively achieved by increasing the temperature and the pressure of the stream entering the turbine. Most modern steam power plants now in operation reach efficiencies of around 42% with steam temperature of 600°C and pressure of 25-30 MPa, which can be improved to an efficiency of 45% with the next generation of power plant capable of operating with steam at 625 to 650°C (Ennis and Czyrska-Filemonowicz, 2003).

The requirements of higher thermal efficiency without decreasing the reliability and service life of the boiler and turbine components inevitably impose increasingly stringent requirements on the development of stronger materials, capable of operating under high stresses at ever increasing temperatures (Viswanathan and Bakker, 2000). For steels used in power plant, creep strength in particular is the most important property for high temperature and high stress

applications, which has led to ongoing research activities placing emphasis on the improvement of creep strength in alloy development. Ferritic steels including 2Cr, 9Cr and 12Cr steels have been employed for steam pipe work in coal-fired power plant since the 1960's. The continued developments of these steels with the addition and optimisation of Mo, V, Nb and W have resulted in a significant improvement of creep strength, enabling the operating temperature to be increased from 565°C to 650°C. Among these steels, the modified 9Cr alloy, P91, has the highest allowable stress and is now extensively used all over the world as a material for headers and steam pipes. However, lack of confidence in the long term performance of welds in advanced high alloy ferritic steels has been a major concern (Allen et al., 2005). Welding, as an essential part of fabrication of power plant components, can have a profound impact on structural integrity issues, reducing efficiency and shortening service lives.

In light of this, efforts have made in research and development of power plant steels with good creep strength as well as weldability, primarily through the optimisation of precipitate strengthening effects. Much of the development work is based on the investigation of microstructure and properties of existing alloys and welds during creep, along with the microstructural modelling which enables life prediction.

This work is part of EPSRC SUPERGEN (Conventional Power Plant Lifetime Extension) programme, a consortium of four universities and supporting industries which has been formed to address critical technical challenges relating to security of electricity supply and lifetime extension of conventional power plant within the UK. It aims to develop an interdisciplinary approach to the predictive methods/models, based on improved understanding of microstructure and structural integrity.

This thesis focused on the study of microstructural developments of P91 weld metal in isolation during creep exposure. Although creep failure of welds in power plant mostly occurs in the Type IV region (Intercritical heat-affected zone), the creep failure in weld metal itself has emerged as Type IV failures have been eliminated due to research and development. This work examined the creep response of P91 weld metal itself in the aspects of microstructure and mechanical

properties, seeing to both understand and model behaviour of these microstructurally complex regions.

Chapter 2

Literature review

2.1 DEVELOPMENT OF POWER PLANT STEELS

Energy saving and environmental protection in power generation require further improvements in efficiency; one way in which these can be achieved is by increasing the temperature and pressure of the steam, as illustrated in Figure 2.1 (Mayer et al., 1998). For example, a 6% efficiency increase can be achieved by changing the steam conditions from 538°C/18.5 MPa to about 593°C/30 MPa. Higher temperatures and pressures up to about 650°C/34.5 MPa are currently being pursued for the future higher efficiency. The main technology enabling the increase of temperature and pressure of steam is the development of stronger high temperature materials capable of operating under high stresses at increasing temperatures (Viswanathan and Bakker, 2000; Viswanathan et al., 2006).

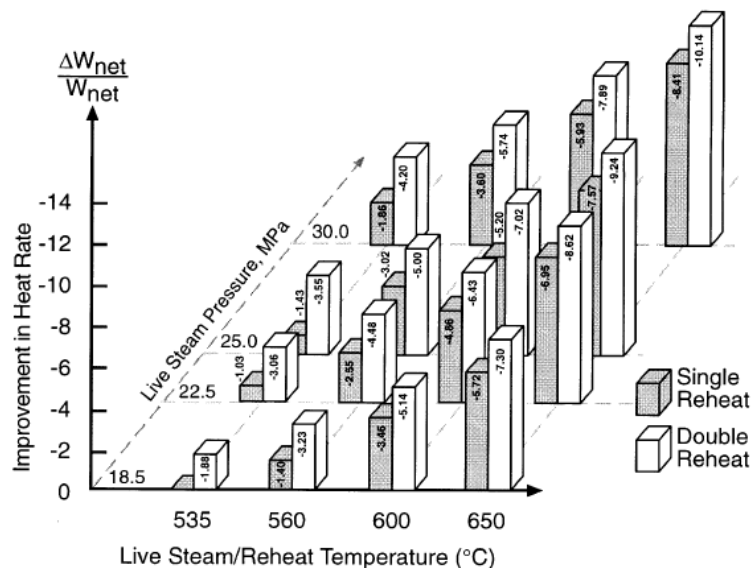


Figure 2.1 Improvements in heat rate (efficiency) achieved by increasing steam temperature and pressure using single and double reheat cycles (Mayer et al., 1998), compared to the base case of 535°C/18.5 MPa

Materials with ferritic/martensite microstructures are preferred over austenitic stainless steels because of their favourable physical properties, such as good thermal conductivity and low coefficient of thermal expansion, coupled with a high resistance to thermal shock (Cerjak and Letofsky, 1998). The historical development of the steels for power plant application is shown in Figure 2.2 (Masuyama, 1999). It can be seen that the development of the ferritic steels has taken place over four generations, which is also indicated in Table 2.1 and Figure 2.3.

The development of the four generation ferritic steels was mainly based on 9Cr-1Mo steels (T9) and 12Cr steels (AISI410), which were put into service before the 1960s. The 600°C/10⁵ hour creep strength was as low as 35 MPa before the 1960s. In 1960s, the additions of molybdenum, niobium, and vanadium gave rise to the first generation steels of the 60 MPa class (The 600°C/10⁵ hour creep rupture life). These steels, including EM12, HCM9M, HT9, F9 and HT91, were able to work under the maximum temperature of 565 °C. The additions of niobium, vanadium and carbon were optimised from 1970 to improve the creep strength of the steels known as the second generation. From this development issued T91/P91 has been extensively used all over the world as the materials for headers and steam pipes in supercritical plants operating at the temperature up to 593°C. The third generation was developed from 1985 to 1995, when the tungsten was introduced to partially substitute molybdenum, in steels such as P92, P122, which can work at a temperature up to 620°C. For the fourth generation of steels (180 MPa class steels), steels which can work at maximum 650°C are expected to emerge. Progress has been made in the laboratory by the addition of cobalt and more tungsten.

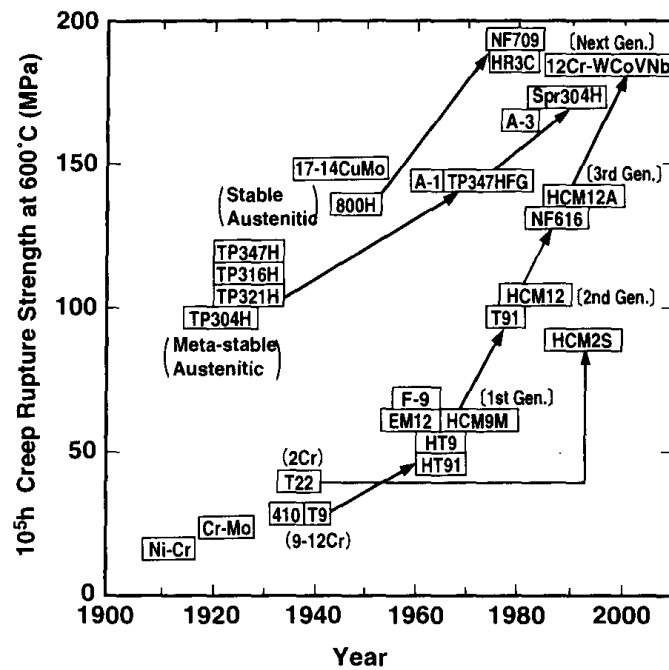


Figure 2.2 Historical improvements of creep rupture strength in steels for boiler (Masuyama, 1999)

Generation	Years	Alloy Modifications	Strength 10^5 hr Creep Rupture Achieved at 600°C / MPa	Example Alloys	Maximum Metal Temp. $^\circ\text{C}$
1	1960-70	Addition of Mo or Nb, V to simple 12Cr and 9Cr Mo steels	60	EM12, HCM9M, HT9, Tempaloy, F9, HT91	565
2	1970-85	Optimization of C, Nb, V	100	HCM12, T91, HCM2S	593
3	1985-95	Partial Substitution of W for Mo	140	P-92, P-122, (HCM12A, NF616)	620
4	Emerging	Increase of W and addition of Co	180	NF12, SAVE12	650

Table 2.1 Evolution of four generations of ferritic steels (Viswanathan and Bakker, 2000)

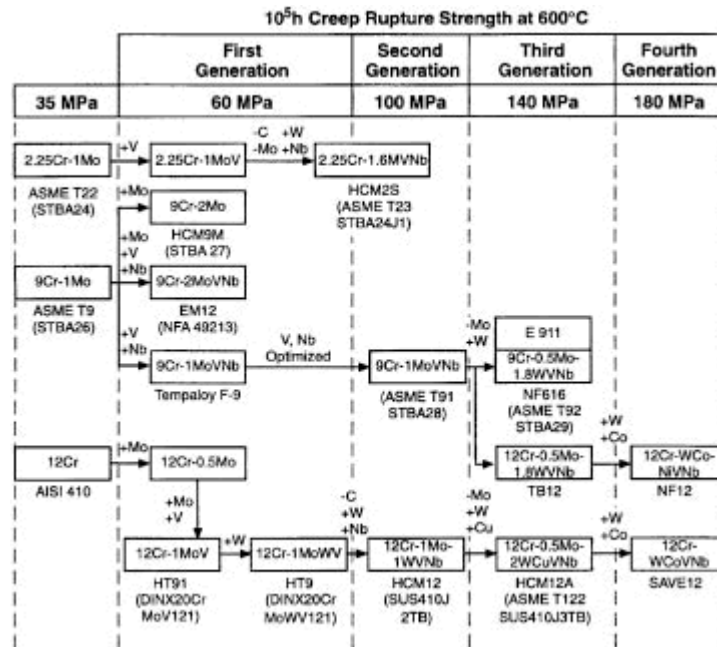


Figure 2.3 Development progress of ferritic steels for boiler (Viswanathan and Bakker, 2001)

2.2 P91 STEELS

The modified 9% Cr 1% Mo steel known as P91/T91 (or as X10CrMoVNb9-1 in Europe) has been successfully accepted world-wide since the late 80's for header and steam piping in power industries due to its excellent elevated temperature strength and creep behaviour. In modern fossil-fired power-plant, the application of grade 91 steels allows higher operating temperatures and pressures, and therefore higher efficiencies. Based on European experience, grade 91 steels can be used inside the boiler (superheaters, reheaters) for steam temperatures up to 560°C (maximum metal temperatures around 600°C), and outside the boiler for pipe and headers up to about 610°C (Haarmann et al., 2002).

2.2.1 Compositions of P91 parent metal

The grade 91 steel is a ferritic / martensitic (9% chromium, 1% molybdenum) steel micro-alloyed with vanadium and niobium and with controlled nitrogen content. The chemical composition of grade 91 specified by ASTM standards is listed in Table 2.2.

	C	Mn	P	S	Si	Cr	Mo	V	Nb	N	Al	Ni
min.	0.08	0.30			0.20	8.00	0.85	0.18	0.06	0.030		
max.	0.12	0.60	0.020	0.01	0.50	9.50	1.05	1.05	0.10	0.070	0.040	0.40

Table 2.2 Chemical composition of Grade 91 steel (wt%)

2.2.2 Effect of alloying elements

Chromium (Cr)

Chromium is the main alloying element in P91 steel and other heat resistant ferritic steels. It is the most important element contributing to solid solution strength as well as to oxidation and corrosion resistance (Viswanathan and Bakker, 2000). Chromium is a solid-solution strengthener and carbide former. The strengthening effect is achieved by the precipitation of chromium-rich carbides from the solid solution, which can impede the movement of dislocations and grain

boundaries to increase creep strength of the steels. The chromium carbides M_7Cr_3 and $M_{23}C_6$ are two main chromium carbide types in chromium steels; $M_{23}C_6$ dominates in the 9-12%Cr steels (Klueh, 2005).

Molybdenum (Mo)

Molybdenum is a ferritic stabiliser. It improves the creep properties of the steels by solid solution hardening (Sourmail, 2001). However, molybdenum can be detrimental because it accelerates the growth of $M_{23}C_6$ carbides (Maruyama et al., 2001). Molybdenum can form Mo_2C in low chromium steels, such as 2.5Cr-1Mo steels, but it does not form carbides or nitrides in 9-12%Cr steels (Nutting, 1999). In tempered conditions, molybdenum is found in solid solution and provides relatively high solid-solution strengthening of iron. However, the amount of the molybdenum must be limited to avoid the formation of δ -ferrite and Laves-phase. It has been stated in reference (Klueh, 2005) that at equilibrium, the molybdenum equivalent Mo_{eq} , defined as $Mo + 0.5W$ (wt%), should not exceed 1%. Exposure of the 9-12%Cr steels with Mo and/or W at a $Mo_{eq} \geq 1\%$ at 600 to 650°C has been shown to result in the precipitation of Laves-phase, which removes the element from solid solution and reduces the solid solution strengthening (Klueh, 2005).

Tungsten (W)

Tungsten is now added to the 9-12%Cr steels or substituted for part of the molybdenum. It is a natural choice to replace molybdenum because they are in the same column of the periodic table and behave similarly in steels (form similar types of carbides, etc.) (Klueh and Bloom, 1985). Like molybdenum, tungsten is also a solid solution strengthener. The addition of tungsten to the steels has been found to be effective in increasing the creep strength at high temperatures and has already been used in some newly developed steels such as P92 and P122 for ultra super critical (USC) boilers (Masuyama, 1999). However, similarly to molybdenum, the strengthening effect of tungsten can be diminished dramatically during long time exposure at high temperatures due to the precipitation of Laves-phase. The limit of tungsten can be defined using molybdenum equivalent Mo_{eq} ($Mo + 0.5W$ (%wt)), which is about 1 wt% at 600 to 650°C (Foldyna et al., 1991; Klueh, 2005; Foldyna et al., 1996).

Vanadium and Niobium (V, Nb)

Vanadium and niobium are added in small quantities to obtain the desired creep properties. Both of them are strong carbide, nitride and carbonitride formers. In 9-12%Cr steels, they are expected to form MX, where M represents the metals V, Nb, and X is either carbon or nitrogen, or a combination of the two, resulting in carbides MC, nitrides MN, or carbonitrides M(C, N) (Viswanathan and Bakker, 2000). Although the density of MX particles is low in normal high chromium steels, the particles are necessary to preserve the fine subgrain structure and thus the improved creep strength of the steels. Maruyama (2001) have made a comparison among three ferritic steels: 9Cr-1.8W-0.4Mo-VNb steel (0.16%V, 0.06%Nb, 0.11%C and 0.036%N) with tungsten and MX particles, 9Cr-1Mo-VNb steel (0.22%V, 0.09%Nb, 0.10%C and 0.051%N) with MX particles but without tungsten, and 9Cr-2W steel (0.08%C) with tungsten but without MX particles. The stress rupture curves showed that 9Cr-1Mo-VNb steel is inferior to 9Cr-1.8W-0.4Mo-VNb in creep rupture strength because the absence of tungsten. However, the rupture life of 9Cr-2W is substantially shorter than that of 9Cr-1Mo-V-Nb steel in spite of tungsten addition. The important role of the MX particles was seen as a major factor in determining these properties.

Nitrogen (N)

Nitrogen also plays an important role in increasing the creep life of steels. It can act like carbon by the precipitation of nitrides (MN), but the nitrogen remaining in solid solution has a much greater strengthening effect than that of carbon. Recent results indicated that vanadium-rich MX is rich in nitrogen. VN is the primary nitride, although niobium and aluminium can form nitrides as well (Sourmail, 2001). Brett et al. (2004) have indicated that a number of early failures of grade 91 components in the UK were found to be associated with both low hardness and with chemical composition which were relatively low in nitrogen and high in aluminium (low N:Al ratio). It was widely accepted that the creep strength of this class of alloy is sensitive to minor variations of N:Al ratio (Sanchez-Hanton et al., 2008).

Boron and Phosphorus (B, P)

In many of the 9-12%Cr steels, 0.005-0.01% boron is added to improve the creep strength. It has been found that boron can segregate to the interface between $M_{23}C_6$ particles and the matrix to decrease the rate at which the carbide can coarsen, thus stabilizing the microstructure, since $M_{23}C_6$ particles help in pinning the subgrain boundaries (Klueh, 2005). It was also found that boron assists in the nucleation of VN particles by the mechanism of latent creep resistance (Garrison and Buck, 1999). Most of the boron atoms are in solution. They can combine with vacancies to reduce the self-diffusion coefficient of ferrite matrix. They can also form a Cottrell atmosphere around dislocations and thus increase creep deformation resistance (Hald and Straub, 1998; Kaneko et al., 1995). Phosphorus can also segregate to the surface of $M_{23}C_6$, and a small amount of phosphorus was also found in the Laves-phase (Schwind et al., 1998).

Carbon

Carbon is a strong austenite stabiliser with a relatively large solubility in austenite. However, it has a very small solubility in ferrite, which contributes to the formation of carbides and carbonitrides as discussed before. Although carbon is required to form fine carbide precipitates, the amount needs to be optimized for good weldability. An increase in carbon level promotes the formation of lower-temperature transformation products, such as bainite and martensite, and leads to a significant reduction in cleavage resistance of heat-affected zone (HAZ) of weldments (Chen and Pollack, 1993).

Nickel and Manganese (Ni, Mn)

Nickel and Manganese are austenite stabilisers. The main reason for adding them to 9-12%Cr steels is to ensure 100% austenite formation (without δ -ferrite) during the austenitisation treatment by lowering the temperature for transformation from austenite to ferrite, thus ensuring 100% martensite when cooled (Hayashi et al., 1999). Nickel can also improve the toughness but at the expense of the creep strength due to its effect in accelerating precipitate coarsening. Nickel promotes the formation of M_6C , thus destabilising the $M_{23}C_6$, which stabilises the subgrain structure (Hayashi et al., 1999). Manganese is a weaker austenite stabiliser than

nickel, and it has similar effect on carbide coarsening and the formation of M_6C (Hayashi et al., 1999; Maruyama et al., 2001).

Copper (Cu)

Copper is also an austenite stabilising element, but it differs from nickel and manganese since it has a low solubility in ferrite. Partial replacement of nickel by copper can help stabilise the creep strength (Viswanathan and Bakker, 2000). Copper precipitation can strengthen the steel and can play a role in the nucleation of other phases during thermal aging or creep. Some researchers have concluded that copper precipitates increased the elevated-temperature strength, but others grouped copper with nickel and cobalt as accelerating precipitate coarsening (Klueh, 2005).

Summary

The contents of alloying elements for 9-12%Cr steel are designed for the optimum creep resistant properties under operating conditions. The roles of each alloying element in creep of high chromium ferritic steels are summarised in Table 2.3 (Maruyama et al., 2001).

Element	Merit	Demerit
B	Improve creep strength and quench hardenability; Stabilise $M_{23}C_6$ particles and delay their coarsening.	Reduce impact toughness.
C	Necessary to make $M_{23}C_6$ and NbC	
Co	Suppress δ -ferrite; Decrease D.	
Cr	Improve oxidation resistance; Lower M_S ; Raise A_1 ; Main element in $M_{23}C_6$.	Increase D
Cu	Suppress δ -ferrite.	Promote precipitation of Fe_2M
Mn		Increase D and reduce creep strength; Lower A_1 ; Promote M_6C precipitation.
Mo	Lower M_S . Raise A_1 ; Solid solution hardening.	Accelerate growth of $M_{23}C_6$
N	Necessary to make VN.	
Nb	Form MX and contribute to strengthening.	Promote precipitation of Z Phase.
Ni		Increase D and reduce creep strength. Lower A_1 .
Re	Prevent loss of creep rupture strength; Lower M_S .	Lower A_1 .
Si	Improve oxidation resistance.	Increase D and reduce creep strength.
V	Form MX and contribute to strengthening,	
W	Lower M_S ; Raise A_1 ; Delay coarsening of $M_{23}C_6$ particles; Solid solution hardening.	

*D - diffusion coefficient of carbon

Table 2.3 Roles of elements in creep of high chromium ferritic steels (Maruyama et al., 2001)

2.2.3 Microstructural features of P91 steel

The microstructure of 9-12%Cr steels is designed by balancing austenite and ferrite stabilisers to produce 100% austenite during the austenitisation and the 100% martensite during quenching treatment following austenitisation, although a small amount of δ -ferrite may be present in some cases, especially in 12%Cr steels (Klueh, 2005). Schaeffler diagram is a constitution diagram used for estimation of metallurgical phases present in steel weld metal. Figure 2.4 is the Schaeffler Diagram showing the location of the composition of the 9-12%Cr steels. The chromium equivalent Cr_{eq} and nickel equivalent Ni_{eq} in order to locate the position of steels in Schaeffler Diagram are:

$$Cr_{eq} = \%Cr + 2\%Si + 1.5\%Mo + 5\%V + 1.75\%Nb + 1.5\%Ti + 0.75\%W \quad (\text{wt}\%) \quad [2.1]$$

$$Ni_{eq} = \%Ni + \%Co + 0.5\%Mn + 0.03\%Cu + 25\%N + 30\%C \quad (\text{wt}\%) \quad [2.2]$$

In Figure 2.4, four types of 9-12%Cr steels including T91, P91, X20 and EM12 are located. Except for the EM12 steel, which is inside the martensite + ferrite (M+F) stability zone, the remaining steels are located inside the martensite (M) stability zone and very close to the border line of δ -ferrite formation. It means that although these steels have fully martensitic microstructure, they have a high potential for the formation of δ -ferrite (Ayala et al., 1999).

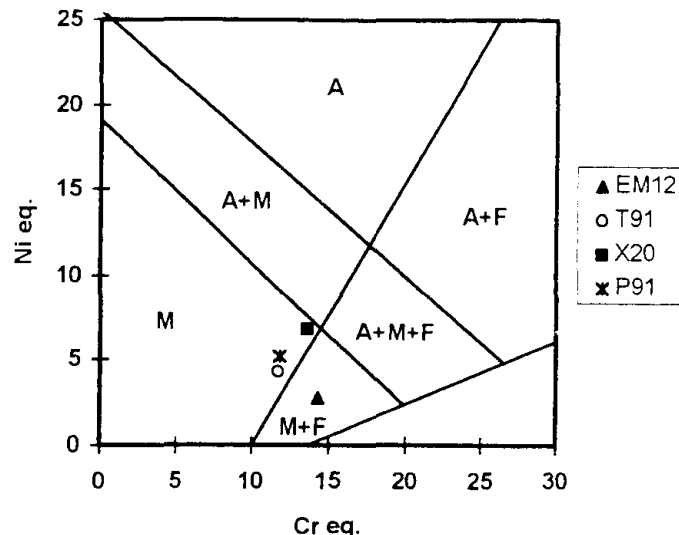


Figure 2.4 Schaeffler diagram showing the location of the composition of 9-12%Cr steel welds (Ayala et al., 1999)

P91 steel, like other high chromium steels, is commonly heat treated by austenitising, quenching and a subsequent tempering treatment at an intermediate temperature. As seen from the phase diagram of P91 steel in Figure 2.5, the as-received P91 steel is heated up to the austenite region (around 1040°C to 1100°C) which provides dissolution of most $M_{23}C_6$ carbides without significant grain growth, and then cooled to room temperature (Ayala et al., 1999). A martensitic lath structure with high density of dislocations is produced in the steel after this treatment.

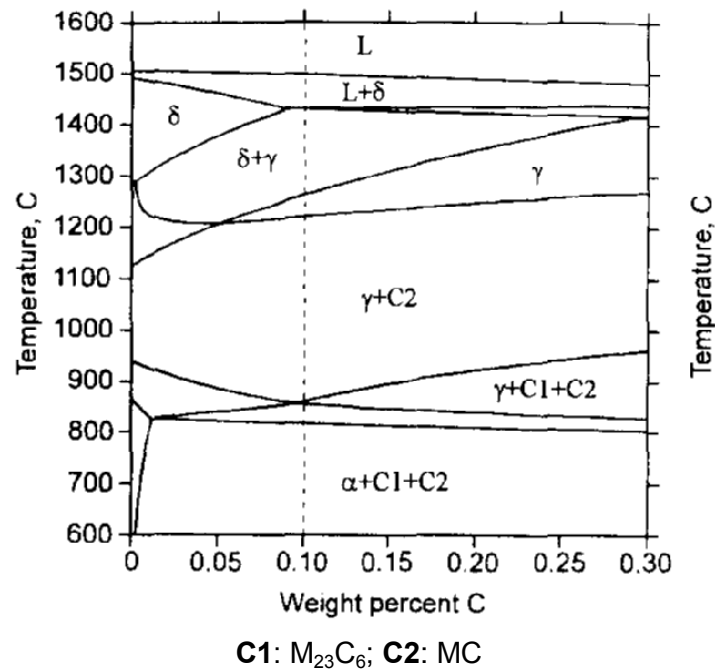


Figure 2.5 Isopleth phase diagram of T91/P91 steel (Ayala et al., 1999)

The steel is then subjected to tempering at a temperature below A_{c1} (750°C to 780°C). During the tempering treatment, the martensitic lath structure changes into a subgrain structure by fragmenting the original martensitic laths by transversal sub-boundaries. The high strength of the steel is mainly conferred by the martensitic structure. The tempering treatment also allows carbides to precipitate homogeneously within the martensite structure, thus improving the creep behaviour. A beneficial combination of the strength and toughness is achieved by age hardening reactions coupled with dislocation recovery processes during tempering beyond 600°C (Klueh, 2005; Gocmen et al., 1998).

Figure 2.6 is the schematic representation of non-uniform precipitation states in tempered martensitic 9-12%Cr steels (Gocmen et al., 1998). The microstructure after heat treatment consists of martensite blocks within former austenite grains, with each block being split into elongated subgrains (laths). The precipitation state in the high tempered condition is non-uniform on the scale of the interface substructures. The coarse carbonitrides are non-uniformly distributed in different subgrains. Maruyama et al. (2001) have concluded that two types of precipitates appear in high chromium steels before creep: $M_{23}C_6$ carbides and MX carbonitrides, as shown in Figure 2.7. The $M_{23}C_6$ carbide particles formed during

tempering are mainly located on the grain boundaries and subgrain boundaries. The Cr_{23}C_6 precipitates are the primary type of M_{23}C_6 precipitates, whilst some of chromium atoms are replaced with Fe and other elements (Maruyama et al., 2001; Orlova et al., 1998). Other finer precipitates are also present in the subgrain interior. Maruyama et al. (2001) have found that the MX precipitates in 9-12%Cr steels are primarily classified into VN and NbC, with some VC and NbN, being observed. However, Orlova et al. (1998) have also found Nb_2C , MoC and Mo_2C in T91 steel.

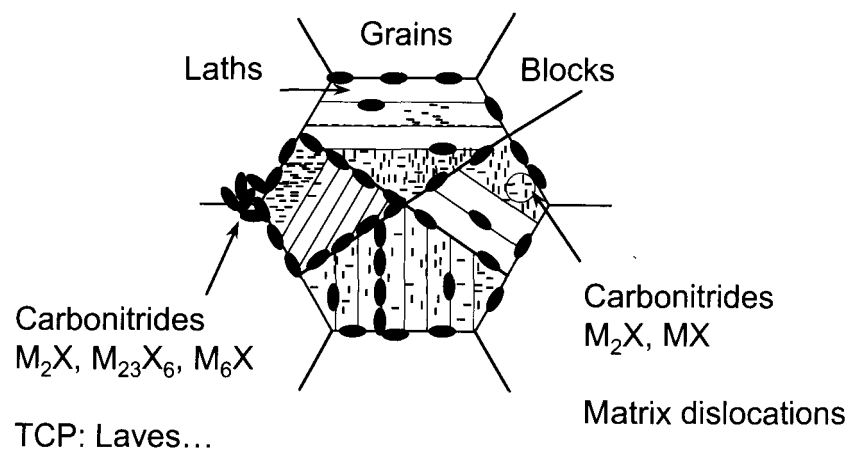


Figure 2.6 Schematic representation of non-uniform precipitation states in tempered martensitic 9-12%Cr steels (Gocmen et al., 1998)

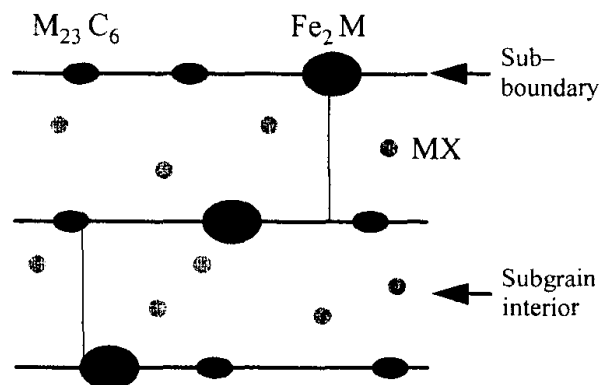


Figure 2.7 A schematic drawing of precipitates in high chromium ferritic steel (Maruyama et al., 2001)

2.2.4 Characteristics of precipitates

As mentioned in the previous section, there are two main types of precipitates in 9-12%Cr steels in as-received heat-treated conditions: $M_{23}C_6$ and MX. The formation of other minor precipitates, such as M_2X and M_6X , is also possible, depending on the specific materials and heat treatment conditions (Orlova et al., 1998; Maruyama et al., 2001; Anderson et al., 2003).

$M_{23}C_6$

$M_{23}C_6$ carbide is the principal precipitate type found in 9-12%Cr steels in quenched and tempered conditions. Normally, austenitisation at 1070°C and above leads to complete dissolution of $M_{23}C_6$ carbides, whilst for austenitisation at 970°C not all $M_{23}C_6$ carbides are dissolved (Ennis et al., 1998). Previous investigations have shown that $M_{23}C_6$ forms very rapidly during tempering, where M_3C particles precipitated after austenitisation dissolve and the more stable carbide $M_{23}C_6$ forms (Ennis et al., 1998; Maruyama et al., 2001). It was found that $M_{23}C_6$ carbides precipitated mainly on prior austenite grain boundaries and subgrain boundaries, whilst some smaller $M_{23}C_6$ carbides were also found in the martensite lath interiors. Anderson et al. (2003) have found the average size for the $M_{23}C_6$ carbides on the prior austenite grain boundaries to be 380 nm before creep and 460 nm after creep, which are very similar to values reported elsewhere. The $M_{23}C_6$ precipitate has a face-centred-cubic (fcc) structure (Sourmail, 2001). The composition of $M_{23}C_6$ precipitates has been investigated by many researchers. The EDX analysis performed by Anderson et al. (2003) indicated that the $M_{23}C_6$ precipitates in the modified 9Cr-1Mo steels contain high chromium with iron and molybdenum. In steels containing nickel, nickel was also found in $M_{23}C_6$ precipitates to substitute partially for chromium (Sourmail, 2001). Small amounts of $M_{23}C_6$ precipitates were also found in the martensite lath interiors, but at a much finer scale. These are approximately 200 nm in size (Anderson et al., 2003). $M_{23}C_6$ precipitates retarded the subgrain growth and therefore increased the strength of the materials (Ennis et al., 1998). However, $M_{23}C_6$ precipitates can only strengthen the steels at the early stage of creep due to their coarsening at the grain boundaries and subgrain boundaries after long time exposure at high temperatures, which gives rise to a reduction in creep strength (Anderson et al., 2003; Yin and Faulkner, 2005).

MX

Another precipitate type important for the mechanical properties of 9-12%Cr steels is MX (where M = Nb or V; X = C and/or N), namely, carbides, nitrides and carbonitrides. Unlike $M_{23}C_6$ precipitates, MX precipitates form primarily in the subgrain interiors. MX precipitates are normally smaller than the $M_{23}C_6$ carbides (Orlova et al., 1998). The MX carbonitrides have a NaCl face-centred-cubic (fcc) structure (Sourmail, 2001).

There are three types of MX precipitates in terms of the morphology of the precipitates. Firstly, primary NbX particles are spherical and relatively coarse. They remain after austenitisation being randomly dispersed throughout the matrix of the steel, due to the Nb content of the steels being much higher than the limits of the mutual solubility of Nb and C/N in austenite at the austenitisation treatment temperatures used for these steels (Maruyama et al., 2001; Ennis et al., 1998; Vodarek and Strang, 2000; Strang and Vodarek, 1998). The average size of the Nb rich MX precipitates observed by Anderson et al. (2003) was approximately 400 nm before creep and 450 nm after creep. Secondary MX phases form during tempering, including spherical NbX particles and platelet VX particles (Maruyama et al., 2001). These MX particles are fine and distributed uniformly within the subgrains as well as on subgrain boundaries (Maruyama et al., 2001). The formation of the secondary MX phases is affected by the tempering temperature. Strang and Vodarek (1998) have carried out three tempering processes at different temperatures (600°C, 650°C and 700°C) on three 12CrMoVNb steel samples, and found that with 600°C tempering, the MX phase was not observed; with 650°C tempering, a small amount of secondary MX phases was observed; with 700°C tempering, the predominant phase was MX. Foldyna et al. (1996) also reported that M_2X precipitates form at tempering temperatures lower than 700°C, while above this temperature, the MX phase tends to form. The secondary MX phases are actually vanadium rich precipitates, where the vanadium content is much higher than the niobium content. Unlike the much larger primary niobium-rich precipitates, which simply remain undissolved throughout the austenitising treatment, these vanadium-rich MX precipitates form during tempering. They have a much smaller average size of approximately 100 nm. In addition, there is another type of MX precipitate called V-wing complex. The larger, spheroidal particles of primary NbX undissolved during austenitising can act as the

nucleation sites during tempering for the plate-like V-rich nitrides, thus forming the V-wing complexes (Ennis and Czyska-Filemonowicz, 2003). Maruyama et al. (2001) found that these V-wing complexes are also formed on fine NbX particles during creep.

It has been generally agreed that MX particles are able to improve the strength of 9-12%Cr steels (Maruyama et al., 2001; Yin and Faulkner, 2005). Anderson et al. (2003) have suggested that the coarse primary Nb-rich MX precipitates are insoluble at austenitising temperatures. The presence of these undissolved MX particles during austenitisation is able to limit the growth of austenite grains and ensure that the recrystallisation of martensitic laths during tempering does not result in a massive loss in creep strength. MX particles, especially the fine secondary MX particles, can improve the creep strength by two mechanisms: one is that MX particles themselves act as obstacles to dislocation motion, and another way is that they slow down the recovery of the dislocation substructure and retain the dislocation hardening for a longer duration (Maruyama et al., 2001).

M_2X

M_2X particles have been found within subgrains after austenitisation. However, it has been argued that these may dissolve and are replaced by more stable MX precipitates. Especially when high tempering temperatures above 700°C are used, only small amount of M_2X particles remain (Vodarek and Strang, 2000). Electron diffraction and EDX studies on 12CrMoVNb steels by Vodarek et al. (2000) indicated that the M_2X precipitates were rich in chromium and had a crystal lattice isomorphous with that of Cr_2N . M_2X precipitates were also found by Anderson et al. (2003) in a modified 9Cr-1Mo steel and they contained high Cr with V, Mo and Fe. The average size of these precipitates is approximately 120 nm. M_2X is believed to be an undesirable phase due to its relatively low stability at high temperature.

M_6X

M_6X is a face-centred-cubic carbide, which has been found in 12CrMoVNb steel (Vodarek and Strang, 2000) and modified 9Cr-1Mo steel (Anderson et al., 2003). The former work identified that the M_6X particles were rich in Mo, Cr and Ni, and

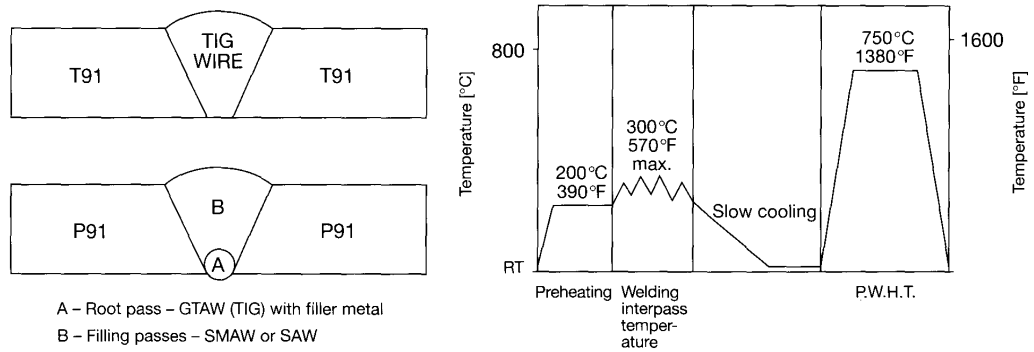
this type of precipitate was found in the steel after creep exposure at 550°C. Sourmail (2001) also agreed that M_6X precipitates normally appear after long time creep exposure. However, Anderson et al. (2003) have found a small amount of M_6X in as-tempered modified 9Cr-1Mo steels.

2.3 P91 WELD METAL

The microstructural features of P91 steel, as well as other 9-12%Cr steels have been well characterised. The excellent creep resistance of these ferritic steels is attributed to several strengthening mechanisms, such as solid solution hardening and precipitation strengthening. Although P91 steels possess very high creep strength, welding (either prior to service or in repair) inevitably affects the creep properties. Over the years, high temperature pipework systems have shown very few failures that are not associated with welds (Brett, 1994). The welding process, including the post-weld heat treatment (PWHT), results in a reduced creep rupture life of the weldments compared to the parent metals.

2.3.1 Welding process for P91 pipework

Fusion welding is a welding process where fusion is employed to complete the weld. The weld joints are made by fusing and running together adjacent edges or surfaces. It involves a heat source and normally involves the use of a filler material such as a consumable electrode or a wire fed into the weld pool. A protective layer is also used between the atmosphere and the molten metal, either in the form of gas shielding or a flux which melts to give a viscous slag on the weld metal that eventually can be removed. In terms of heat source, fusion welding is often classified as gas welding, arc welding, and resistance welding. For P91 steel pipelines in power plant, arc welding is normally used. Specifically, there are several welding processes applied, such as gas tungsten arc welding (GTAW), submerged arc welding (SAW), shielded metal arc welding (SMAW) and manual metal arc welding (MMAW). The typical welding procedure of T/P91 to T/P91 is shown in Figure 2.8, root run using GTAW and weld filled using SMAW or SAW (Haarmann et al., 2002).



T91 boiler tubes: wall thickness < 10 mm

P91 steam pipes: wall thickness around 60 mm

Figure 2.8 Welding Procedure of T/P91 to T/P91 (Haarmann et al., 2002)

In order to reduce the adverse effects caused by welding to the minimum, some heat treatments are applied. The typical heating cycle during and after welding are shown in Figure 2.9 (Haarmann et al., 2002). Preheating and welding occurs at temperatures around 250°C. Bergquist (1999) suggested a preheat temperature between 200°C and 350°C. After welding, it is essential to cool down to a temperature below 100°C, to ensure that the martensite transformation has been fully completed. Afterwards a post-weld heat treatment (PWHT) is applied to reduce the high as-welded residual stress levels and improve the toughness and defect tolerance of the joint. The PWHT temperature is normally between 750°C and 760°C. In practice, the weld metal shows satisfactory tempering at a tempering parameter P of 21 or above. P is the parameter involving T and t ,

$$P = T (\log t + 20) \times 10^{-3}$$

where T is the exposure temperature in (*Kelvin*); t is the exposure time in hours. It equates to 755°C for 3 hours or 760°C for 2 hours (Chen and Pollack, 1993).

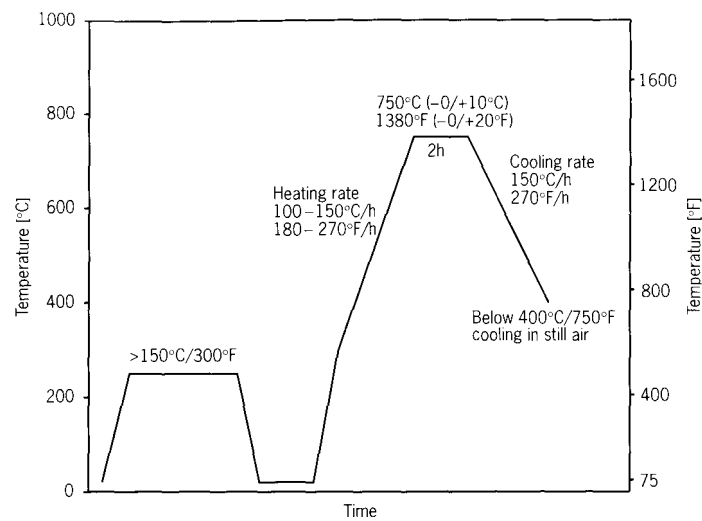


Figure 2.9 Typical heating cycle for welding T/P91 (Haarmann et al., 2002)

For the welding of large section P91 pipes, multipass welding is usually applied. The reheat thermal cycle of each welding pass austenitises and refines the portions of the microstructure in the previous weld metal, and also tempers the previous weld metal and reduces residual stresses from previous runs. Previous weld passes provide certain preheat that slows down the cooling rate of the subsequent passes (Chen and Pollack, 1993). The interpass temperature involved in multipass welds is represented by the minimum and maximum temperatures of the deposited weld metal and adjacent base metal before the next pass is started. It has to be kept at least equal to the preheat temperature.

Typical procedures for T/P91 welding, particularly for multipass welding, are given schematically in Figure 2.8, where the preheating temperature is 200°C, the interpass temperature is 300°C and a PWHT temperature of 750°C is used.

2.3.2 Microstructural features of welds

In welding, the intense heat source interacts with the materials, which experience very different thermal profiles from region to region, giving unique microstructure features in different regions of the weld. The classical definition of a welded structure includes three regions: these are the unaffected parent metal (PM), the heat-affected zone (HAZ) and the fusion zone, namely the weld metal (WM)

(Lancaster, 1993). However, microstructural examination at finer scales reveals a more complicated metallurgical condition at the weld interface region, which is the interface between the weld metal (WM) and heat-affected zone (HAZ) (Savage et al., 1976). The schematic diagrams of the weld microstructures in both the classical and Savage et al. (1976)'s definitions are shown in Figure 2.10 (a) and (b), respectively. In the definition of Savage et al, two additional zones between weld metal (WM) and heat-affected zone (HAZ) have been introduced into weld interface region. They are the unmixed zone and partially melted zone, as indicated in Figure 2.10(b). The P91 steel parent metal has been introduced in previous sections. The microstructure features and properties of other regions will be discussed in the following sections.

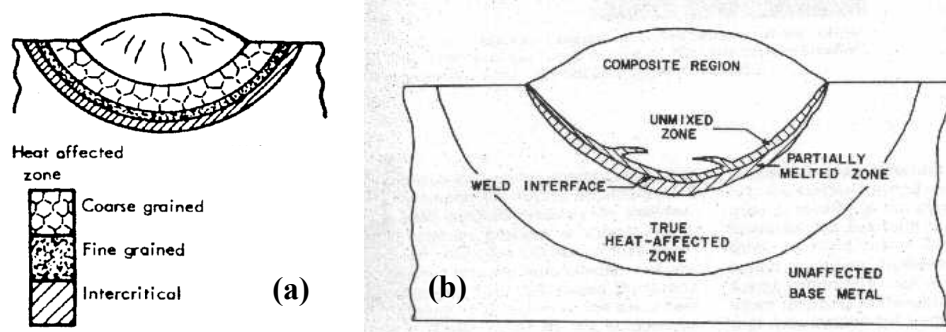


Figure 2.10 Schematic diagrams of weld structures: (a) Classical definition; (b) Savage et al.'s definition of weld interface region (Savage et al., 1976)

2.3.2.1 Heat-affected zone (HAZ)

Heat-affected zone (HAZ) is the area of base metal, which has had its microstructure and properties significantly altered by the thermal cycle associated with welding. Depending on the thermal history, different microstructures appear in the HAZ of a P91 fusion weld, which can be divided into two distinct regions: the high temperature region and the low temperature region. The former region is mainly the coarse grained heat affected zone (CGHAZ), while the latter consists of the fine grained heat affected zone (FGHAZ) and the intercritical heat affected zone (ICHAZ). The distributions of these different regions are shown in Figure 2.10 (a).

During the welding process, the CGHAZ is just adjacent to the hot, molten weld deposit. It experiences very high peak temperature, which is much higher than the α to γ transformation temperature A_{c3} , completely re-austeniting the microstructure. The rapid cooling experienced after welding results in the coarse grain microstructure of the former austenite. The number of grain boundary precipitates in the CGHAZ is quite low, due to the high temperature experienced which is enough to re-dissolve previously existing particles, and the rapid cooling which does not give enough time of temperature to form new precipitates. The FGHAZ experiences a lower peak temperature around the A_{c3} , which allows the recrystallisation to take place, yielding a finer grain structure. Pre-existing precipitates are not re-dissolved but coarsened. The ICHAZ experiences an even lower peak temperature during welding, just above the eutectoid A_{c1} temperature. The microstructure in this region is a mixture of fine recrystallised grains and unchanged coarser grain structure of parent metal (Agyakwa, 2004).

2.3.2.2 Weld metal (WM)

Weld metal is the portion of the weldment which experienced melting and re-solidification during the welding process. Filler metal and parent metal are melted together and well mixed, and element distribution in this region is generally thought to be uniform. The weld metal in single-pass weldments exhibits a coarse columnar microstructure, as shown in Figure 2.10. The weld metal in multi-pass weldments is normally made up of a large number of overlapping weld beads where a heating and cooling thermal cycle of each bead was repeated and has affected adjacent beads. As shown in Figure 2.11, the weld metal in multi-pass weldments actually includes the coarse columnar region, recrystallised coarse grain region and recrystallised fine grain region. The last two regions are together termed the recrystallised region. The recrystallised region is made up of the coarse columnar zone of previous beads, which have been re-austenitised by the subsequent bead deposition leading to the refined equiaxed structure.

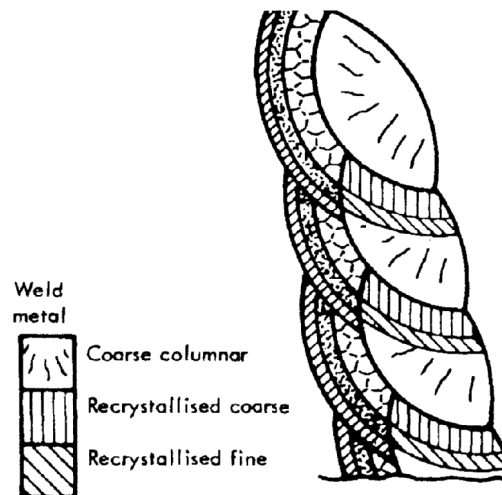


Figure 2.11 Schematic diagram of multipass welding (Agyakwa, 2004)

2.3.2.3 Weld interface region

The weld interface of the weldment is classically defined as the interface between the liquid metal and heat affected zone. However, microstructural examination on a finer scale reveals a more complicated metallurgical condition at the fusion boundary. Savage et al. (1976) have established a schematic illustration of the various regions of the weld resulting from a heterogeneous weld process, which is shown in Figure 2.10 (b). What is normally called the fusion line is actually a region, rather than a simple line. Two additional zones between melted weld metal and heat affected zone have been introduced into the fusion boundary region. They are the unmixed zone and the partially melted zone. The interface between these two regions is called weld interface, namely the fusion boundary.

Unmixed zone

The unmixed zone is the narrow band consisting essentially of melted and solidified base metal and any composition gradient between the composite region and the parent metal contained in the unmixed zone. The base metal in this region has been completely melted. Savage et al. (1976) argued that while molten, the materials in this region only experienced lamellar flow, indicating that the liquid at the fusion boundary does not experience convective mixing but only diffusional mixing.

Generally, the significance of this unmixed zone is given more consideration for the fusion boundary of heterogeneous weld; and less for autogenous and homogeneous welds due to their uniform composition. However, in an autogenous or homogeneous weld, the resulting composition of the weld metal may be still significantly different from the base metal due to other factors during welding, such as, absorption, outgassing, oxidation, and vaporization of certain elements. So an unmixed zone may also be significant even in these cases (Savage et al., 1976).

Partially melted zone

The partially melted zone is the narrow band region between unmixed zone and true heat-affected zone. This base metal has undergone only partial melting during welding. Localised melting is caused by the variation of the effective melting temperature from place to place, which is due to the point-to-point variations in solute content in the base metal. In the partially melted zone, the grains near the fusion boundary are smaller than those in the nearby region of the true heat-affected zone where no localised melting was present (Savage, 1978).

2.3.3 Inhomogeneity of element distribution in welds

2.3.3.1 Solidification of welds

The mechanisms of weld metal solidification can be described, based upon the following boundary conditions (Savage, 1978, Porter, 1992): **(i) No diffusion in the solid.** This is a good approximation since the cooling rate is very high during weld metal solidification; **(ii) No convective mixing in the liquid.** As discussed by Savage et al. (1976), an unmixed zone at the solid-liquid interface is a stagnant layer which has not experienced enough convective mixing during weld solidification; thus this is also a good approximation since the extent of the diffusion zone in the liquid is small in comparison to the thickness of the stagnant layer (unmixed zone) in the liquid at the advancing solid-liquid interface. **(iii) Only diffusion mixing in the liquid.** Concentration changes in the liquid occur by diffusion alone.

In the case of welding, the weld metal forms by the growth of the solid into the liquid at solid/liquid interface. The microstructural characteristics of the weld metal are determined by the stability of the solid-liquid interface, which is affected by the conditions in the immediate vicinity of the interface. Several structural morphologies may develop which, generally, may be divided into planar, cellular, columnar dendritic and equiaxed dendritic growth, as schematically shown in Figure 2.12 (David and Vitek, 1989). The conditions which control which growth form dominates largely depend on the following parameters: growth rate, temperature gradient, undercooling and alloy constitution (David and Vitek, 1989, Savage, 1978). The growth rate (R) and temperature gradient (G) influence the solidification morphology in the combined form of G/R and influence the scale of the solidification substructure in the form of GR (cooling rate). It is known that G/R ratio is very important in determining the degree of constitutional supercooling. As shown in Figure 2.13 (Kou, 1987), when the actual temperature gradient in the liquid is so steep to be above the effective liquidus profile, planar growth prevails. When the actual temperature gradient is less steep, some part of the actual temperature gradient line lies below the effective liquidus profile, which then promotes cellular growth. With increasing constitutional supercooling, columnar dendritic and equiaxed dendritic growth will be dominant. On the other hand, cooling rate in the form of GR also affects the solidified substructure. The greater the product GR , the finer the cellular, columnar dendritic and equiaxed dendritic structure. The effect of temperature gradient G and solidification rate R can be summarized in the schematic diagram in Figure 2.14 (Giamei et al., 1976).

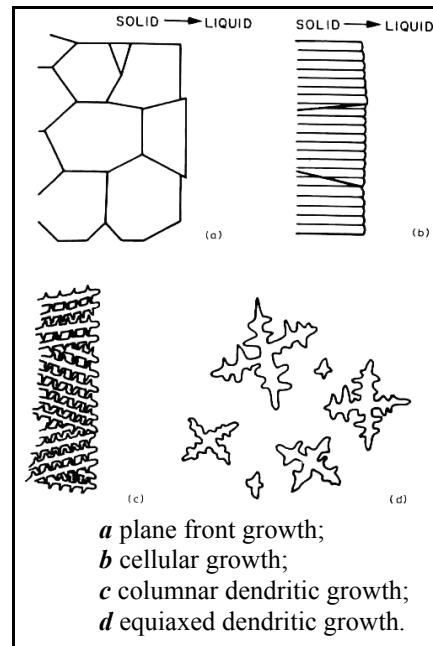


Figure 2.12 Various structural morphologies possible during solidification (David and Vitek, 1989)

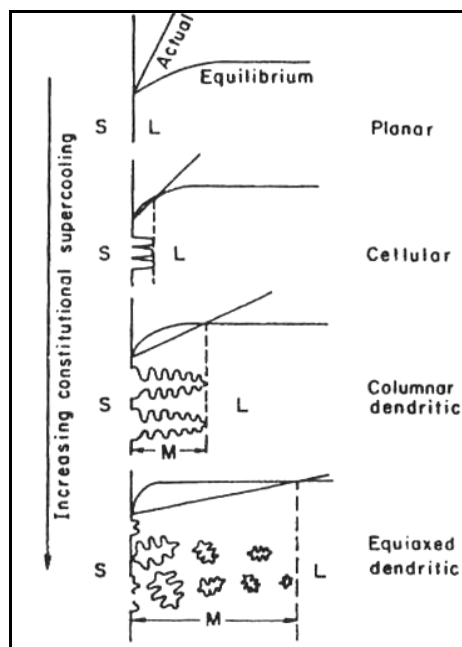


Figure 2.13 Various solidification growth modes as a function of the relative degree of constitutional supercooling (Kou, 1987)

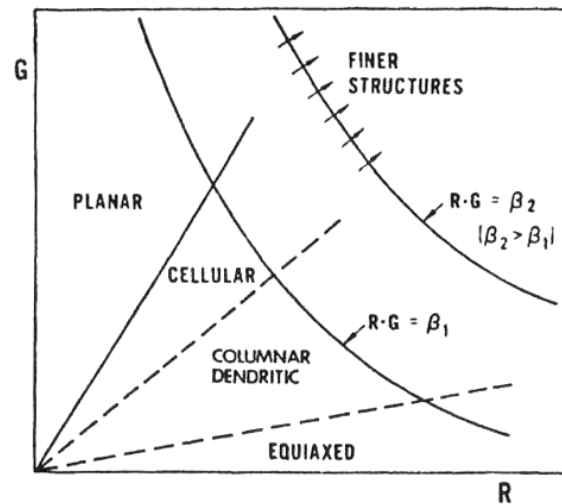


Figure 2.14 Schematic growth rate (R) vs. temperature gradient (G) map showing transitions in solidification growth mode and the refining effect of high cooling rate (Giamei et al., 1976)

In the case of weld pool solidification shown in Figure 2.15 (Messler, 1999), the solidification modes at different positions on the solid-liquid interface are different due to their different combination of thermal gradient G and growth rate R . The thermal gradient G in the liquid decreases continuously from the fusion line to the weld centreline. The growth of the solid will generally occur in the direction of the maximum temperature gradient. The nominal crystal growth rate R_n varies with position along the fusion boundary. Taking the angle between the R_n and the welding direction to be ϕ , the nominal growth rate R_n becomes,

$$R_n = v \cos \phi \quad [2.3]$$

where v is the welding velocity. In the case of dendritic growth, the actual dendrite growth rate R has an angle ψ with the welding direction. It can be defined as,

$$R = \frac{v \cos \phi}{\cos(\phi - \psi)} \quad [2.4]$$

It suggests that the growth rate of the solidification front R is equal to the welding velocity v at the weld centreline and decreases toward the fusion boundary, where R is equal to 0.

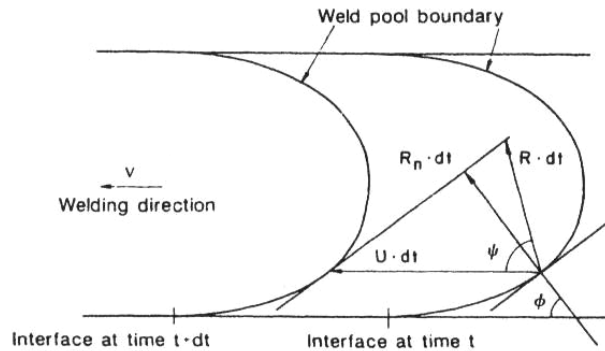


Figure 2.15 Relationship between welding velocity (v) and solidification growth rate (R) (Messler, 1999)

In light of the effects of thermal gradient G and growth rate R on the morphology of the solidified structure indicated in Figure 2.14, the microstructural distribution in the fusion zone of the weld is generally as shown in the schematic diagram in Figure 2.16 (David and Vitek, 1989). It can be seen that near the fusion boundary on the two sides of the weld bead, planar growth occurs. It changes to cellular growth, columnar dendritic growth and equiaxed dendritic growth toward the centreline.

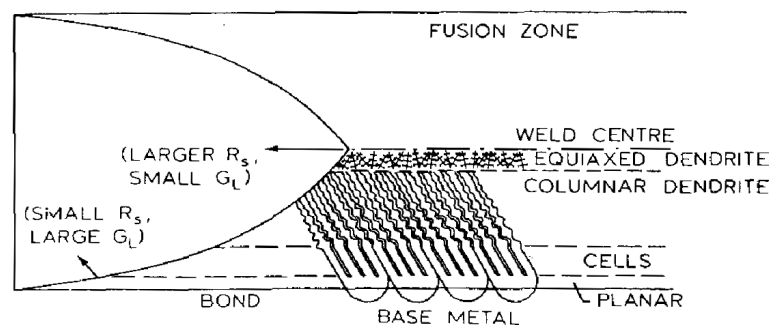


Figure 2.16 Schematic drawing of structural variation of weld microstructure across fusion zone (David and Vitek, 1989)

2.3.3.2 Solute partition during weld solidification

The solidification of an alloy is commonly subdivided into three cases according to solidification conditions (Porter, 1992, David and Vitek, 1989, Messler, 1999):

Case 1: Infinitely slow solidification (equilibrium solidification), where equilibrium is maintained at all times and complete solid and liquid diffusion take place. No composition gradient exists anywhere. A uniform solid with nominal alloy composition will be achieved finally.

Case 2: Solidification with no diffusion in the solid but perfect mixing in the liquid (Scheil solidification). In this case, the rapid cooling rate will not allow substantial diffusion in the solid. But it is assumed that the liquid composition is kept homogeneous as a result of efficient convection and diffusion. This kind of solidification is called Gulliver-Scheil solidification.

Case 3: Solidification with no diffusion in the solid and only diffusion mixing in the liquid. Since there is no convective mixing in the liquid, the changes in the composition in the liquid occur by diffusion only.

According to conditions of the weld metal solidification discussed before, Case 3 is more appropriate for describing morphological stability and microstructural development in welds (David and Vitek, 1989). There is always a stagnant layer (unmixed zone) in the liquid at the advancing solid-liquid interface. Within this layer, no convective mixing occurs but only diffusion mixing. Compared to the thickness of this layer, the extent of diffusion in the liquid is small.

The solute redistribution at the solid-liquid interface is responsible for the composition variations occurring during the solidification of the weld metal. As shown in the schematic phase diagram in Figure 2.17 (Stefanescu, 2002), an alloy with nominal solute composition C_0 will begin to solidify at T_L with the formation of the first solid with the composition k_0C_0 . k_0 is the equilibrium partition coefficient, which is defined as $k_0 = C_S / C_L$, where C_S and C_L are the equilibrium concentrations of solid and liquid phase at a given temperature T_i . Although in a real system, k_0 may vary with temperature because of the curvature of the liquidus and solidus lines, for dilute solutions, k_0 can be assumed to be essentially

constant. The equilibrium partition coefficient between solid (δ) and liquid iron, $k_0^{\delta/L}$ for some elements in binary iron alloys can be found in Table 2.4 (Stefanescu, 2002).

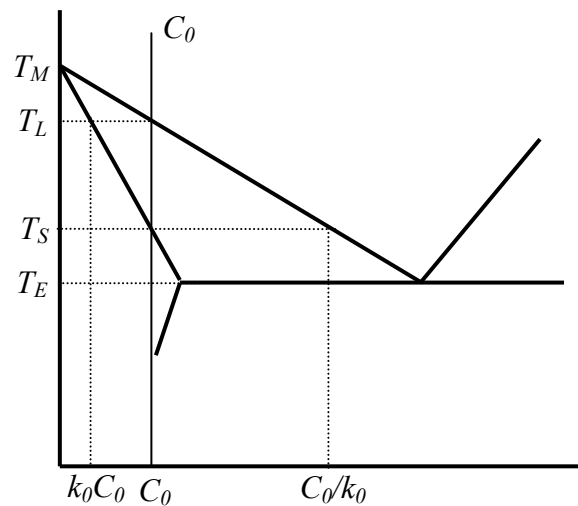


Figure 2.17 Schematic phase diagram showing solute partition during solidification of an alloy with nominal solute composition C_0

Dissolved element	Partition coefficient, k_0
H	0.297
N	0.281
S	0.052
P	0.16
C	0.11
Mn	0.73
Si	0.77
Cr	0.94
Al	0.7

Table 2.4 The equilibrium partition coefficient $k_0^{\delta/L}$ between solid (δ) and liquid iron for some elements in binary iron alloys (Stefanescu, 2002)

Obviously, since mass must be preserved, any solute atoms that do not appear in the newly formed solid must be left behind to appear in the liquid, thereby raising the composition of the liquid along the liquidus line (Messler, 1999). In the case 3 with only diffusion mixing in the liquid, the solute rejected from the solid accumulates in the liquid near the solid-liquid interface. A diffusion layer will exist ahead of the interface. As shown in Figure 2.18 (Stefanescu, 2002), three distinctive zones are seen:

- I. The initial transient, between T_L and T_S : because of the boundary layer
- II. The steady state, at T_S : solute concentration in liquid is a constant C_0/k_0
- III. The final transient between T_S and T_E : build-up of solute occurs because the boundary layer reaches the end of the crucible

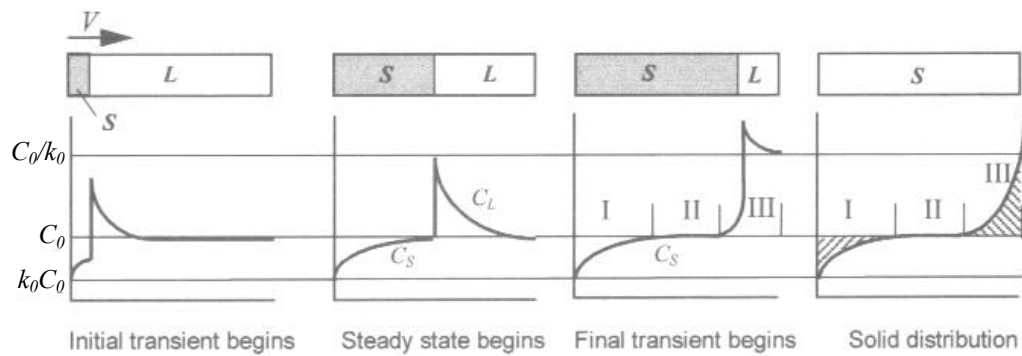


Figure 2.18 Solute redistribution during planar-front solidification

The solute redistribution during the initial transient can be expressed by the following equation (Stefanescu, 2002; Kruz and Fisher, 1989, Brody and Flemings, 1966),

$$C_s = C_0 \left[1 - (1 - k_0) \exp\left(-k_0 \frac{R}{D} x\right) \right] \quad [2.5]$$

An exact solution was also developed to the initial transient variations in the solid (Smith, 1948; Tiller et al., 1953; Tiller and Rutter, 1956),

$$C_s = 2C_0 \left\{ 1 + \operatorname{erf} \sqrt{\frac{R}{2D}} x + (2k_0 - 1) \exp \left[-k_0(1 - k_0) \frac{R}{D} x \right] \times \operatorname{cerf} \left[\frac{(2k_0 - 1) \sqrt{\frac{R}{D}}}{2} x \right] \right\} \quad [2.6]$$

where in both equation [2.5] and [2.6], C_0 is the nominal solute composition of the alloy (at. fraction), R is the growth rate of solid (m/s), D is the diffusion coefficient in the liquid (approximately 5×10^{-9} m²/s), x is the distance from the initial solid-liquid interface to the moving solid-liquid interface (m).

Within the initial transient zone, the solid concentration in the liquid changes from $k_0 C_0$ in the first solid to C_0 when the steady state is achieved. Both solutions above predict virtually same length of the initial transient, which can be expressed approximately by following equation,

$$d_i \cong \frac{5D}{k_0 R} \quad [2.7]$$

where d_i is the length of the initial transient region (solute partitioned region) (m).

2.4 CREEP PROPERTIES OF P91 AND 9-12% CHROMIUM STEELS AND WELDS

2.4.1 Introduction to creep

Creep is a term used to describe the material deformation occurring as a result of long term exposure to levels of stress which is lower than the yield or ultimate strength of the materials, and at a sufficiently high temperature, usually greater than approximately 0.4 of the absolute melting temperature T_m (Evans, 1984, Evans and Wilshire, 1985). This creep strain is thermally activated and leads eventually to specimen or component failure. Creep is a function of stress, temperature, time and material itself. At a given temperature and stress level, creep is a time-dependent deformation process. Creep failure does not happen upon sudden loading, but the material permanently strains over a long period until it finally fails.

A typical creep curve showing the variation of creep strain with time subjected to a constant tensile stress σ_a is shown schematically in Figure 2.19. There are three stages during creep: Primary stage (transient stage), secondary stage (steady-state stage) and tertiary stage (rupture stage). In the primary or transient stage, after the initial strain on loading, the creep rate decreases gradually to a constant value. During this stage, the strain is a combination of elastic and plastic deformation. The increase in the dislocation density results in a decrease of creep rate. In the secondary stage, the rate of strain hardening by dislocations is balanced by the rate of dislocation recovery, so the creep strain rate is apparently constant and reaches a minimum, namely the minimum creep rate, as indicated in Figure 2.19. This is why this stage is also called the steady-state stage. The creep in this stage is governed by two creep mechanisms: dislocation creep and diffusional creep, which will be discussed in the next section. The tertiary stage is characterised by the steep increase in strain rate which starts to cause the formation of creep damage voids in materials. This voiding will cause an increase in the local stress of the component which further accelerates the strain, eventually leading to the final rupture. For some materials, the primary stage may be absent or have an inverted form and similarly, the extent of the tertiary stage may be limited in some relatively brittle materials and very extensive in ductile

ones (Evans, 1984). The classic three-stage creep curve in Figure 2.19 is frequently observed for creep of metals.

The time from the first application of stress to the final rupture of the material is called the creep failure life at a particular stress and temperature. The total strain along the stress axis after creep rupture is called the total elongation.

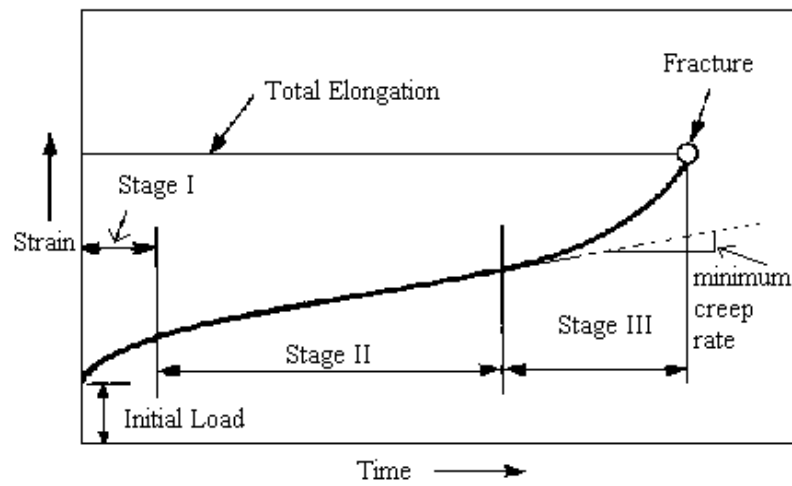


Figure 2.19 Schematic representation of a high temperature curve (strain vs. time) at constant stress and temperature (Evans and Wilshire, 1985)

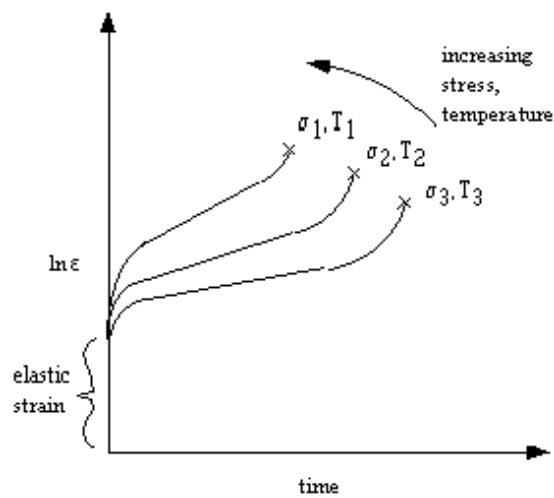


Figure 2.20 Effect of temperature and stress on strain vs. time creep behaviour (Evans, 1984)

Stress and temperature are two important factors in creep. The effect of stress and temperature on the creep curve is shown in Figure 2.20. With increasing stress and temperature, the minimum creep rate increases and the creep failure life decreases. Creep strain rate is very sensitive to temperature. The relationship between creep strain rate ($\dot{\epsilon}$) and temperature (T) can be expressed as the Arrhenius law as follows (Evans and Wilshire, 1993; Lagneborg, 1979),

$$\dot{\epsilon} = A \exp\left(-\frac{Q_c}{RT}\right) \quad [2.8]$$

where $\dot{\epsilon}$ is the creep strain rate, A is material-dependent constant, Q_c is the activation energy for creep which is constant for a given creep mechanism, R is the universal gas constant, and T is the absolute temperature (K).

The relationship between the steady-state creep rate $\dot{\epsilon}_s$ and stress σ can be expressed by Norton's law equation,

$$\dot{\epsilon}_s \propto \sigma^n \quad [2.9]$$

where n is the creep index, and has a value typically between 3 and 6 for single-phase materials.

It is widely assumed that the parameter of greatest significance is the secondary or steady-state creep rate $\dot{\epsilon}_s$, the slope of the secondary stage of typical high temperature creep curves (Figure 2.19), due to its extended duration. The steady state or minimum strain rate is often used in life calculation. The way in which the steady state creep rate $\dot{\epsilon}_s$ varies with both stress and temperature can be defined as,

$$\dot{\epsilon}_s = u(\sigma) \cdot v(T) \quad [2.10]$$

Substituting for $v(T)$ using the equation [2.8] and for $u(\sigma)$ using Norton's law equation [2.9], the power law relationship of creep strain rate $\dot{\epsilon}_s$ with stress σ and temperature T can be expressed as,

$$\dot{\epsilon}_s = A\sigma^n \exp\left(-\frac{Q_c}{RT}\right) \quad [2.11]$$

The value of Q_c has frequently been found to be close to the activation energy for lattice self diffusion Q_{SD} , but it is not always equal to Q_{SD} (Evans and Wilshire, 1993).

Creep is controlled by several different mechanisms depending on the material itself and the creep conditions, namely stress and temperature. There are two dominant mechanisms that contribute to the creep in metals: diffusional creep and dislocation creep, depending on the applied stress and the temperature at which the test is performed (Evans and Wilshire, 1993).

2.4.2 Evolution of microstructure and material properties during creep

The 9-12%Cr heat resistant steels, including P91 steel, have been extensively applied in power plant under high stress and elevated temperature exposure. Their creep behaviours have also been widely studied to pursue better performance and longer service life. The microstructural evolution brought about by creep exposure has been investigated because of the dependence of the properties on the microstructure (Agyakwa et al., 2003; Ennis et al., 1998; Kubon et al., 1998). For 9-12%Cr steels, the evolution of the microstructure mainly involves the strengthening and coarsening of precipitates, the recovery of the martensite lath structure and dislocations, and thermal softening (Gladman, 1998).

2.4.2.1 Precipitates

The 9-12%Cr steels have their superior high temperature creep resistance largely attributed to their chemical composition which was designed by balancing austenite and ferrite stabilizers to produce 100% austenite during austenitisation

and 100% martensite during a quenching treatment following austenitisation (Klueh, 2005). Moreover, the creep strength of the materials is also determined by those elements which confer solid solution strengthening and precipitation strengthening effects (Anderson et al., 2003).

It is known that dislocation motion is one of the important mechanisms of creep. Precipitates dispersed in the materials can act as obstacles for dislocation motion. Enough stress needs to be applied to force the dislocations to climb over those precipitates to enable creep deformation to proceed, and so materials with large numbers of precipitates normally possess higher creep strength.

In the 9-12%Cr steels, especially P91 steel containing also molybdenum, vanadium and niobium, the formation of large number of precipitates can obstruct the dislocation motion, leading to higher creep strength. The chromium carbides Cr_{23}C_6 are the dominant precipitates in 9-12%Cr steels due to the high chromium content in the steels. They form in the quenched and tempered condition mainly at the prior austenite grain boundaries and subgrain boundaries but with a small amount of them were also found in the martensite lath interior but at a much finer scale. Although this type of precipitate was found to improve the creep strength of the material in the short term, the strengthening effect is reduced at the later stages of the service by precipitate coarsening. The evolution of the particle mean size d can be described by the Ostwald ripening law (Orlova et al., 1998),

$$d^3 = d_0^3 + k \cdot t \quad [2.12]$$

where d_0 is the initial particle size at $t = 0$ and k is the particle growth rate.

Precipitate coarsening is detrimental to the creep strength of the materials in that it diminishes the limiting effect of grain boundary precipitates on subgrain growth. When the particles grow to a larger size which exceeds a critical size, the strengthening effect of the precipitates will decrease. Furthermore, these large grain boundary precipitates can act as the initial locations for the formation of the grain boundary creep cavitation, which results in the grain boundary sliding as the onset of the tertiary creep stage.

However, not all precipitates coarsen during creep so rapidly, such as the minor precipitates in the form of MX in the subgrain interior. Klueh (2005) performed creep testing on P9 and P91 steels. The results showed that the presence of elements such as vanadium, niobium and nitrogen gave P91 steel an advantage of creep strength over P9, even though they have similar chromium and carbon contents. Moreover, MX precipitates in the subgrain interior did not exhibit the rapid coarsening exhibited by chromium carbide $Cr_{23}C_6$ in long term creep exposure. The MX precipitates based on molybdenum, niobium, vanadium, titanium and tungsten are resistant to coarsening (Nawrocki et al., 2000, Tamura et al., 2003). Compared to the $Cr_{23}C_6$ particles at subgrain boundaries, which coarsen during creep but with approximately constant or lower numbers of precipitates and therefore larger inter-particle space, MX precipitates in the subgrain interior were generally found to increase both in size and relative numbers with increasing time at a given temperature (Klueh, 2005). With increasing temperature, the relative number and average size of the MX precipitates were both found to increase. The small amount of $Cr_{23}C_6$ precipitates within the martensite lath were found to decrease in both average size and relative number, indicating that they dissolved and reprecipitated on the coarse $M_{23}C_6$ precipitates at grain boundaries (Anderson et al., 2003). Although the MX precipitates are found to offset the loss in creep strength due to the coarsening of the $Cr_{23}C_6$ precipitates after long term creep exposure, the loss of the creep strength by the coarsening of $Cr_{23}C_6$ precipitates overwhelms the strengthening effect of MX precipitates, leading to the formation of creep cavitation and deformation of the materials.

2.4.2.2 Recovery of martensite and dislocations

In addition to the evolution in precipitate morphology and distribution, the well-developed martensite laths, namely subgrains, with low dislocation density in their interiors are also the important characteristic features of long-term creep exposed materials (Ennis and Czynska-Filemonowicz, 2003). Figure 2.21 (Sawada et al., 1999, Sato et al., 2000) shows a typical example of the recovery of subgrains and dislocations observed in three high chromium steels during creep at 650°C and a stress level of 98 MPa. With the progress of creep deformation, the subgrain width increases and the free dislocation density decreases.

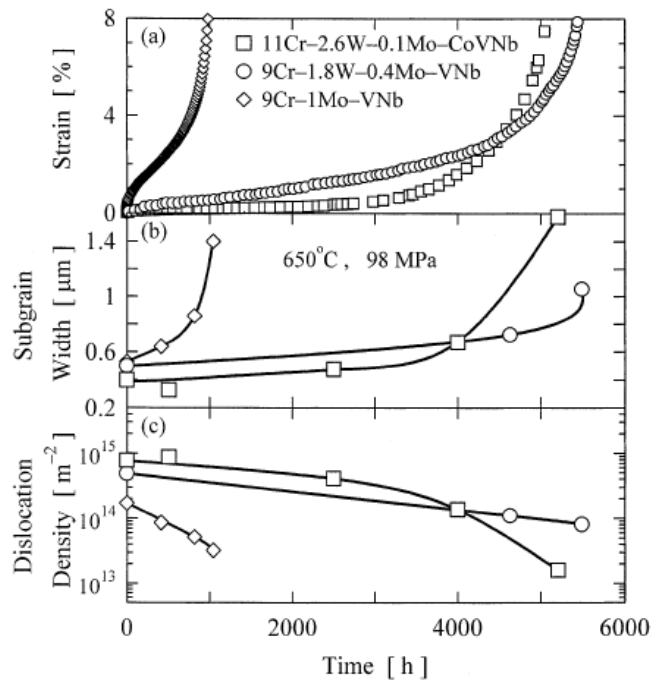


Figure 2.21 (a) Creep curves, and changes in (b) subgrain width and (c) free dislocation density within subgrain during creep of three chromium ferrite steels at 650°C under 98 MPa (Sawada et al., 1999)

Along with the subgrain size growth, it is observed that subgrains tend to an equiaxed shape, instead of the martensite lath shape. Orlova et al. (Orlova et al., 1998) found that subgrain growth in the gauge section of creep specimens is more pronounced than the growth in the head of creep specimens where the material is only subjected to high temperatures. This region experiences lower applied stress and lower creep deformation during the testing. According to the suggestion of Raj and Pharr (Raj and Pharr, 1986) deduced from an analysis of a large collection of data, the subgrain size d can be expressed as follows:

$$d = K \cdot b \cdot \left(\frac{G}{\sigma} \right)^m \quad [2.13]$$

where K is a dimensionless constant, b is the Burgers vector length, G is the shear modulus, σ is the applied stress and m is an exponent, $0 < m < 2$.

The high creep strength of 9-12%Cr steels is also attributed to the high dislocation density of the tempered martensite structures. During the creep process, dislocations move by glide and climb, resulting in the deformation of the material. If the stress is high enough, the dislocations can cut or loop those obstacles such as precipitates, grain boundaries and other dislocations. On the other hand, the evolution of precipitates and grain boundaries during creep such as the increasing inter-particle spacing or increasing width of subgrains, also make dislocation motion easier.

2.4.2.3 Softening / Hardness

Hardness is a parameter which may give an indication of the creep strength of the materials. Its well established relationships with other mechanical properties, such as yield stress, elongation and fatigue, make hardness evaluation useful in obtaining plastic flow and strain hardening parameters associated with creep of the materials (Kohlhofer and Penny, 1996).

The qualitative relationship between hardness and creep properties has been studied extensively and is well documented (Okada et al., 2002, Park et al., 2005, Klueh, 2005, Orlova et al., 1998). The degradation of the hardness due to long time exposure at elevated temperature has been observed by hardness testing on aged materials. It has been shown that the hardness reduces with increasing temperature and thermal exposure duration. The hardness value of P91 steel as a function of the Hollomon-Jaffe Parameter P (or Larson-miller Parameter) was plotted by Agyakwa et al. (2003), as shown in Figure 2.22.

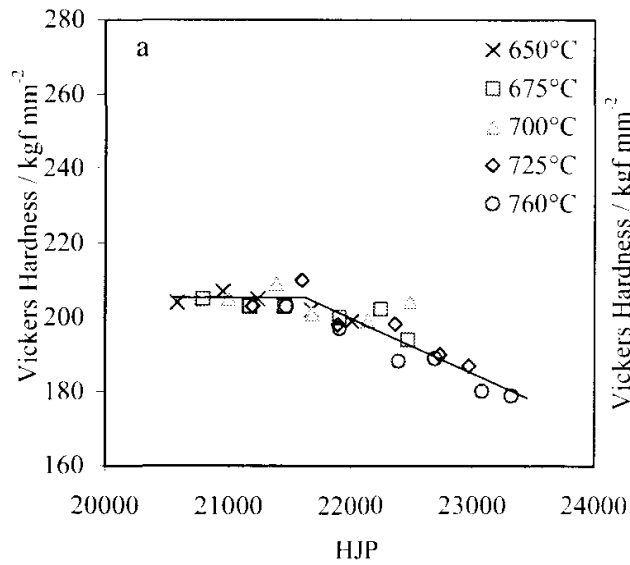


Figure 2.22 Effect of thermal exposure on hardness as a function of HJP (or P)
(Agyakwa et al., 2003)

The HJP parameter / Larson-Miller parameter is given by:

$$P = T(20 + \log t) \quad [2.14]$$

where T is the exposure temperature in Kelvin and t is the exposure time in hours. The figure shows that the hardness is relatively insensitive to tempering up to a HJP value then drops with further increase in HJP .

The effect of stress on the degradation of hardness was also investigated through the hardness testing on both aged and stress-aged 2.25Cr-1Mo steels by Watanabe et al (2004). The stress-aged specimen had a much lower hardness value than that of the aged specimen. It was argued that the difference in the changes of hardness between the aged specimen and stress-aged specimen indicated that stress has significant effect on hardness degradation during creep. It was again been argued that higher applied stress normally leads to more rapid degradation of hardness (Tanaka et al., 2001). Both the coarsening of carbides and the recovery of dislocations have been regarded as the sources of such hardness difference (Watanabe et al., 2004; Fujiyama et al., 1990). Whilst, many authors regard this is a stress effect, it is also possible that this is a strain effect, since the two are inseparable in experiments.

The quantitative relationship between hardness and creep rate or between hardness and creep rupture time is often evaluated by the plots of Larson-Miller parameter P as in equation [2.14] (Fujiyama et al., 1990; Klueh, 2005).

2.4.3 Creep failure mechanism of P91 welds

The low creep strength of the weldment structures is different to that of normal steels and results from their complex and heterogeneous structures formed during the welding thermal cycle. A typical weld structure consists of parent metal, heat-affected zone (HAZ) and weld metal which all have different creep properties. The failure modes of the weld under creep have been well studied previously and some conclusions have been drawn (Francis et al., 2004; Issler et al., 2004). Failures have been categorised according to the position of the creep fractures within the weld structure. Type I mode occurs within the weld metal and is confined to the weld metal, whereas Type II mode also occurs within the weld metal but may grow out of the weld into the plate. Type III and Type IIIa modes occur in the coarse grained region of HAZ (CGHAZ) close to the fusion boundary. However, the Type III is actually the reheat cracking arising in this location early in life, which is caused by the creep strain absorbed during the decay of residual welding stress exhausting low local ductility; Type IIIa occurs later in service, in more ductile microstructural regions as a result of long term system load (Brett, 2004). Type IV mode occurs in the low temperature region of the HAZ, typically the intercritical HAZ (ICHAZ). In addition, creep cracking has also been found at the inter-bead fusion boundaries (weld bead to weld bead) (Allen et al., 2005, Zhang et al., 2007), different from Type IIIa which occurs adjacent to the fusion boundaries of weld bead to parent metal. Among these failure modes, although Type IV creep failure in the HAZ has been considered as the most important life-limiting failure mechanism in practice, creep failure in weld metal has also been found by some researchers and showed the importance of understanding of creep mechanisms of the weld material itself (Mannan and Laha, 1996; Watanabe et al., 2004; Fujibayashi et al., 2004). However, the creep behaviour of the weld metal itself has not been extensively studied and documented, with most previous research being based on the empirical and numerical approaches, rather than being based on metallurgical studies of evolution of the materials and properties

during creep. Investigating the creep properties of the weld metal itself is also essential to establish the creep model of the weld metal.

2.4.3.1 Type IV cracking in ICHAZ

Type IV cracking, namely intercritical heat-affected zone (ICHAZ) cracking, is a well known problem in ferritic steels. It is named after a German classification of weld cracking modes and has been found both in low and high chromium Cr-Mo steels (Schuller et al., 1974). It normally occurs in a circumferential mode just outside of the fully transformed HAZ region adjacent to the parent metal, leading to the inferior creep strength of the weldment compared to those of both the parent and weld metal. During welding, the intercritical heat-affected zone (ICHAZ) is heated to a maximum temperature between A_{c1} and A_{c3} , where the phase transformation from α to γ only partially proceeds during the thermal cycle (Gaffard et al., 2005). This leads to the existence of some soft ferrite in ICHAZ. Moreover, because the peak temperature of the heating cycle is not very high and its duration is short, many of the precipitates do not dissolve in the austenitic matrix, unlike in the CGHAZ, where the dissolution of the precipitates is typically completed due to the higher peak temperature. The ICHAZ has essentially a very fine structure consisting of subgrains with low dislocation density. Hardness measurement carried out on cross-weld specimens reveal that ICHAZ has lowest hardness, which is even lower than that of parent metal (Albert et al., 2003; Wu et al., 2004). A typical Type IV creep failure of 9Cr-1Mo-V-Nb steel weld is shown in Figure 2.23 and the hardness profile across the weld metal is shown in Figure 2.24 (Watanabe et al., 2006), indicating the lowest hardness in the ICHAZ.

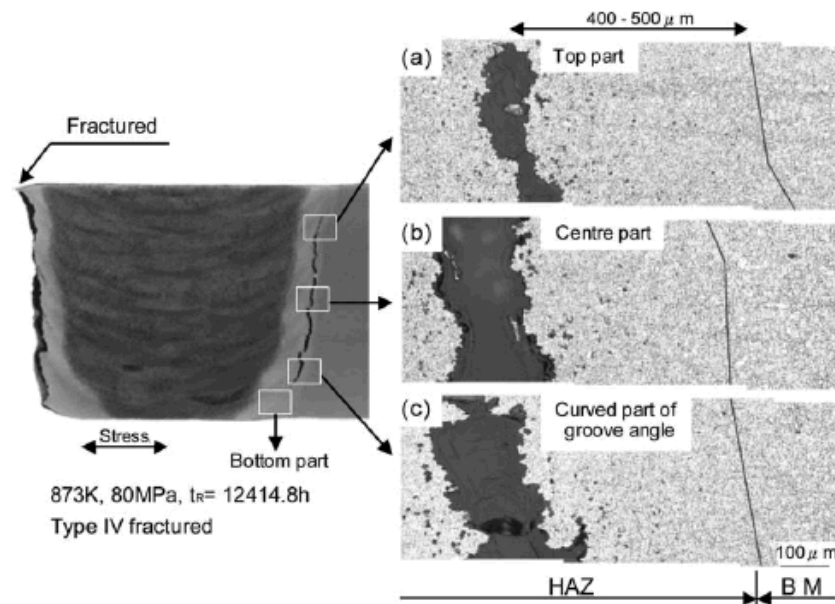


Figure 2.23 Profile and optical microstructures of the Type IV fractured welded joint specimen (Watanabe et al., 2006).

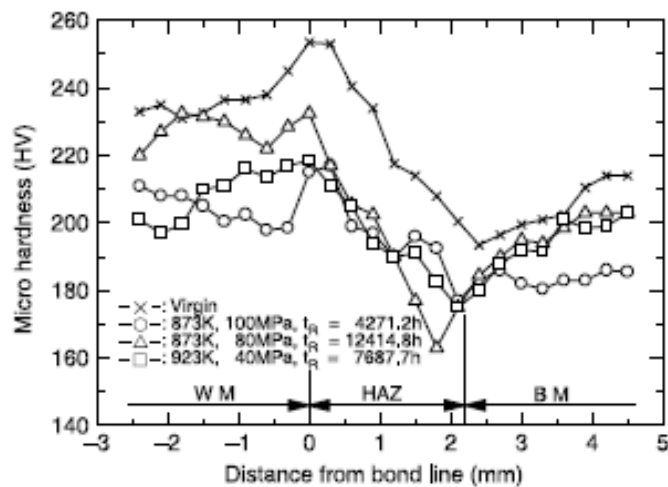


Figure 2.24 Hardness variations in the base metal (BM), heat-affected zone (HAZ) and weld metal (WM) (Watanabe et al., 2006)

After creep exposure, creep cavities and microcracks tend to form in the ICHAZ which is partially transformed and over tempered. The failure mechanism is therefore by the creep of locally constrained regions under the action of some additional operating process (Wu et al., 2004). The coarsening of the $M_{23}C_6$ carbides and the absence of any secondary reprecipitation of fine MX particles

during tempering and creep exposure have been identified as the major mechanisms accelerating the relatively poor creep response of the ICHAZ (Spigarelli and Quadrini, 2002).

2.4.3.2 Type I weld metal failure

Weld metal failure is also called type I failure, happening on the outer weld metal surface. The cracks are the result of the nucleation, growth and linkage of creep cavities. The cracks are oriented transversely across the weld metal, along the prior austenite grain boundaries in the coarse columnar weld metal. They are normally constrained by the refined region adjacent to the weld beads, which are more ductile and resistant to cracking. In the work of Watanabe et al. (2006), creep tests of 9Cr-1Mo-V-Nb welded joints at 823K, 873K and 923K with different stress levels showed that the failure location of the welded joint specimens changes from the weld metal in the higher stress and shorter time condition to the HAZ in the lower stress and longer time condition. Work by Fujibayashi et al. (2004) on the creep behaviour of 2.25Cr-1Mo steel weldment showed that twenty-four out of thirty-three cross-weld specimens failed in the centre of weld metal. Type I failure of 2.25Cr-1Mo steel welds could be a serious threat to actual components operated at low stress levels. Weld metal failure in a 2.25Cr-1Mo weldment also has been found by Gooch and King (1978). The cracks are intergranular and form preferentially in the columnar regions of the weld metal, often close to the fusion boundary.

Both Watanabe et al. (2006) and Fujibayashi et al. (2004) agreed that the stress level affects the creep failure mode of the weld joints. However, Watanabe et al. suggested that weld metal failure occurred in the higher stress conditions, whereas the latter stated that it happened at lower stress. In addition, the former authors also considered temperature as an influencing factor of failure location. According to Mannan and Laha (1996) and previous researchers (Coleman, 1981), this type of weld metal cracking normally occurs in low chromium Cr-Mo steel weldments, but is not as common for high chromium Cr-Mo steel weldments.

2.4.3.3 Type IIIa weld interface failure

Most of the weld interface (weld metal/HAZ) failures reported are found in dissimilar weldments. Differing from homogeneous welds, due to the difference in chemical composition and mechanical properties between parent metal and weld metal, the weld interface experiences very complicated metallurgical changes during welding, heat treatment and service at elevated temperature, leading to the defects at or near the weld interface and mismatches in mechanical properties. So cracks preferentially form at or near the weld interface and propagate to become macro-scale cracks along the interface during long term creep exposure, until the final rupture.

Schuller et al. (1974) has introduced the term 'IIIa' for the interfacial cracks, which lie within the heat affect zone (HAZ) close to the weld fusion line. It was found that Type IIIa creep failure is associated with carbon migration across the weld interface. Laha et al. (2001a) found that the creep failure in a 2.25Cr-1Mo / INCONEL 182 dissimilar weld joint occurred in type IIIa zone near to the weld interface at stresses below 150 MPa, and in the type IV zone at stresses over 150MPa. They did not find type IIIa failure in 2.25Cr-1Mo similar weld joints at any stress level. In contrast to type IV Creep failure, which is due to the low creep strength as a result of the weld thermal cycles at the outer edge of the HAZ, the Type IIIa zone has the creep strength comparable to that of the weld metal. To explain why any weld should fail in the type IIIa zone, Brett (2004) and other researchers (Lundin, 1982; Laha et al., 2001b; Laha et al., 2001a) have found an important factor, which is the carbon depletion at the fusion boundary, a process which starts during post weld heat treatment and continues with operation at service temperature.

For dissimilar welding, it is easier to understand the formation of the carbon depleted zone at the fusion boundary within the parent metal, which is caused by carbon diffusion from the parent metal to the weld metal (or vice versa) due to the carbon gradient. Due to the local migration of the carbon, there are carbon-depleted regions and carbon-rich regions formed. The carbon-depleted region locates on the low alloy side (typically parent metal) of the weld interface and has an appearance of the light-etched white band along the fusion boundary. The carbon-rich region is parallel to the carbon-depleted region on the high alloy side

(typically weld metal) and is a darker etched zone. The precipitates are absent in the carbon-depleted region and rich in the carbon-rich region, predominately in the form of $M_{23}C_6$ carbides. In dissimilar chromium steel welds, the light-etching carbon-depleted region normally consists of large ferrite grains, which is relatively soft and has lower creep strength. The depletion of carbon in this region caused the recrystallisation, and grain growth can also be observed in the soft zone due to the absence of the pinning effect of carbides (Sudha et al., 2002). The low creep strength makes the carbon-depleted region the most vulnerable region in a weld joint (Kasatkin and Tsaryuk, 1967). However, another phenomenon found by Allen et al. (2005) is that the creep cracks observed primarily lie on the edges of the carbon-depleted zone, rather than inside the zone, since creep cavitation is nucleated by intergranular inclusions in adjacent materials and the discontinuity between carbon depleted zone and normal materials may also increase the susceptibility to creep cavitations.

Carbon depletion at the fusion boundary can also be possible even when the carbon content is same between parent metal and weld metal in a dissimilar weld. The diffusion of carbon is actually driven by the difference of carbon activity rather than the difference of carbon concentration between parent metal and weld metal. Laha et al. (2001a; 2001b) have found the carbon-depleted zone in 2.25Cr-1Mo/9Cr-1Mo dissimilar weld joint where the carbon content is same in the parent metal and the weld metal (0.12%wt) as shown in Figure 2.25. The carbon migration here is caused by the difference of carbon activity due to the different chromium content. Brett (2004) also mentioned the dissolution and growth, respectively, of the $M_{23}C_6$ type carbides as the reason for the carbon depletion at the fusion boundary.

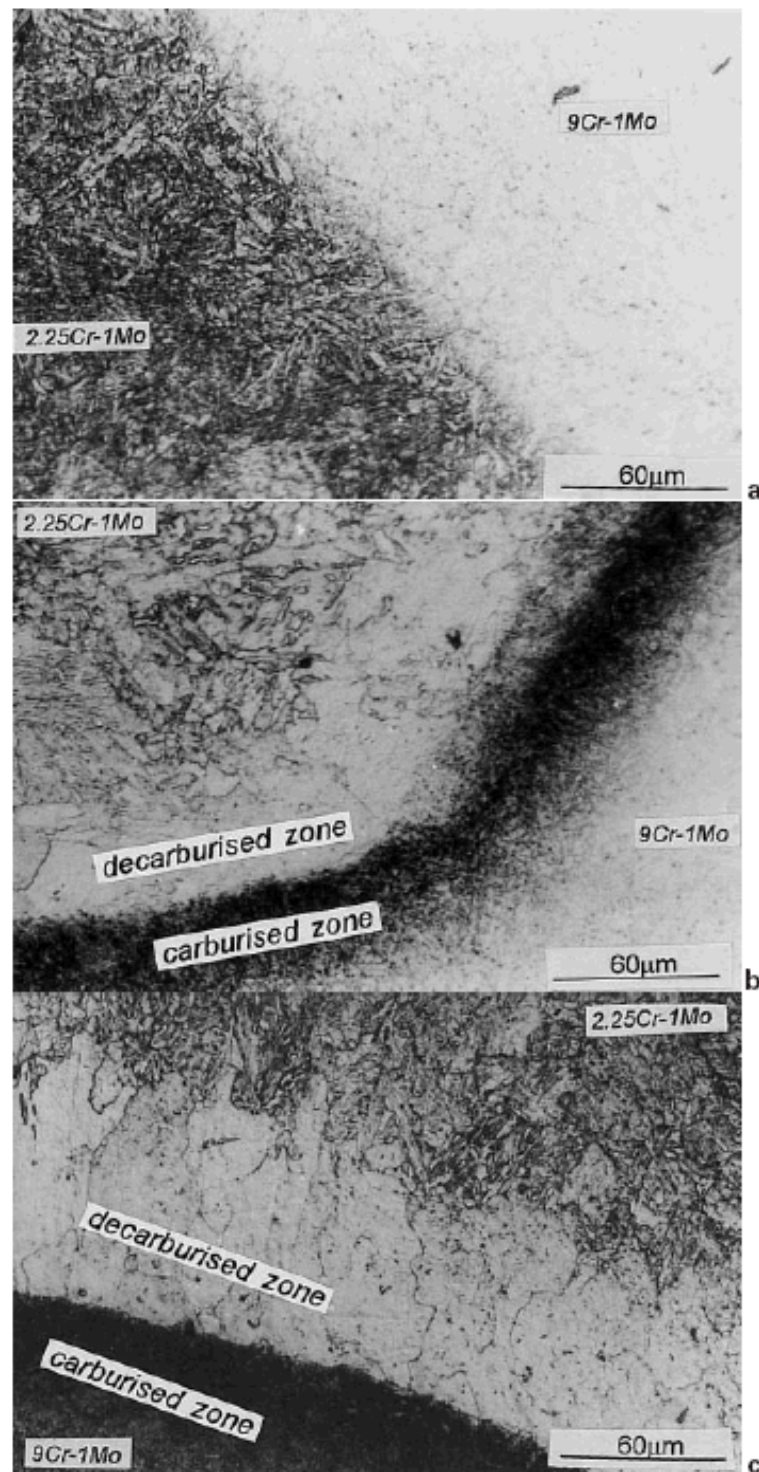


Figure 2.25 Microstructure across weld interface of 2.25-1Mo steel base metal and 9Cr-1Mo steel weld metal of dissimilar joint in various conditions: (a) as-welded; (b) PWHT; (c) creep tested (130MPa, 823K) (Laha et al., 2001b)

2.4.3.4 Inter-bead boundary creep failure (weld bead to weld bead)

This type of creep fracture, although not well documented, has been found on both P91 (Zhang et al., 2007) and P92 weld metal (Allen et al., 2005). It normally occurs at some light-etched white-bands formed along the inter-bead boundaries within the weld metal. Some common features have been found between the inter-bead boundary creep fracture (weld bead to weld bead) and the Type IIIa weld interface creep fracture in dissimilar welds (parent metal to weld metal), such as carbon depletion, carbide depletion, low hardness and recrystallisation. In P91 weld metal (Zhang et al., 2007), this type of creep fracture acted as a linkage between the typical weld creep fractures in columnar regions, making a significant contribution to the creep failure of the welds. In P92 weld metal (Allen et al., 2005), this type of creep fracture was the dominant creep fracture mechanism leading to the final failure of the materials (Figure 2.26). However, the mechanism of the formation of inter-bead boundary fractures has not been extensively studied.

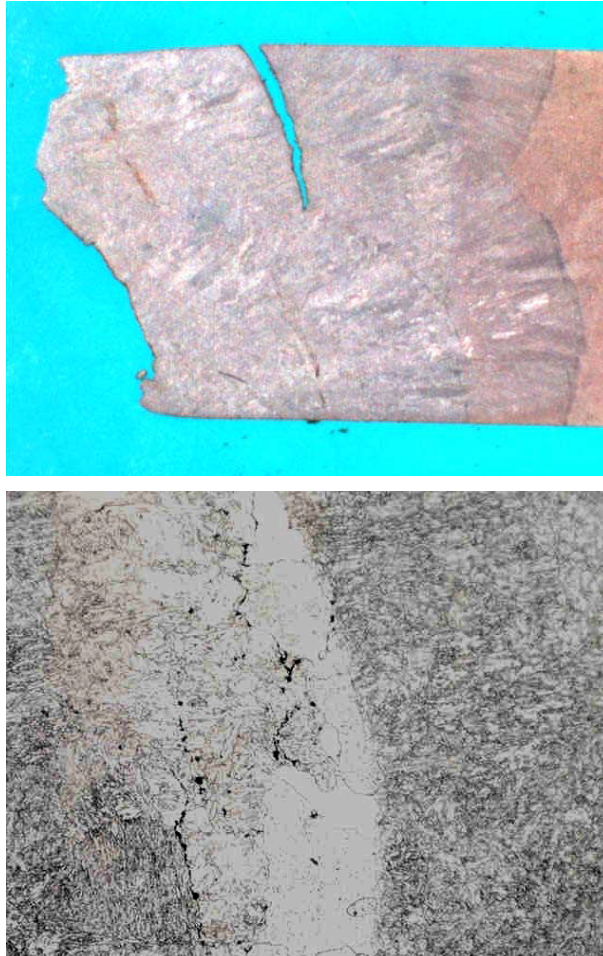


Figure 2.26 Weld metal failure and inter-bead microcracking and cavitation in carbon-depleted regions at the bead boundaries (Alstom HCM12A casting weld, P92 weld metal, 625°C 105 MPa.) (Allen et al., 2005)

2.4.4 Mechanism of carbon diffusion in dissimilar welds

Diffusion driven by an activity gradient was first reported in Darken's experiment (Stark, 1980) and has been reported frequently in the examination of carbon diffusion in welds between dissimilar steels. The presence of higher chromium leads to a significant reduction in the activity of carbon, and thus carbon migration down the activity gradient towards the high chromium side has been observed during high temperature exposure of dissimilar welds. This has resulted in a carbon-depleted zone on the low chromium side and carbon-rich zone on the high chromium side (Laha et al., 2001b; Foret et al., 2006; Laha et al., 2001a; Kasatkin and Tsaryuk, 1967; Foret et al., 2001). A thermodynamic and kinetic model of carbon diffusion in dissimilar welds has also been created by some researchers

based on the Darken's experiment (Foret et al., 2001; Million et al., 1995; Kucera et al., 1985; Buchmayr et al., 1990; Sopousek et al., 2004; Kozeschnik et al., 2002). As shown in Figure 2.27, carbon redistribution is expected to occur at the interface of the dissimilar weld between steels with different chromium concentrations. In Foret et al. (2001) and Million et al. (1995)'s modelling work, constant carbon concentrations at the interface ($N_C^-(0)$ on the low chromium side and $N_C^+(0)$ on the high chromium side respectively) will be achieved when $t > 0$.

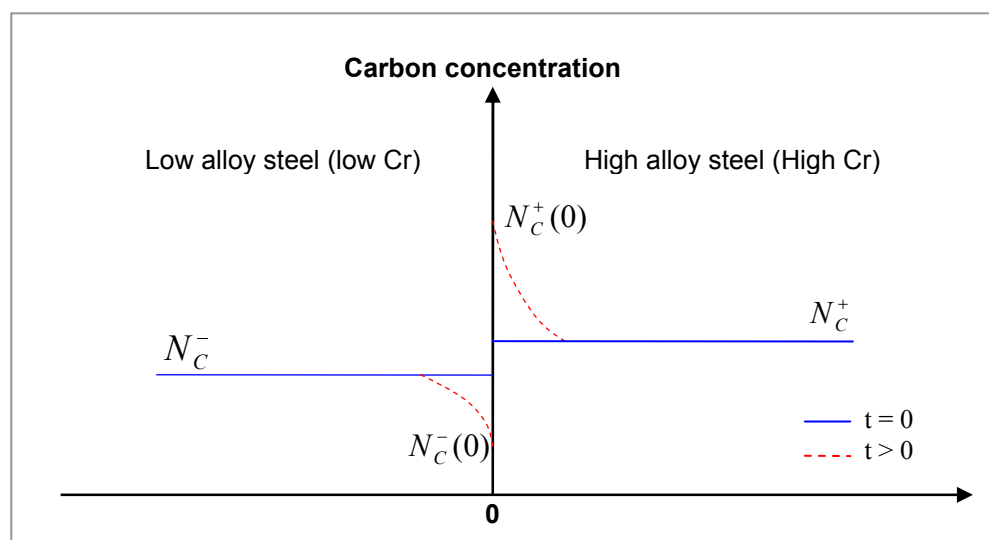


Figure 2.27 Schematic diagram showing the modelling of carbon diffusion in dissimilar welds

According to Henry's law, the activity of carbon a_C is given by,

$$a_C = N_C \gamma_C \quad [2.15]$$

where, N_C is the carbon concentration in atomic fraction; γ_C , the activity coefficient of carbon, is independent of carbon content. γ_C can be expressed by Wagner's relationship (Pilous and Stransky, 1998),

$$\gamma_C = \exp(\varepsilon_C^{Cr} N_{Cr}) \quad [2.16]$$

γ_C does not depend on carbon concentration but it is only a function of the concentration of substitutional element, which, in this case, is the chromium equivalent. ε_C^{Cr} is the Cr-C thermodynamic interaction coefficient, to which, the following expression applies (Million et al., 1995),

$$\varepsilon_C^{Cr} = 54.98 - 78600/T \quad (\text{at. fraction}^{-1}) \quad [2.17]$$

The thermodynamic chromium equivalent in the atom fraction is determined from the equation (Pilous and Stransky, 1998),

$$N_{Cr(eq)} = \sum K_{Cr(C)}^j N_j \quad [2.18]$$

The summation sign in this equation relates to all substitutional elements in the steel. N_j is the concentration of element j in the steel in the atom fraction. $K_{Cr(C)}^j$, the equivalence constant, is the ratio of the interaction coefficient of element j and chromium. It can be expressed by the equation,

$$K_{Cr(C)}^j = -1869 \ln\left(\frac{v_C^j}{6}\right) \cdot \exp\left(-0.6835 \ln\left(\frac{v_C^j}{6}\right)\right) \quad [2.19]$$

where, v_C^j are the characteristic numbers. $K_{Cr(C)}^j$ and v_C^j can be obtained by Table 2.5 and 2.6 as below.

Characteristic number v_C^j	Period						
	1	2	3	4	5	6	7
1				Sc	Y	La*)	Ac**
2				Ti	Zr	Hf	Ku
3				V	Nb	Ta	
4		(O)		Cr	Mo	W	
5		F	Cl	Mn Br	Tc J	Re At	
6	He	Ne	Ar	Fe Kr	Ru Xe	Os Ru	
7	H	(Li)	Na	K Co	Rb Rh	Cs Ir	Fr
8		(Be)	Mg	Ca Ni	Sr(Pd) Cd	Ba Pt	Ra
9		B	Al	Cu	Ag	Au	
10		C	Si	Zn	Cd	Hg	
11		N	P	Ga	In	Tl	
12		(O)	S	Ge	Sn	Pb	
13				As	Sb	Bi	
14				Se	Te	Po	

*) Lanthanides, **) actinides, () position of the elements in the brackets is not certain. Statistical processing of experimental data shows that $v_C^j = v_i^j$, where $i = N, H, B$.

Table 2.5 Characteristic numbers v_C^j for individual elements on the periodic system of elements (Pilous and Stransky, 1998)

Characteristic number v_C^j	1	2	3	4	5	6	7	8	9	10	11	12	13	14
Equivalence constant $K_{Gr(C)}^j$	11.40	4.35	2.08	1.00	0.386	0	-0.259	-0.442	-0.574	-0.673	-0.749	-0.807	-0.852	-0.887

Table 2.6 Dependence of the equivalence constants $K_{Gr(C)}^j$ on characteristic numbers v_C^j elements in the periodic table of elements (Pilous and Stransky, 1998)

It is necessary to note that the application of the stationary model involves the presumptions that carbon diffusing in the steel matrix is a part of carbon which appears in solid solution, and that the dissolution of carbides continuously compensates the carbon decrease in solid solution caused by diffusion outflow (Million et al., 1995). It was also argued (Foret et al., 2001) that carbon

redistribution in the creep resistant steels is, apart from difference in the activity of carbon on both sides of the weld joints, governed also by kinetic dissolution or precipitation of carbides phases.

2.4.5 Thermodynamic modelling of carbon diffusion in dissimilar welds

Thermodynamic modelling of carbon diffusion in dissimilar welds has been carried out by many researchers (Sopousek et al., 2004; Sopousek and Foret, 2008; Kozeschnik et al., 2002). The CALPHAD approach by calculation of the phase diagram was commonly used in such a simulation. This semi-empirical approach enables the calculation of chemical compositions of equilibrium phases as well as the chemical potentials / activities of elements at a given condition (composition, temperature and pressure). This approach is based on a description of the individual phases by thermodynamic models using thermodynamic parameters which can be provided by an appropriate database (Sopousek and Foret, 2008). Most of the simulation work is based on the assumption that diffusion is the controlling process of the phase transformation rate, theory of multi-component bulk diffusion, thermodynamic evaluation of the driving force for phase transformation, and the assumption of local condition of phase equilibrium (Sopousek et al., 2004). Thermo-Calc software is a commonly used simulation tool based on the CALPHAD approach; and DICTRA software is also commonly used in the prediction of the sequence of phase transitions across the dissimilar weld joints.

As in Figure 2.28, the results of simulation of carbon diffusion and phase fraction at a P22 / P91 weld joint (Sopousek and Foret, 2008) showed the existence of a carbon depleted zone on the P22 (low alloy side) side and a carbon enriched zone on the P91 side (high alloy side), and the corresponding distribution of carbides ($M_{23}C_6$, M_7C_3 , M_6C). The good correlation between simulation results and experimental results indicated that such kinetic simulation can be used for failure-risk prediction for the weld joints.

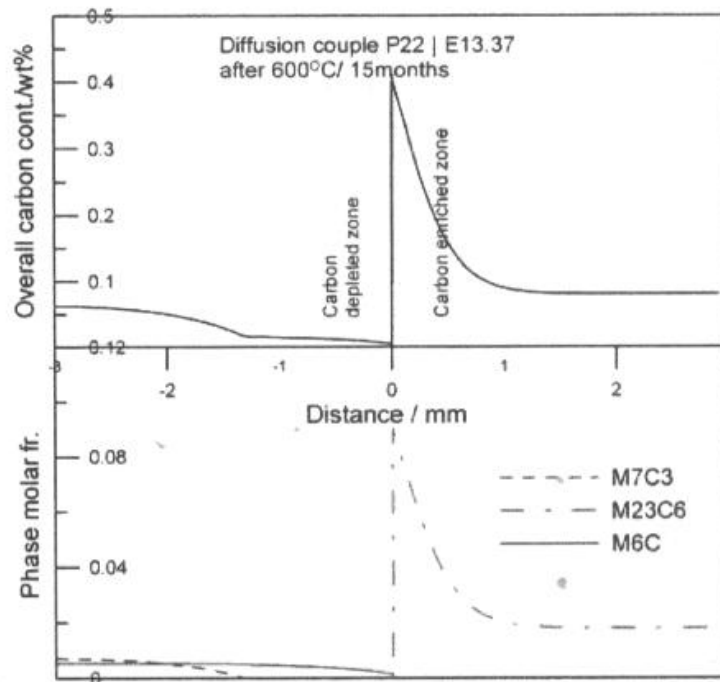


Figure 2.28 P22 (left side) / P91 (right side) weld joint simulation (Sopousek and Foret, 2008)

2.5 SUMMARY

The creep failure associated with welds has been regarded as a critical issue in the studies of power plant steels. As such, based on the literature survey of creep resistant chromium steels and welds, and their creep properties, this work has been focused on the investigation of the P91 weld metal itself in the aspect of both microstructure and properties, seeking ways to further understand the evolution of the microstructure and mechanism of creep failures. Moreover, thermodynamic modelling work has been carried out for the simulation of formation of localised creep-weak regions (white-band regions) based on the understanding the carbon migration in dissimilar welds during creep exposure.

Chapter 3

Experimental work

3.1 MATERIALS AND WELD PREPARATION

In this section, the preparation of the SUPERGEN P91 MMA weld pad is introduced. A P91 TIG weld produced by the melting and solidification of P91 parent metal was also prepared to aid the understanding of the formation of the microstructure and creep-weak zones found in the SUPERGEN P91 weld metal.

3.1.1 SUPERGEN P91 MMA weld pad

In order to understand the properties of P91 weld metal itself in isolation from the weldment structure (containing the parent metal (PM) and heat-affected zone (HAZ)), three large P91 multi-pass weldpads (A, B and C) were produced by Doosan Babcock Ltd. UK, using their $\Phi 5\text{mm}$ Type M creep resistance electrodes (BS EN 1599-E CrMo 91 B32 H5). These are modified 9CrMo basic coated low hydrogen electrodes for high temperature creep applications, with a mild steel core rod coated by a flux containing the necessary alloying elements. The welding was performed by the manual metal arc welding (MMAW) procedure, with the laying down of a large number of overlapping welding passes on a steel plate, as shown in Figure 3.1a and 3.1b. The welding was in one direction only, with adjacent bead overlap being around 50%. The preheat temperature was approximately 200°C to 250°C, and this was maintained throughout the welding process. A post weld heat treatment (PWHT) was performed after welding: the weldpad was heated to 760°C at 100°C/h, soaked for 3 hours and then cooled at about 46°C/h.

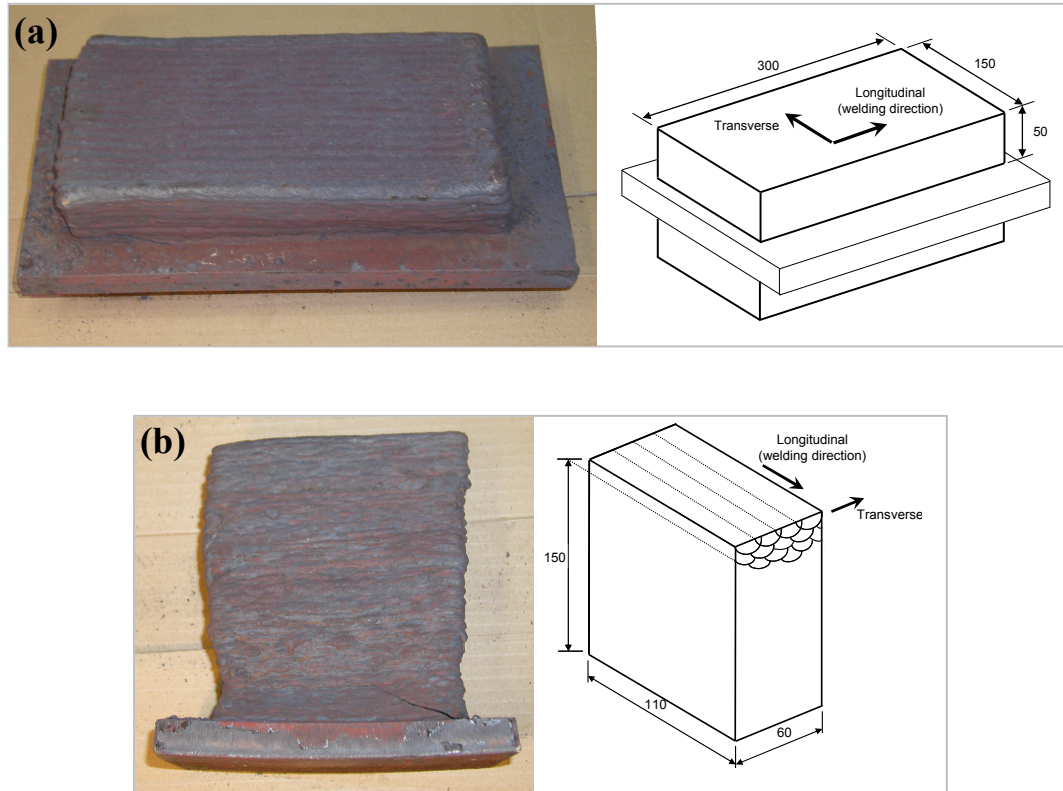


Figure 3.1 Photographs and schematic diagrams of (a) P91 weldpad B (b) P91 weldpad C following post-weld heat-treatment (mm)

In order to investigate the anisotropic creep behaviour of P91 weld metal, creep specimens were removed from the P91 weld pads from different orientations. Taking the angle between welding direction and specimen axis as φ (Figure 3.2), creep specimens were cut from both longitudinal direction ($\varphi = 0^\circ$) and transverse direction ($\varphi = 90^\circ$). The creep tests were performed at 650°C in air under various stress levels (115 MPa, 90 MPa, 80 MPa), with both longitudinal and transverse specimens tested at each stress level. The chemical composition of the SUPERGEN P91 weld metal was provided by Doosan Babcock Ltd. UK along with the weld metal, as listed in Table 3.1. It was measured on a sample removed from the weld pad using optical emission spectrometry along with LECO analysis.

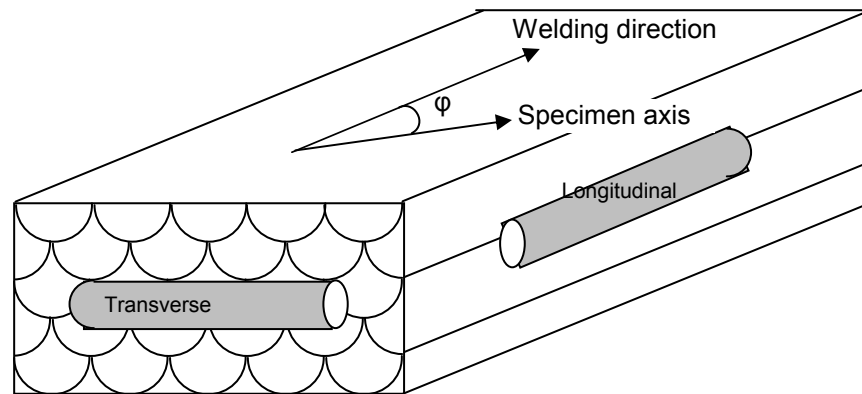


Figure 3.2 Schematic illustration of creep specimen orientations

C	Si	Mn	P	S	Cr	Mo	Ni
0.098	0.45	1.11	0.015	0.010	8.61	1.02	0.22
Al	Co	Cu	N	Nb	V	O	
<0.01	<0.02	0.05	0.046	0.03	0.21	0.059	

Table 3.1 Chemical composition of SUPERGEN Type M P91 weld metal (wt%)

3.1.2 P91 TIG weld

P91 TIG welds were made by the simple melting and solidification of a plate of P91 parent metal without any addition of filler materials. The TIG welding was carried out at 100 amps and a welding speed of 0.08 m/min (about 1.33 mm/s) and 0.04 m/min (about 0.67 mm/s). The welding process was carried out with argon protection, where the flow rate of argon for torch shielding was 14 l/min in all cases. As shown in Fig. 3.3, both a single pass weld and a multi-pass weld containing two overlapping passes were made on 8 mm thick P91 plate. The overlapping in the multipass weld is approximately 50%. The chemical composition of the P91 TIG weld measured by the atomic emission spectrometry (Foundry-Master) is given in Table 3.2. Samples were removed from each plate for further examination and heat treatment. Heat treatment was carried out in air at 650°C and 760 °C for 30 hours.

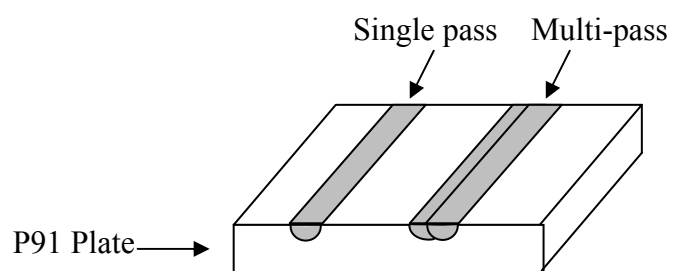


Figure 3.3 Schematic illustration of P91 TIG weld

C	Si	Mn	P	Cr	Mo	Ni	Al	Co	Cu	Nb	V
0.127	0.33	0.43	0.008	8.48	0.97	0.09	0.003	0.013	0.034	0.051	0.25

Table 3.2 The chemical composition of P91 TIG weld (wt %)

3.2 CREEP TESTS OF SUPERGEN P91 WELD METAL

Creep tests were carried out on P91 weld metal samples. The geometry of the creep specimens is shown in Figure 3.4. Creep tests were performed in a temperature-controlled laboratory, using five ton Dension (T45A3) constant load creep test machines. Creep specimens were tested in air and a temperature of 650°C was maintained throughout all tests. Specimen temperature was monitored by thermocouples attached to the specimens. The strain was measured by monitoring the changes in the specimen gauge length at regular time interval until specimens failed. The creep strain curves were obtained, and the corresponding minimum creep strain rates (MSR), and rupture lives (t_f) were also recorded.

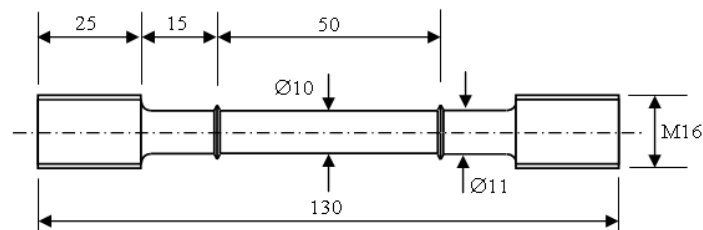


Figure 3.4 Schematic diagram showing the creep specimen geometry (mm)

3.3 CHARACTERISATION METHODS

3.3.1 Sample preparation

The fracture surface of the creep tested specimens following failure were often oxidised and could not be realistically examined in a scanning electron microscope (SEM). To overcome this, fracture surfaces were de-scaled in a 4wt% aqueous solution of 1 part malic acid ($C_4H_6O_5$) to 3 parts ammonium citrate at 80°C for two hours to remove oxide.

All creep tested specimens were also sectioned though the specimens parallel to the stress axis. The P91 TIG weld plate was sectioned along the plane normal to the welding direction to examine the cross-section. All sectioned samples were mounted using cold mounting in epoxy resin for large specimens or hot mounting with conductive phenolic mounting resin black for smaller specimens. Cross-sections of the samples were ground and polished with SiC and diamond abrasives down to a 1 μm finish. The microstructural features were revealed by etching with acidic ferric chloride.

3.3.2 Optical microscopy (OM)

Optical microscopy (OM) was utilised for the examination of the microstructure features and creep fractures of the P91 weld metal. In order to obtain the macro information of the weld structure distribution and creep fracture features, microstructural montages were generated using Adobe Photoshop. For each sample, large numbers of low magnification OM images (x5) were taken covering the whole examination area, and then stitched using Adobe Photoshop to show the macro structure.

3.3.3 Micro-hardness measurement

The Vickers micro-hardness of the specimens was measured using a Leco M-400 tester. An indentation time of 15 seconds was employed. The hardness values

were obtained by measuring the length of diagonals of the hardness indents and converting to Vickers Hardness readings. The conversion equation is shown as follows.

$$H_V = \frac{2F \sin \frac{\theta}{2}}{d^2} \approx \frac{1.854F}{d^2}, \quad [3.1]$$

where F is the load in kgf, $\theta = 136^\circ$, d is arithmetic mean of the two diagonals of the hardness indents in mm. H_V is the Vickers hardness in kgf/mm². A 0.5 kgf load was used for the hardness measurement across the different microstructure regions of the weld metal. For creep tested specimens, hardness tests were performed on axial cross sections, along a line from fracture surface to grip end, with 500 μ m between adjacent indentations. A lower indentation load (such as 50 gf) was used in some cases (such as tests in the white-band regions) as stated.

3.3.4 Strain measurement and analysis

In order to investigate the relationship between the evolution of hardness and strain due to creep, the reduction in area (R_A) was also measured along the creep samples following creep failure. R_A is the difference between the original cross sectional area of specimen gauge (A_0) and the local area of cross section after creep testing (A):

$$R_A = \frac{A_0 - A}{A_0} \%, \quad [3.2]$$

Average diameters of creep tested specimens were measured every 0.5mm along the stress axis from the gauge end to fracture surface, using a Mitutoyo EuroApex CNC coordinate measuring machine (CMM). As shown in Figure 3.5, the longer half of each creep-tested specimen was used for the measurement. Since the radius of the detecting ball in CMM is 2.5 mm, the measurement started 3 mm from the gauge end and finished at the position just before the fracture surface. At each position, measurements were taken at twelve evenly spread points, as

indicated in Figure 3.5, to obtain the average diameter. The original diameter of creep specimens within the gauge is 10 mm.

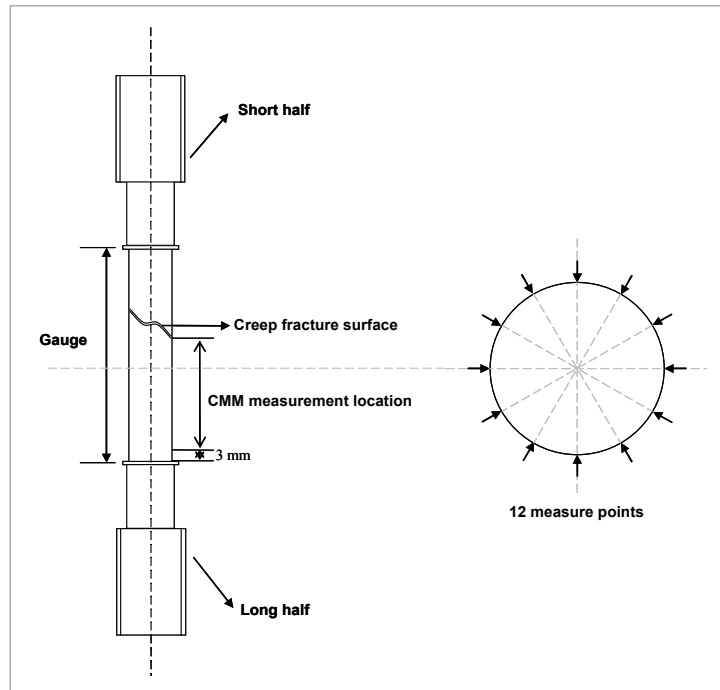


Figure 3.5 Schematic diagram of CMM measurement

3.3.5 Scanning electron microscopy (SEM)

The scanning electron microscope (SEM) is a microscope which uses electrons instead of light for imaging. The sample surface was scanned with a high-energy electron beam. The electrons interact with sample atoms to produce the signals that contain information about the sample surface. The signals include secondary electrons (SE), which can provide information concerning the topography and surface structure of the sample, and back scattered electrons (BSE), which can provide the information about the distribution of different elements in the sample. Characteristic x-rays were also used to identify and quantify the composition of the sample, using the energy dispersive x-ray (EDX) analysis method. A Philips/FEI XL-30 scanning electron microscope was used in this work.

Since the specimens for SEM examination are required to be electrically conductive, most samples were hot mounted in conductive phenolic mounting

resin. In the case of large samples, cold mounting in epoxy resin was used. To prevent electrical charging in the SEM, these samples were coated with gold or platinum with an Emscope SC-500 Sputter Coater. The bottom and side of the mounted samples were also covered with aluminium foil to provide better conductivity.

All samples were examined using 20 kV accelerating voltage, and the working distance was set to be 10 mm. For EDX analysis, the counting time employed was 200 seconds, which gave more reproducible results, especially for minor alloying elements. In order to quantify the amounts of the precipitates ($M_{23}C_6$ carbides) in different regions of weld metal, secondary electron images on selected areas of lightly etched samples were taken at a constant magnification of $\times 1000$. The analysis of these images was carried out using the particle counting module in Image J software (National Institutes for Health, Maryland, USA). The contrast between the precipitates and the matrix is obvious in these black and white secondary electron images. A threshold range can be set to differentiate the particles and the matrix. Information regarding the size, numbers and volume fraction of particles can be obtained from the analysis. However, the limit of particle analysis using Image J need to be noticed, since factors such as sample etching, SEM imaging and threshold setting in analysis will inevitably affect the results of particle analysis.

3.3.6 Laser induced breakdown spectroscopy (LIBS)

It was recognised that the ability of EDX analysis to accurately quantify the differences in carbon levels in materials where the bulk carbon level is less than 0.1 wt% is limited. In light of these limitations, laser-induced breakdown spectroscopy (LIBS) was employed, using a LIBS prototype instrument designed for rapid elemental mapping with micro-scale spatial resolution. The prototype instrument was manufactured by the Fraunhofer ILT (Aachen, Germany) and the application development is being conducted at the Corus Swinden Technology Centre (Rotherham, UK). LIBS is a spectroscopic technique that enables rapid and direct chemical analysis of any sample types (conductive and non-conductive solids, liquids and gases). During a LIBS measurement, a high energy density pulsed laser beam is focused on to the sample, which leads to the ablation and

excitation of a small volume of the sample; the elements in the excited vapour are then analysed by optical emission spectroscopy (OES). The current micro-analysis LIBS instrument is designed to generate elemental maps for 31 elements simultaneously. The emission signals are recorded by a stack of photomultiplier tube detectors with the limits of detection being similar to those experienced with conventional spark-OES. The samples were polished down to a 1 μm finish and lightly etched in order to identify the location of the areas of particular interest displaying white-bands. The LIBS analysis can be very efficient. For examples, a rectangular array of analyses was carried out on a 12 \times 5 mm area of the P91 weld metal covering several weld beads, with a step size of 20 μm in both the X and Y directions. This scan examined the composition at 150851 individual analysis points, the data for which were gathered in \sim 10 minutes.

3.3.7 Electron backscatter diffraction (EBSD)

Electron backscatter diffraction (EBSD) is a microstructural-crystallographic technique, which allows crystallographic information to be obtained in the scanning electron microscope (SEM) fitted with a backscatter diffraction camera. When the electron beam impinges on a tilted crystalline sample, the diffracted electrons form a characteristic diffraction pattern on a fluorescent screen, which can be analysed to provide information such as grain morphology, crystal orientation and grain boundary misorientations.

In this work, EBSD analysis was used to investigate the grain structure of creep-weak zones in the form of white bands discovered in creep tested P91 weld metal. The testing was done in Loughborough University using an EDAX Pegasus combined EBSD and EDX system attached to a LEO 1530-VP FEGSEM.

Extra care should be given to the sample preparation for EBSD examination. Since diffraction electrons escape from only a few tens of nanometres from the sample surface, it is essential to remove all mechanical distortion which is produced during previous grinding and polishing. In this case, the samples were firstly ground and polished with SiC paper and diamond abrasives down to a 1 μm finish. Samples were chemically etched at this stage to locate the testing region previously marked by hardness indents. An additional final polishing stage using

colloidal silica was then carried out to remove the residual surface damage from the previous diamond polishing. Colloidal silica polishing is basically a chemo-mechanical polish, combining the effect of mechanical polishing with etching. This final polishing took approximately 30 min to achieve the desired surface finish without causing excessive relief. The EBSD examination operated with a 20kV accelerating voltage and an aperture size of 30 μm . The sample was tilted at 70° with respect to the horizontal during the test.

3.3.8 Transmission electron microscopy (TEM)

Unlike SEM which uses secondary and backscattered electrons, transmission electron microscopy (TEM) is a diffraction technique which uses electrons which pass through a very thin slice of the sample. This technique for material characterisation is able to provide versatile information, such as the imaging of local structure at extremely high magnification, identifying the species and their crystal class and analysing the local chemical composition. In this work, examination was performed with a JEOL 2000FX TEM operating at 200 kV.

3.3.8.1. Sample preparation

a. Standard thin foils of bulk weld metal

The TEM specimen must be extremely thin for the electrons to pass through it and create an image or diffraction pattern. To achieve this, a thin slice of approximately 2 mm thick was cut off from the P91 creep tested specimen and secured in a polishing block for grinding down to 100 μm thick on various grades of SiC paper. After that, several 3 mm diameter discs were punched from this thin foil, and glued onto 3 mm diameter copper sample holders. These samples were firstly mechanically polished down to a thickness of about 40 μm using a Southbay 590 tripod polisher with diamond pastes of 30, 15, 9, 5, 3, 1 and 0.5 μm , and then ion-beam milled using a FISCHIONE 1010 argon low angle milling and polishing system at 6 kV, to produced a thin area typically ~100 nm thick required for imaging around the central hole of the sample.

b. Focus ion beam (FIB) milled sample of white band region

In this work, thin regions (termed white-bands) were identified. Since the white-band regions were typically about 200 μm wide, the standard TEM sample preparation technique could not be used to reproducibly produce foils from these regions. As such, focused ion beam (FIB) machining with FEI quanta 2003D FIBSEM was used for the sample preparation of the white-band region. FIB uses a focused beam of gallium ions, which sputter atoms from the surface when they strike the sample. Because of the sputtering capability, the FIB is commonly used to prepare TEM samples of specific area of interest, which in this case, allowed sample extraction from the white-band region. FIB was used to cut two trenches, one from each side, leaving behind a thin electron-transparent lamella supported by bulk material on two opposite sides. The sample was lifted out by a nanomanipulator mounted inside the FIB chamber and then mounted on a TEM grid for examination. The size of the FIB sample of the white-band region is about $4 \times 10 \mu\text{m}$ and 250 nm thick. Since it was still slightly thick for the TEM imaging, an extra thinning process for 25 minutes using a FISCHIONE 1010 argon low angle milling and polishing system at 4 kV was applied.

3.3.8.2. TEM imaging and EDX

TEM imaging allows the detailed investigation of the samples at much higher magnification; it is very useful for the determination of crystallographic information and for examination of small phases such as precipitates. Both bright field and dark field images were obtained from creep-tested P91 weld metal and the FIB milled white-band sample. Another advantage of TEM is that it can determine the chemical composition in a region smaller than a few nanometres using energy dispersive X-ray (EDX) spectroscopy fitted within TEM. It has been used to aid identification of the precipitates on the samples.

3.3.8.3. Selected area electron diffraction patterns (SADP)

Selected area electron diffraction (SAD) is a crystallographic experimental technique which can be performed inside the TEM. It is a useful method for the identification of precipitates. The principle of electron diffraction is similar to that of

x-ray diffraction, but the wavelength of electrons in the TEM is much smaller than that of x-rays. Like x-ray diffraction, electron diffraction obeys Bragg's law,

$$\lambda = 2d \sin \theta , \quad [3.3]$$

where λ is the wavelength of the electrons, d is the spacing between crystal planes and θ is the angle of the diffracted electron beam. The wavelength of the electron in TEM can be given by the de Broglie equation,

$$\lambda = \frac{h}{p} , \quad [3.4]$$

where h is Planck's constant and p is the momentum of the electron. In the TEM, the relationship between camera length L and the distance r between diffraction spots and the transmission beam spot can be express as,

$$\frac{r}{L} = \tan 2\theta , \quad [3.5]$$

Since diffraction angle θ of electron beam is very small, $\tan 2\theta \approx 2\theta$ and $\sin \theta \approx \theta$. The above equations can be rearranged as,

$$\frac{r}{L} = 2\theta , \text{ and } \lambda = 2d\theta , \quad [3.6]$$

So, the d spacing between crystal planes can then be expressed as,

$$d = \frac{L\lambda}{r}$$

In this work, the accelerating voltage of the electrons is 200 kV, the wavelength of the electrons λ is 0.0251Å and camera length L is 1000 mm. So the camera constant $L\lambda = 25.1 \text{ mm \AA}$.

The measurement of the angles and distance between diffraction spots was performed using software Image J. d spacings of the crystal can then be

determined and matched with the database of known crystal parameters. The precipitates can finally be indentified.

3.4 MODELLING METHOD

Thermodynamic modelling of the phases expected in the steels as a function of composition and temperature was carried out using Thermo-Calc[®] 4 for Windows with TCFE5 Steel and Fe-alloys Database (Foundation of Computational Thermodynamics and Thermo-Calc Software AB, Stockholm, Sweden). Thermo-Calc for Windows is a software package used to perform thermodynamic and phase diagram calculations for multi-component systems in materials science and engineering. Calculations are based on thermodynamic databases produced by expert evaluation of experimental data using the CALPHAD method. The CALPHAD method is based on the fact that a phase diagram is a manifestation of the equilibrium thermodynamic properties of the system, which are the sum of the properties of the individual phases. It is thus possible to calculate a phase diagram by first assessing the thermodynamic properties of all the phases in a system.

TCFE5 is the steel and Fe-alloy database for Thermo-Calc Classic and/or Thermo-Calc for Windows. It can be applied in steel and Fe-alloy design and engineering. The TCFE5 database includes data for molar volume calculation of density and lattice parameter (for cubic structures), coefficient of thermal expansion and/or relative length change.

Thermo-Calc can be used for all kinds of calculations of thermodynamic properties, equilibrium and partial / local-equilibrium quantities, chemical driving forces, and for various types of stable / meta-stable phase diagram and property diagrams of multicomponent systems. In this work, it has been used to calculate the phase diagram of P91 weld metal and the equilibrium at given conditions (chemical composition, temperature and pressure etc.). Thermo-Calc deals with the systems that are in equilibrium, i.e., in a state stable against internal fluctuations in a number of variables, such as temperature and composition. If the work that can be exchanged with the surroundings is limited to pressure-volume work, the state of equilibrium of a system can be obtained by assigning values to exactly $N+2$ state variables where N is the number of component of the system.

The modelling started with defining the system, which in this work, is defining the elements contained in the steel with TCFE5 steel and Fe-alloy database as

chosen database. The phases which will be considered in the calculation can be selected from the full list of possible phases. The concentration of each element is defined under a defined temperature and pressure to obtain the equilibrium. To investigate the solute partition during solidification (especially the chromium partition), the fraction of phases existing was plotted against the temperature from room temperature to above the melting point, and the element composition of first solidified phase was obtained. Since carbon diffusion caused by localised solute partition is considered to be the second stage of the white-band formation, carbon activity under different conditions has also been investigated. The details of modelling work will be presented in chapter 5 along with the modelling results.

Chapter 4

Experimental Results

4.1 CHARACTERISATION OF P91 WELD METAL

4.1.1 Type M P91 weld rod

Figure 4.1a shows a cross-section of Type M P91 welding consumables used for the deposition of the P91 weldpad, with the core wire surrounded by the flux. The EDX analysis indicates that the core wire is mild steel with 0.4 wt% Mn and 0.1 wt% Cr; the main alloying elements are present in the flux. Figure 4.1(b) shows an SEM image of a polished section of the flux with the metallic particles containing the alloying elements being in the form of particles typically 200µm in size. The chemical composition of a number of individual particles (as marked in Figure 4.1b) have been analysed by EDX analysis and the results are shown in Table 4.1. This shows that the major metallic additions are typically in the form of ferro-alloys (ferro-vanadium, ferro-chromium etc) with other particles containing the minor elemental additions required in the Grade 91 alloy along with other species required for the operation of the flux.

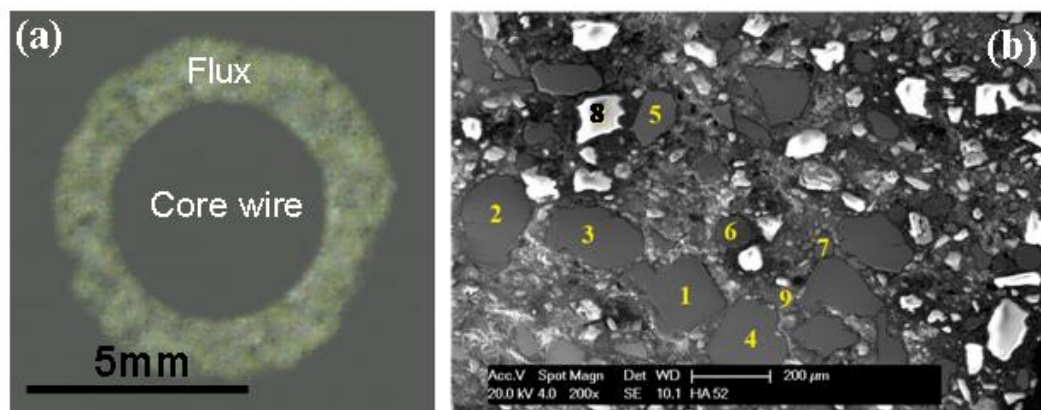


Figure 4.1 (a) Structure of Type M weld rod; (b) SEM image of the flux coating

Position		Elemen	Average / wt%	
Flux coating	1	Fe	40.2	
		V	59.8	
	2, 3, 4	Fe	32.1	
		Cr	67.9	
	5	Fe	27.4	
		Mo	72.6	
	6	Fe	54.6	
		Si	45.4	
	7	Fe	15.9	
		Mo	83.2	
		Ca	0.3	
	8	Si	0.6	
		O	56.8	
	9	Si	43.2	
		Ti	98.6	
		V	1.0	
			Ca	0.4

Table 4.1 Element distribution in type M P91 welding rod

4.1.2 Microstructure features

Figure 4.2 shows montage images of the microstructural distribution in P91 weld metal in the as-PWHT condition, both from a longitudinal section and from a transverse section. The microstructure of the P91 PWHT weld metal consisted of two main microstructural regions, namely a coarse columnar grain region and a refined (recrystallised) equi-axed region. The coarse columnar grain region was formed by the solidification of liquid metal in the weld pool, whilst the refined equi-axed region was formed by the recrystallisation of such columnar material during the reheating process associated with the deposition of the next bead onto a previously deposited bead. The spatial distribution of these two regions differs between longitudinal samples and transverse samples, as shown in Figure 4.2. Alongside each micrograph is a schematic diagram of the distribution of the microstructural regions. Longitudinal samples exhibited a banded structure of coarse columnar regions and refined regions whereas transverse samples had a structure of overlapping weld beads. The samples in Figure 4.2 were removed from the P91 weld pad. Figure 4.3 shows the scanned microstructural image of a multipass P91 weld metal removed from a pipe weld in the as-PWHT condition showing a transverse section.

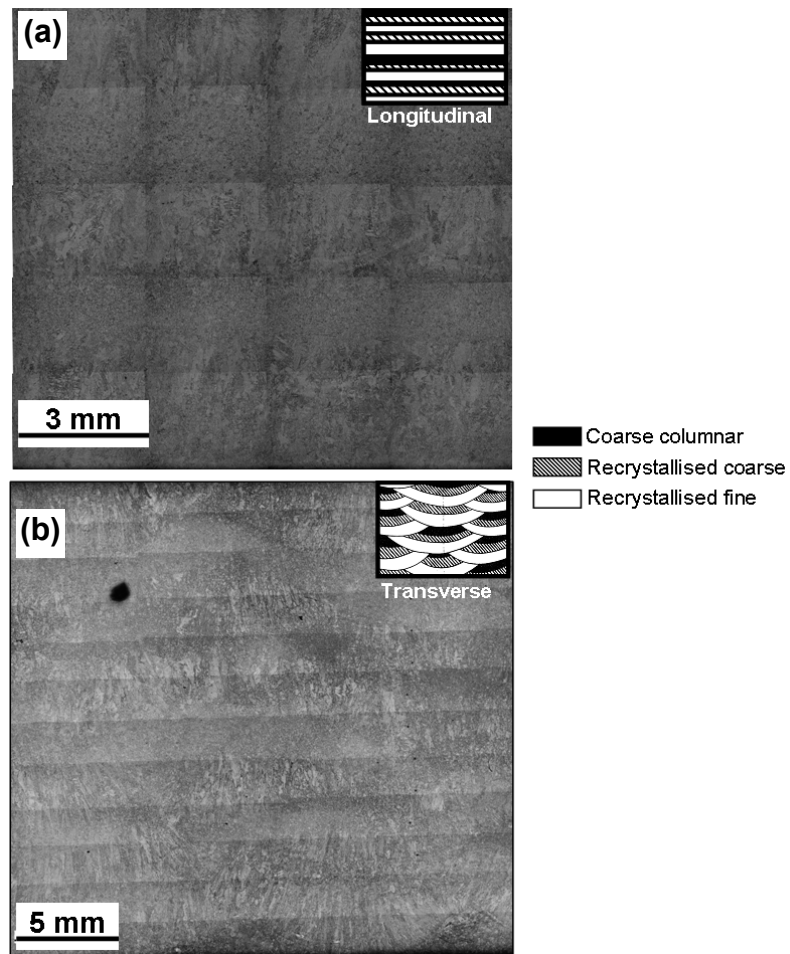


Figure 4.2 Optical micrograph montages of (a) longitudinal and (b) transverse sections of PWHT P91 weld metal with a schematic diagram of the microstructural distribution in each case (sample etched with acidic ferric chloride)

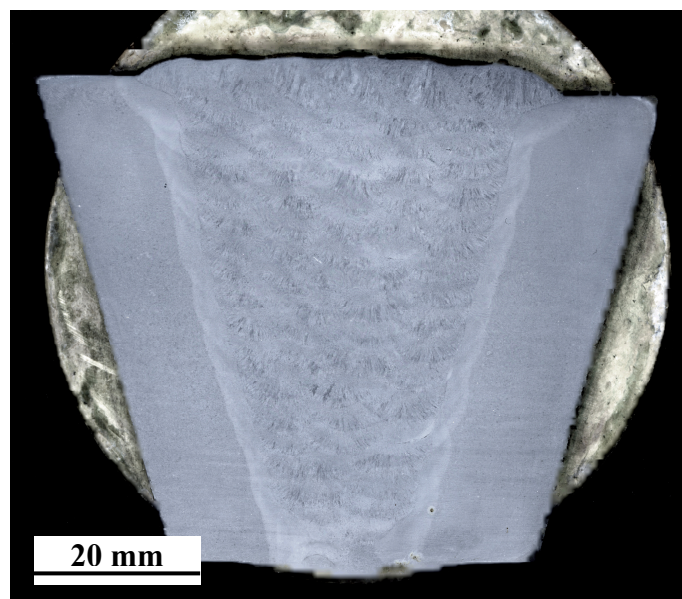


Figure 4.3 Scanned microstructural image of transverse section of P91 pipe weld

4.1.3 Hardness

A microhardness profile across both columnar and refined regions on a transverse section of P91 weld metal in the as-PWHT condition is shown in Figure 4.4. It can be seen that columnar region exhibits a much higher hardness than the refined region. The hardness values in the columnar regions range from 260 to 285 kgf mm^{-2} , whilst the hardness values in the refined regions range from 230 to 260 kgf mm^{-2} .

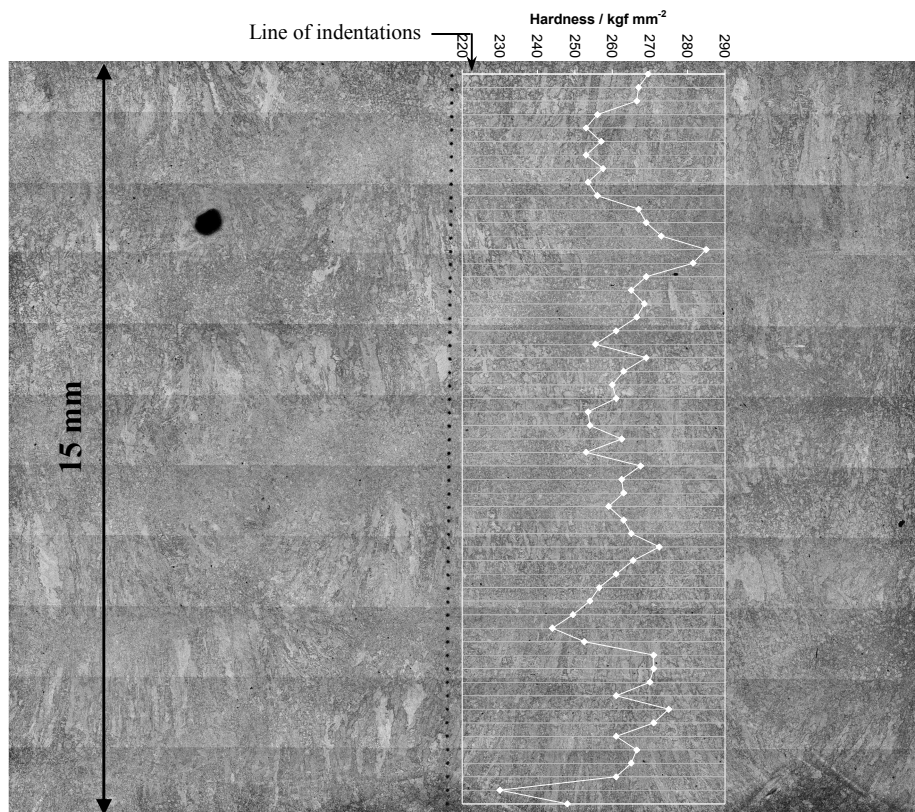


Figure 4.4 Distribution of Vickers hardness on the transverse P91 weld metal

4.2 CHARACTERISATION OF CREEP TESTED P91 WELD METAL

4.2.1 Anisotropic creep behaviour

In order to investigate the anisotropic creep behaviour of P91 weld metal, creep specimens were removed from the P91 weld pad on both longitudinal ($\varphi = 0^\circ$) and transverse sections ($\varphi = 90^\circ$), where φ is the angle between the welding direction and the sample axis as indicated in Figure 3.2. Creep tests were carried out at 650°C under various stress levels (115 MPa, 90 MPa and 80 MPa), with both longitudinal and transverse specimens tested at each stress level. The creep strain curves obtained from the tests are shown in Figure 4.5, and the corresponding rupture lives (t_f) and strain to failure (ϵ_f), are given in Table 4.2. (These samples are labelled Fxx-yy where xx = the angle φ , and yy indicates the applied stress).

It is clear to see that specimens creep tested at lower stress levels always exhibited longer creep lives in both longitudinal and transverse specimens. In addition, at each stress level, the longitudinal specimens exhibited much longer creep failure lives than the transverse specimens, and the failure ductility in the longitudinal direction was about twice of that in the transverse direction.

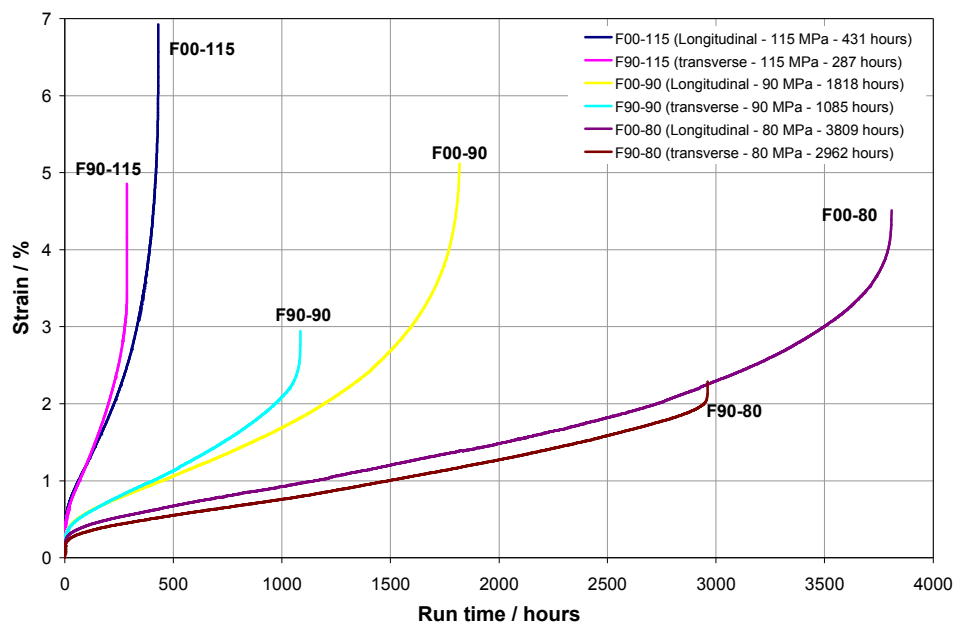


Figure 4.5 Creep strain curves of the Type M P91 weld metal at 650°C .

Spec. ID	σ (MPa)	ϕ (deg.)	t_f (h)	ϵ_f (%)
F00-115	115	0	431	~ 6.9
F90-115	115	90	287	~ 3.8
F00-90	90	0	3809	~5.1
F90-90	90	90	2962	~2.9
F00-80	80	0	1818	~4.5
F90-80	80	90	1085	~2.3

Table 4.2 Creep Data (rupture lives t_f and strain to failure ϵ_f) for the P91 weld metal creep tested at 650°C and various stress levels for both longitudinal ($\phi = 0^\circ$) and transverse samples ($\phi = 90^\circ$) (these samples are labelled Fxx-yy where xx = the angle ϕ , and yy indicates the applied stress)

4.2.2 Features of creep tested samples and the fracture surface

All creep tested specimens exhibited necking near the fracture surface to some extent, as shown in Figure 4.6. The fracture surface of each creep tested specimen has a common feature, which is shown in Figure 4.7. It can be seen that the fracture surface normally has two distinct regions with different surface colour. Dark oxide indicates long-time oxidation and thicker oxides, whilst bright coloured oxide indicates very short-time oxidation and very thin oxides. It is suggested that the dark region is where the crack initiated and the bright coloured region is where the final rupture happened. This feature can also be seen on the cross section of the fracture surface. In Figure 4.8, the image on the left is the SEM BSE image of cross section near the fracture surface. The top half fracture surface is covered with thick oxide film and bottom half surface has very thin oxide film, as shown at higher magnification in Figure 4.8a and 4.8b respectively.

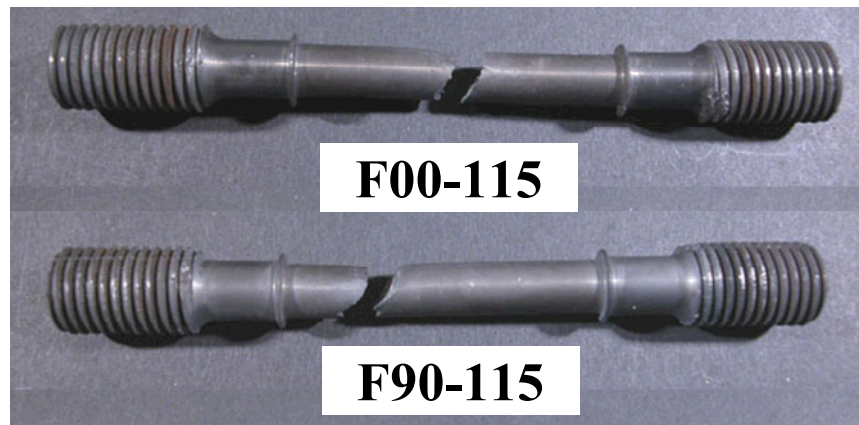


Figure 4.6 P91 weld metal specimens from both longitudinal (F00-115) and transverse (F90-115) orientations following creep tests at 650°C and 115 MPa

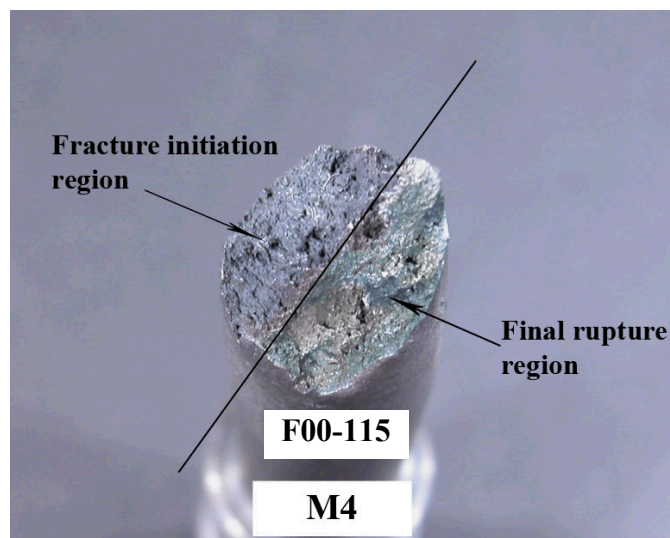


Figure 4.7 A digital photo showing the fracture surface of crept specimen (F00-115)

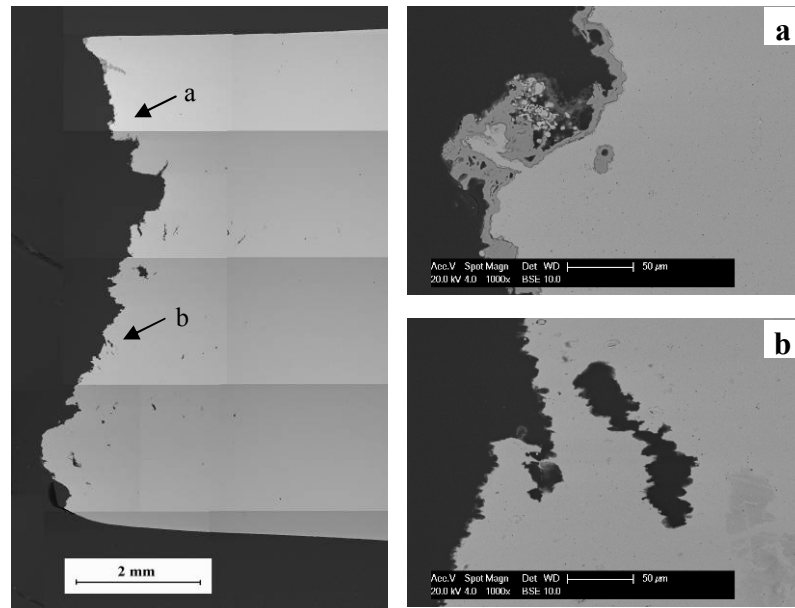


Figure 4.8 SEM BSE images of cross section of fracture surface (F00-115): (a) thick oxide on fracture surface; (b) very thin oxide on fracture surface

4.2.3 Features of creep fractures

Creep specimens from different orientations have been examined to reveal their failure mechanism. Figure 4.9 to 4.11 show the optical microstructural montages of creep tested specimens from both longitudinal and transverse orientations (F00-115, F90-115, F90-90) which had failed under creep at 650°C. Microstructure distribution is similar to that which has been observed in PWHT specimens, but with some additional light-etched white-bands being observed mostly at or near inter-bead boundaries. Regions of representative modes of failure have been indicated on the micrographs (Figure 4.9 to 4.11), broadly classified into two types: creep fractures in the columnar regions and creep fractures along the white-bands. Sources of fracture were not observed in the refined region since it has much higher creep ductility. The propagation of creep fracture is restricted by the ductility of the refined region.

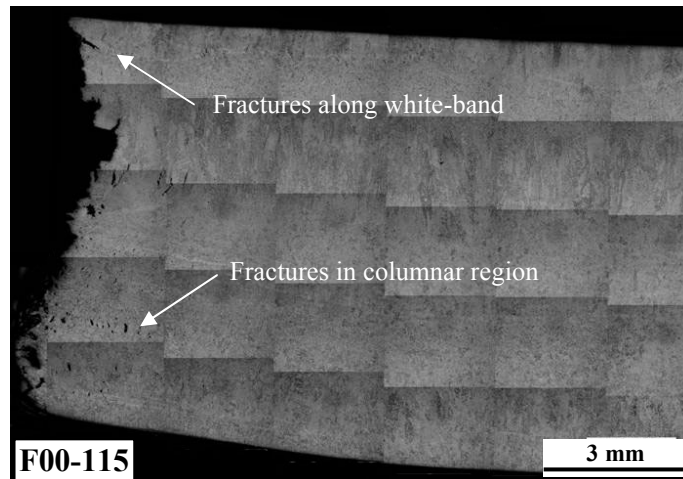


Figure 4.9 Optical micrograph montage of creep tested P91 weld metal specimen F00-115

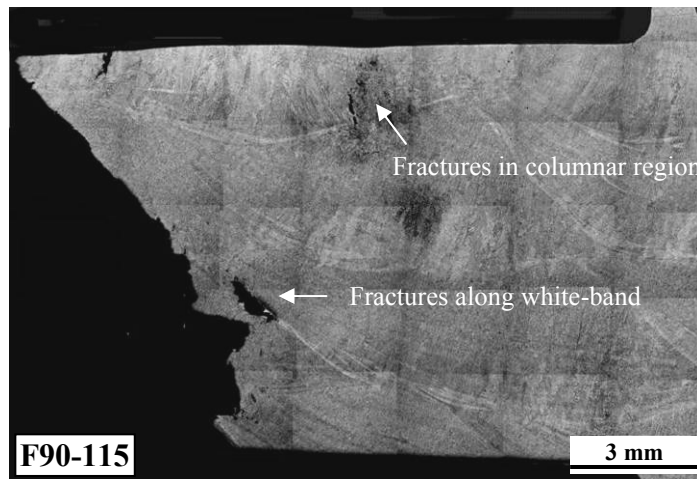


Figure 4.10 Optical micrograph montage of creep tested P91 weld metal specimen F90-115

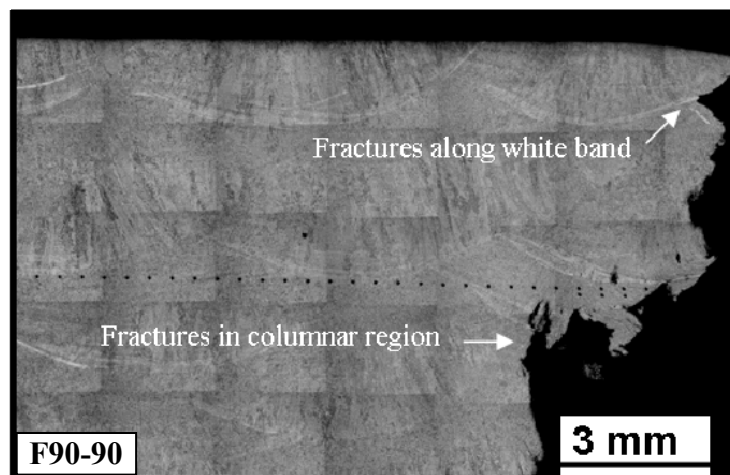


Figure 4.11 Optical micrograph montage of creep tested P91 weld metal specimen F90-90

Specimens from all orientations showed very clear evidence of creep fractures in the columnar region, as indicated in Figure 4.9 to 4.11. This is the typical weld metal creep fracture mode, which normally formed along coarse columnar grain boundaries. Optical and SEM micrographs of creep fractures in the columnar regions are shown in Figure 4.12, where Figure 4.12a and 4.12c represent the initial stages of fracture formation and Figure 4.12b and 4.12d illustrate the stage of fracture growth. These types of creep fractures are formed along the columnar grain boundaries associated with solidification. Figure 4.12c is an SEM image of a newly formed creep fracture in a columnar region, also showing the distribution of precipitates. It is observed that in the initial stage of creep, creep cavities started to form at grain boundaries where precipitates are present; these creep cavities then linked to each other to form creep fractures.

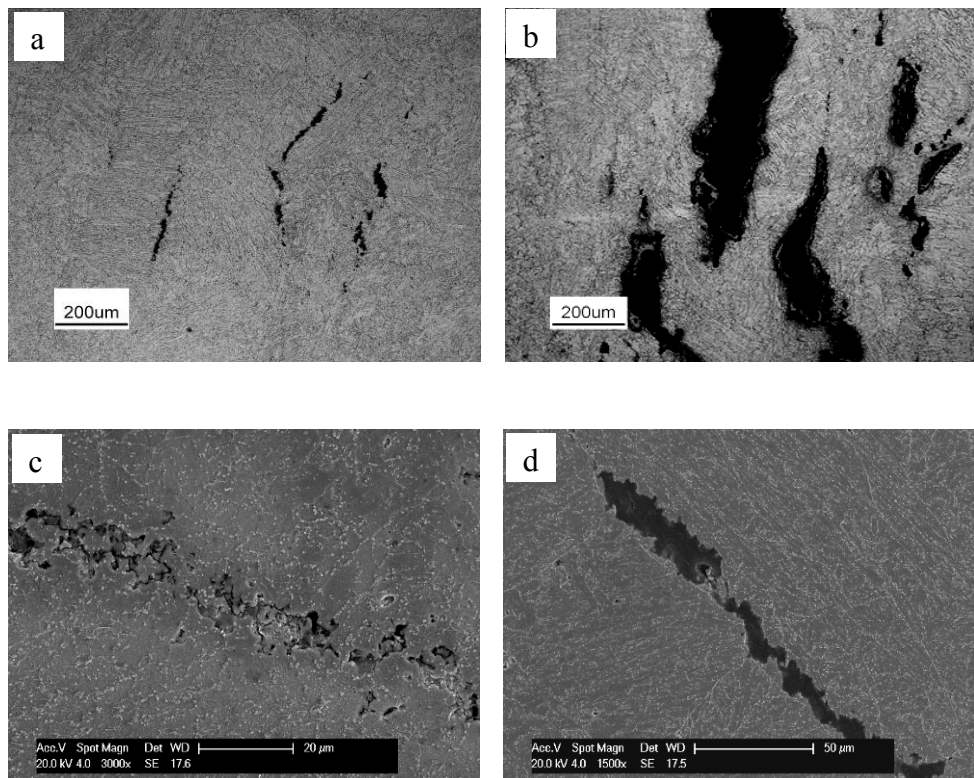


Figure 4.12 Micrographs of creep fractures at coarse columnar grain boundaries in creep tested P91 weld metal specimen (F00-115): Optical micrographs of fractures (a) just formed and (b) grown; SEM SE micrographs of fractures (c) just formed and (d) grown

Creep fractures were also found along the light-etched white-bands at the inter-bead fusion boundaries (Figure 4.9 to 4.11). Most of them occurred at an angle of approximately 45° to the stress axis. They are not as common and severe as the creep fractures in the columnar regions, but they can act as a linkage between the creep fractures in columnar regions (Figure 4.11). It was also found that the white-bands on transverse specimens were more vulnerable to the formation of creep fracture; in contrast, the white-bands in the longitudinal specimen did not normally lead to the formation of creep fractures. Optical and SEM micrographs of creep fractures along white-bands are shown in Figure 4.13. The mature fractures propagate along the white-bands at inter-bead fusion boundaries. It can be seen that there are less precipitates within the white-band region from the SEM micrographs in particular Figure 4.13c and 4.13d. Creep fractures along and within the white-band were observed at large distances from the final creep fracture face (Figure 4.14). Moreover, the damage in these positions was only observed in the white-bands, indicating the importance of these regions in the overall mode of failure. It is suggested that although the creep tested specimens mainly failed by the formation of creep fractures along the coarse columnar grain boundaries, creep fractures along the white-band regions were also commonly observed and considered to be an important contributor in the creep failure of the weld metal.

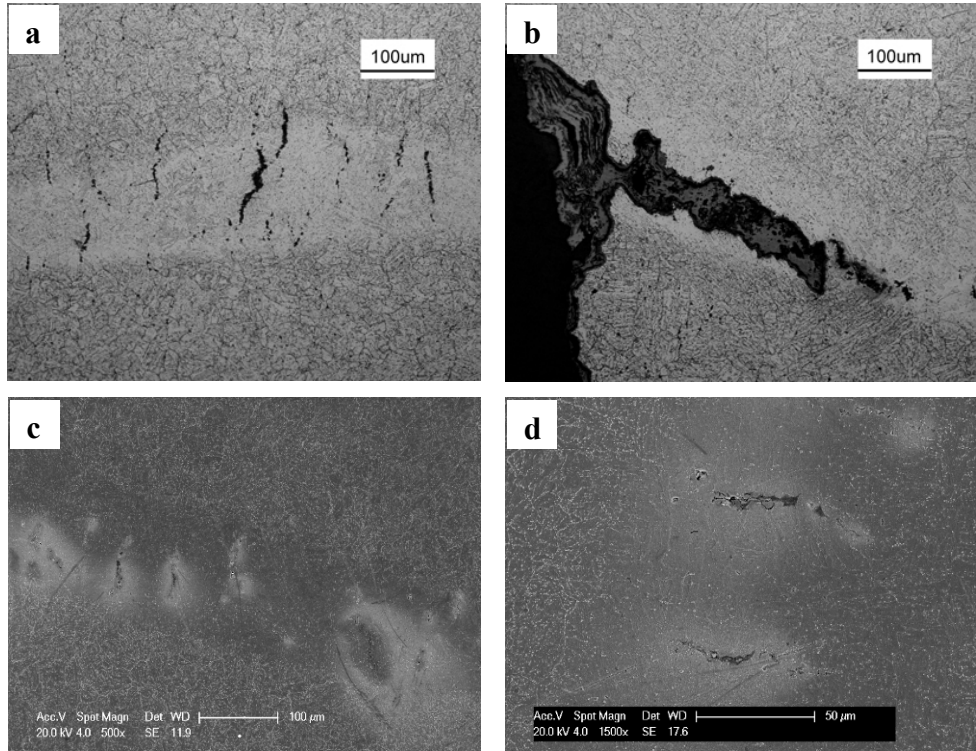


Figure 4.13 Micrographs of creep fractures along white-bands in creep tested P91 weld metal specimen (F00-115): Optical micrographs of fractures just (a) formed and (b) grown; (c) and (d) SEM SE micrographs of fractures

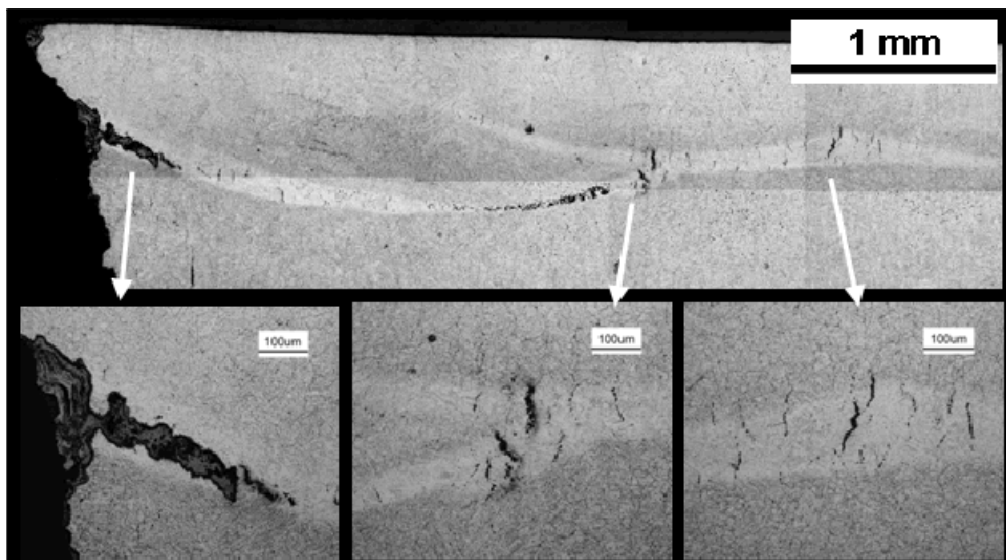


Figure 4.14 Microstructural montage of longitudinal creep tested P91 weld metal F00-115

4.2.4 Precipitates

Figure 4.15 shows the SEM images of as-PWHT P91 weld metal and creep tested P91 weld metal. Bright particles can be seen primarily at the grain boundaries, especially at prior austenite grain boundaries, as indicated by the arrow. By comparing the images before and after creep, the coarsening of the precipitates can be seen clearly; however, the numbers of precipitates did not appear to have changed significantly.

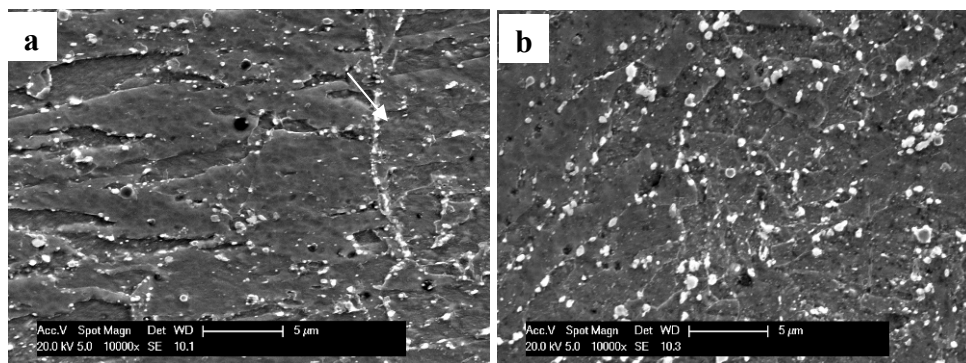


Figure 4.15 Precipitates on (a) as-PWHT and (b) creep tested P91 weld metal; samples etched to reveal precipitate distribution

The types of the precipitates were identified by TEM analysis. Figure 4.16 is the bright field TEM image of P91 weld metal, showing a typical fine martensitic lath structure with large precipitates along the grain boundaries. Figure 4.17a shows a precipitate which is around 150 nm size. It has been identified as an $M_{23}C_6$ precipitate, with EDX analysis showing it to be rich in chromium, as shown in Figure 4.17b. The TEM bright field image (Figure 4.18a) and dark field image (Figure 4.18b) of another $M_{23}C_6$ particle was observed, which was approximately 200nm in size. It was found that the size of $M_{23}C_6$ particles observed was in a range from 100 to 300 nm in length.

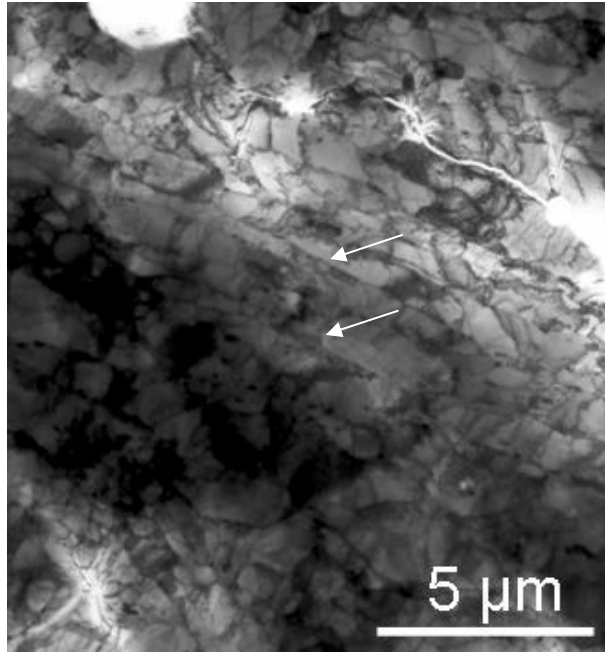


Figure 4.16 Bright field TEM image of martensite lath structure in creep tested P91 weld metal

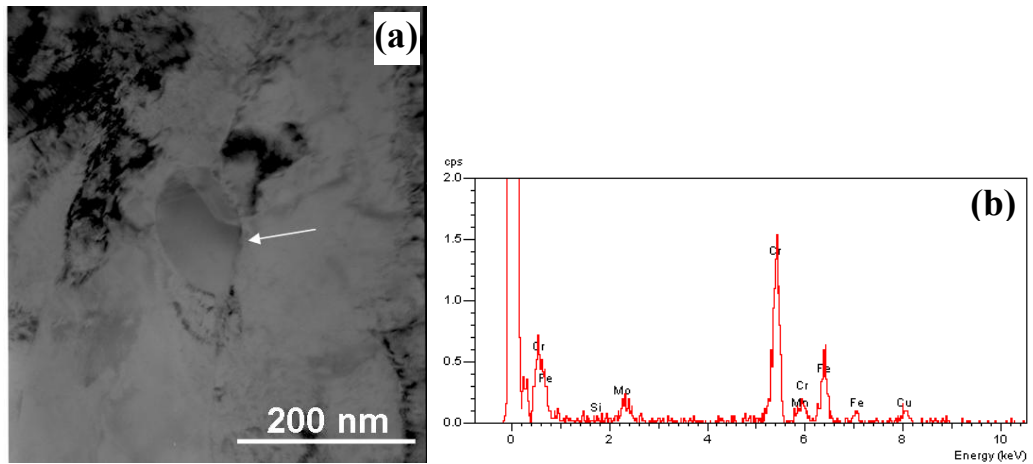


Figure 4.17 (a) TEM bright field image of an $M_{23}C_6$ particle in creep tested P91 weld metal; (b) EDX spectrum of the $M_{23}C_6$ particle

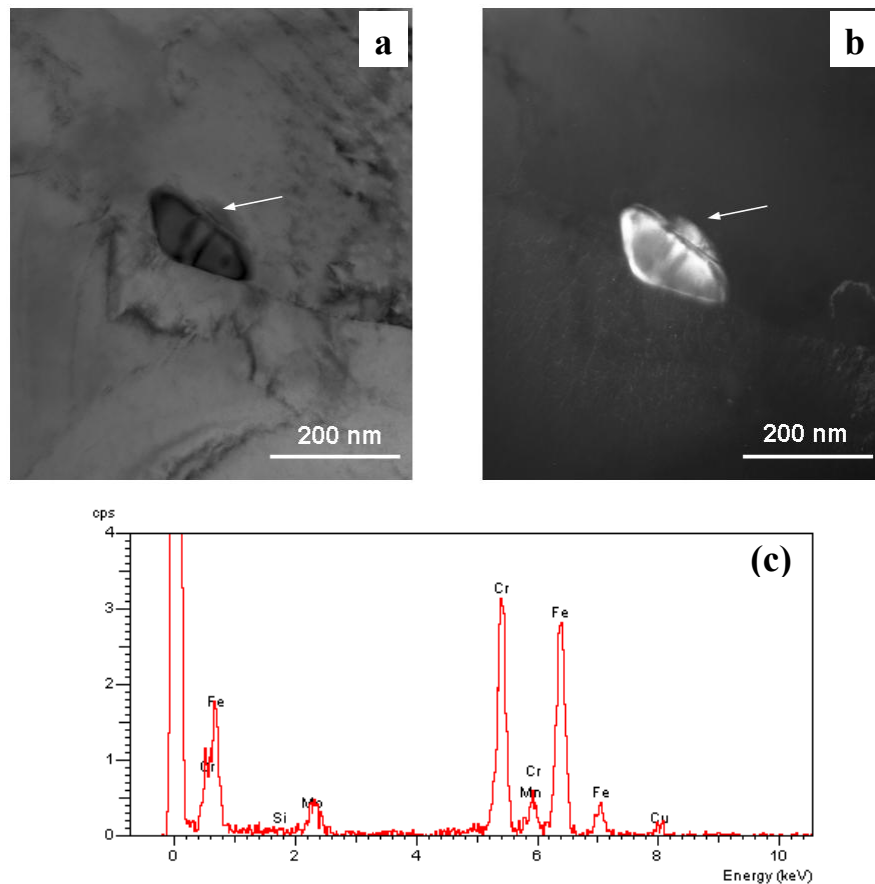


Figure 4.18 (a) TEM bright field image of an $M_{23}C_6$ particle in creep test P91 weld metal; (b) dark field image of the $M_{23}C_6$ particle; (c) EDX spectrum of the $M_{23}C_6$ particle

4.2.5 Hardness and strain

Figure 4.19 shows the plots of hardness along the stress axis of the different creep sample types (both longitudinal and transverse samples), from the fracture surface to the grip end. The line on the microstructural montage of the creep tested specimens (alongside each trace) indicates where the hardness indentations were made. The exact positions of the gauge and grip of each specimen are also indicated on the hardness plots. The stress in the gauge section is 115 MPa and the stress in the section between gauge and grip is around 95 MPa due to its larger diameter; the stress in the grip section is assumed to be zero. Both hardness traces exhibited very clear trends in that hardness becomes lower when it gets closer to the fracture surface. Hardness is generally reduced by more than 50 kgf mm⁻² from the grip end to the fracture

surface. The hardness did not reduce too much in the grip section due to its unstressed status during creep exposure; its hardness is similar to the hardness value of as-PWHT P91 weld metal. By comparing the hardness reduction in specimens from different orientations, it can be seen that transverse specimen F90-115 exhibited smallest hardness reduction, whilst the hardness of the longitudinal specimen F00-115 reduced to less than 200 kgf mm⁻² near the fracture surface.

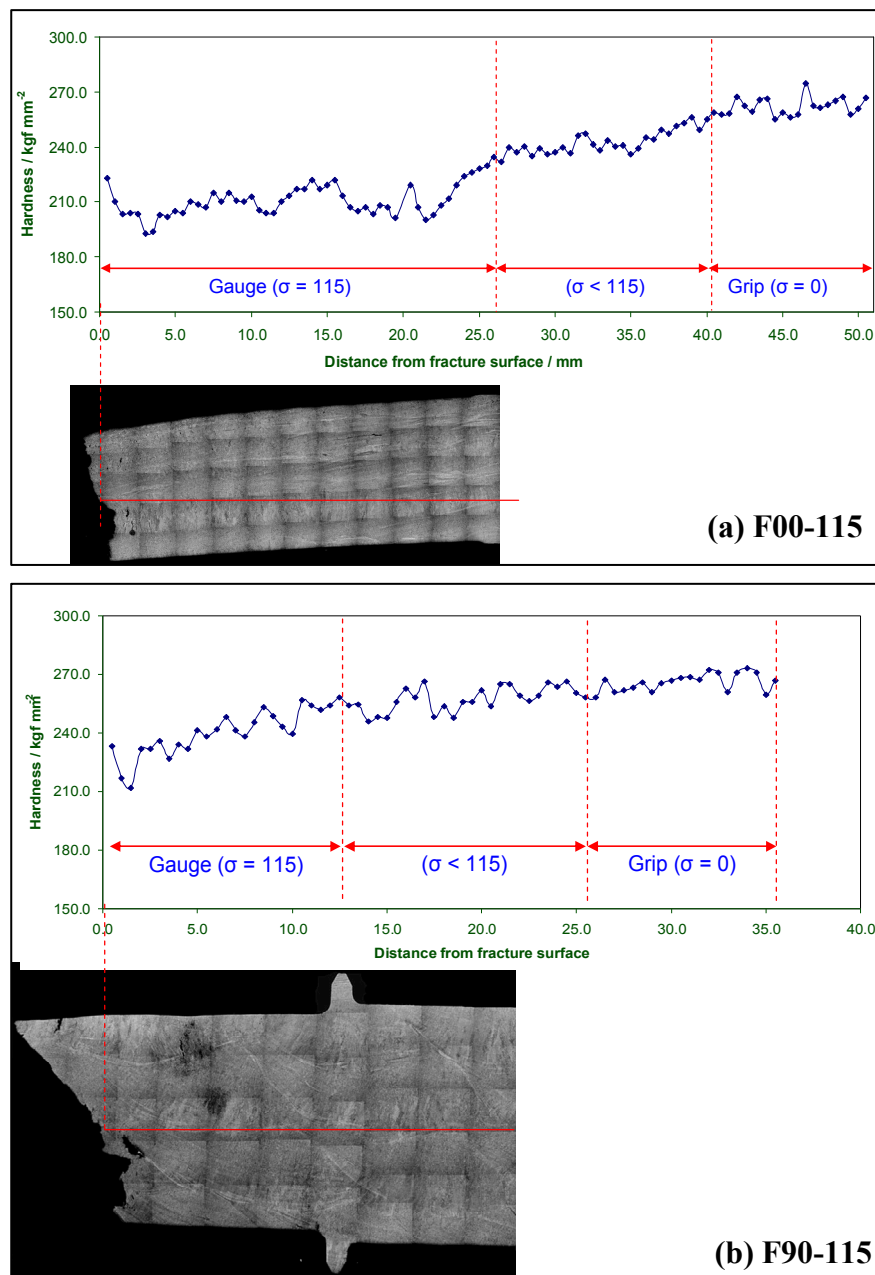


Figure 4.19 Hardness trace along stress axis on the creep tested specimens: (a) longitudinal, 115MPa; (b) transverse, 115MPa

In order to examine the relationship between strain and stress level in both longitudinal and transverse P91 weld metal specimens, the reduction in area (R_A) along the specimen axis was plotted against the distance from the grip end for both longitudinal and transverse specimens creep tested under various stress levels (80 MPa and 90 MPa), as shown in Figure 4.20. It can be seen that the reduction in area (R_A) ranged from approximately 2% up to 7% for longitudinal specimens with increasing stress level. The reduction in area (R_A) for transverse specimens are much lower, ranging from approximately 0% to 3% with increasing stress level. In both cases, higher stress during creep caused more serious deformation of the specimens, namely higher strain. In addition, the strains in the longitudinal specimens tended to increase sharply near the fracture surface, which was not observed in transverse specimens. Compared to the creep strain curves in Figure 4.5 and creep data in Table 4.2, it can be seen that longitudinal specimens with longer creep lives exhibited higher strain along the specimen axis and higher reduction in area at the cross section of the specimens. It is suggested that longitudinal specimens are more ductile than transverse specimens, resulting in their higher creep lives.

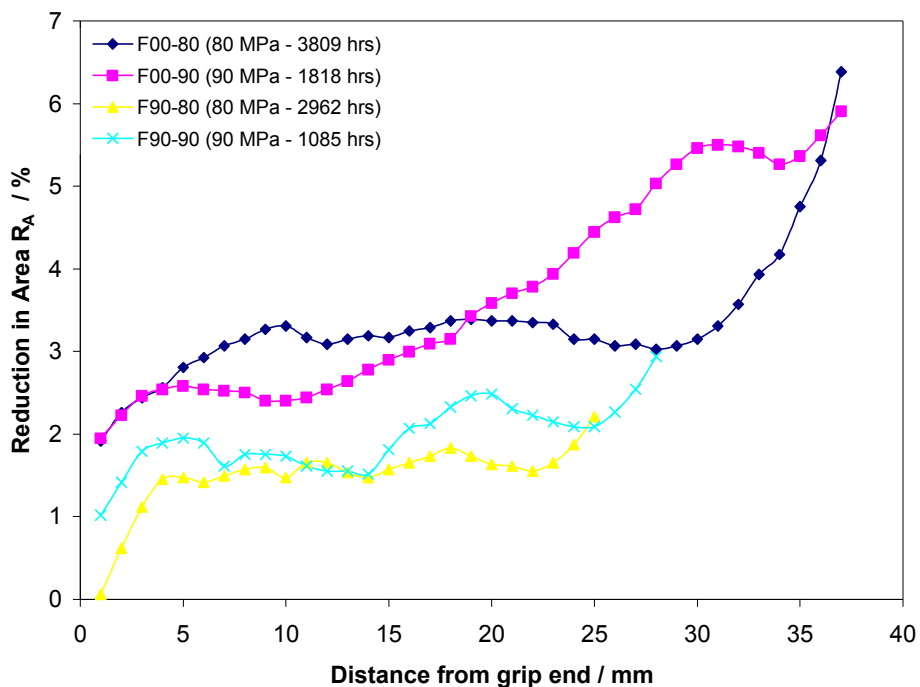


Figure 4.20 Reduction in area (R_A) along specimen axis of longitudinal and transverse P91 weld metal specimens creep tested at 650°C under two stress levels

4.3 CHARACTERISATION OF WHITE-BANDS IN P91 WELD METAL

Although creep cracks formed in the white-band regions are not the main type of creep cracks in weld metal, it has been noticed that they made significant contributions to the failure of the weld metal. However, the features and formation of white-bands have not been extensively investigated and studied. In this work, in order to understand the formation mechanism of white-bands, the characteristics of these regions have been explored.

4.3.1 Microstructural features of white-bands

White-bands have been frequently observed in creep tested P91 weld metal specimens. Most of them were at or near the inter-bead fusion boundaries; some of them were occasionally found within the weld bead, as shown in Figure 4.21, where examples of white-bands at inter-bead fusion boundaries are indicated as A, whilst examples of white-bands within the weld bead are indicated as B. It has also been noticed that not every inter-bead fusion boundary has developed a white-band during creep exposure. Moreover, all white-bands are not visually exactly same in terms of the reaction to etching: some of them are more obvious in etched micrographs than others.

However, there was no evidence of white-bands in the micrographs of the PWHT P91 weld metal (PWHT: 3 hours at 760°C). This suggested that white-bands developed during the long-term creep exposure. It was also found that in creep tested specimens white-bands did not only form in the gauge section where the stresses and strains were high, but they also formed in the grip section which was stress-free and strain-free. This indicated that the thermal condition during creep exposure was the main cause of white-band formation, rather than the stress and strain.

Although all white-bands did not necessarily lead to creep cracks, they are clearly potential locations where creep cracking can initiate. Figure 4.22 shows the optical micrographs of different white-bands which have not led to creep cracks, whereas Figure 4.23 shows the optical micrographs of white-bands which have led to creep cracks. The width of white-bands observed ranged from 50 μm to 200

μm . The thick oxides at some of these creep fracture surfaces indicated that creep fractures along white-bands can form at an early stage of creep exposure.

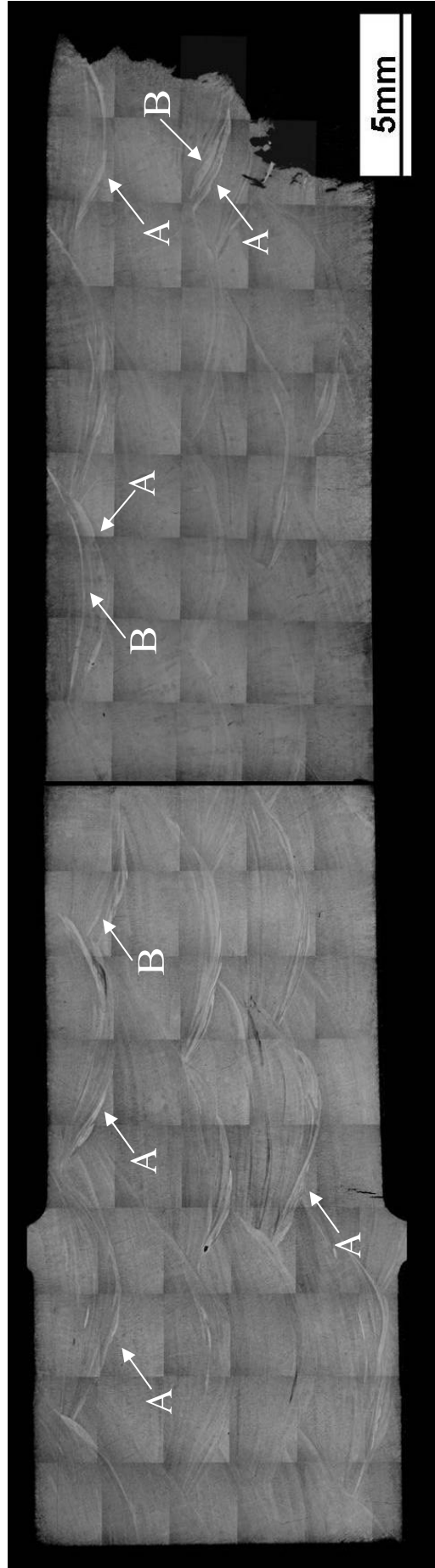


Figure 4.21 Optical micrograph montage of creep tested weld metal specimen F90-90 ($\phi = 90^\circ$ (transverse), $T=650^\circ\text{C}$, $\sigma = 90 \text{ MPa}$, $t_f = 1085$

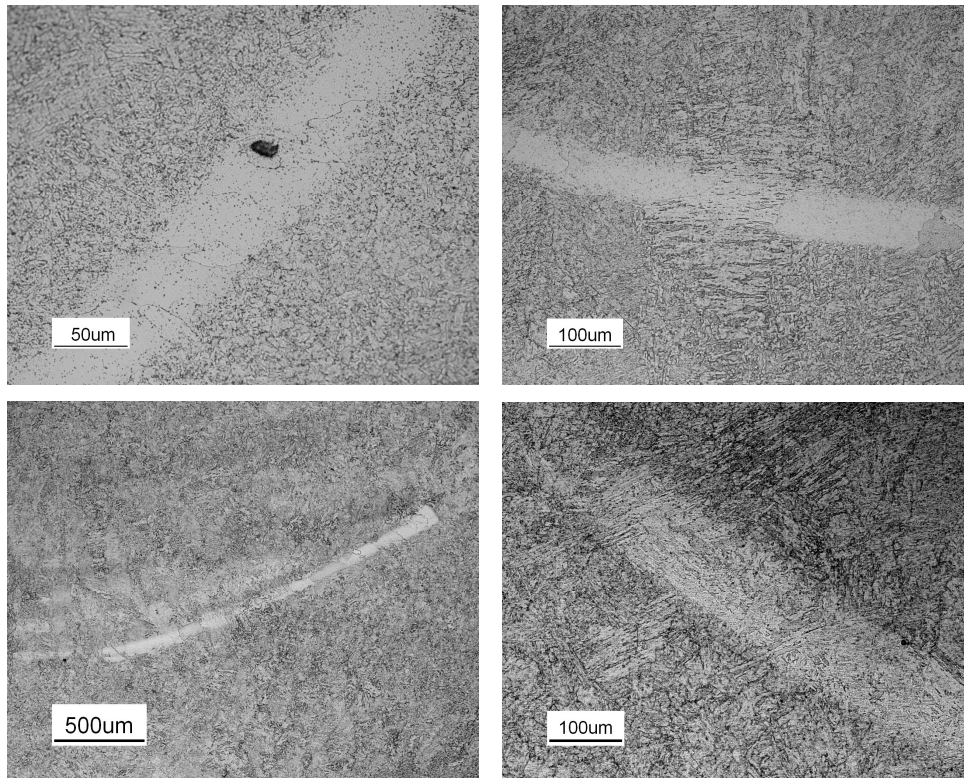


Figure 4.22 Optical micrographs of white-bands in creep tested P91weld metal. No creep damage is associated with these white-bands

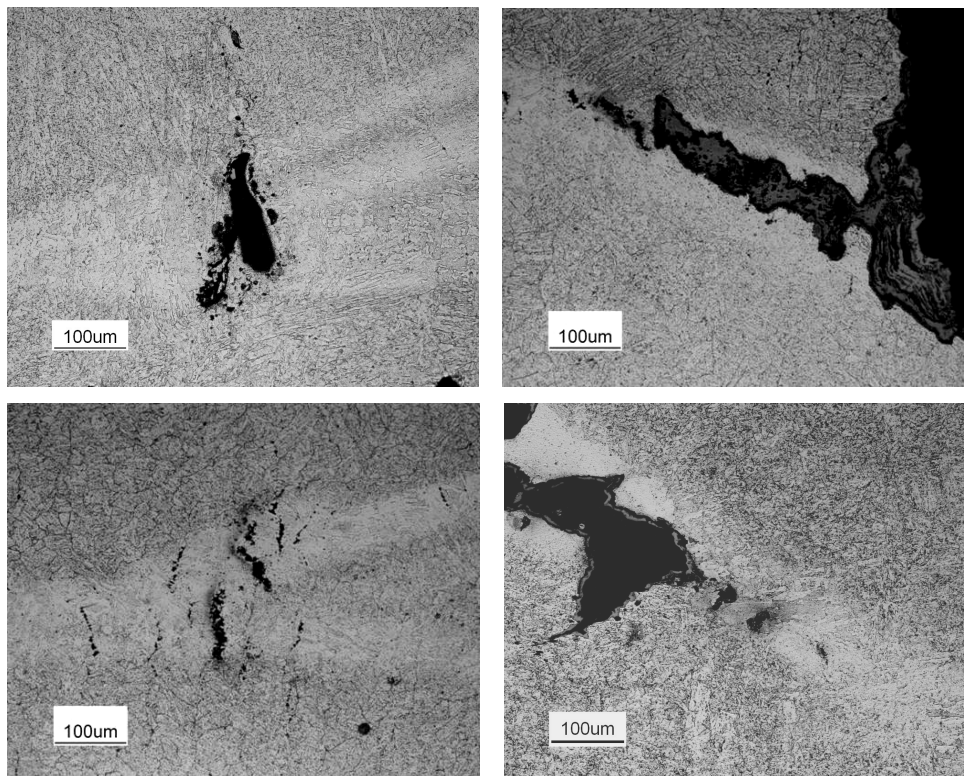


Figure 4.23 Optical micrographs of creep cracks formed at white-bands in creep tested P91 weld metal

Electron backscattered diffraction (EBSD) analysis has also been carried out to investigate the crystallographic nature of the white-band region in comparison to that of the surrounding material. Figure 4.24 shows an optical micrograph along with the corresponding inverse pole figure map and rotation angle map in a white-band region at inter-bead fusion boundary, indicating two large grains in the white-band (each making up its full width) surrounded by the martensitic structure typical of such welds. It indicates that the white-band has a fully recrystallised structure, consisting large ferrite grains. EBSD analysis was also conducted on white-bands within the weld bead, as seen in Figure 4.25. It showed that the crystallographic features are exactly same as those of the white-bands at inter-bead fusion boundaries.

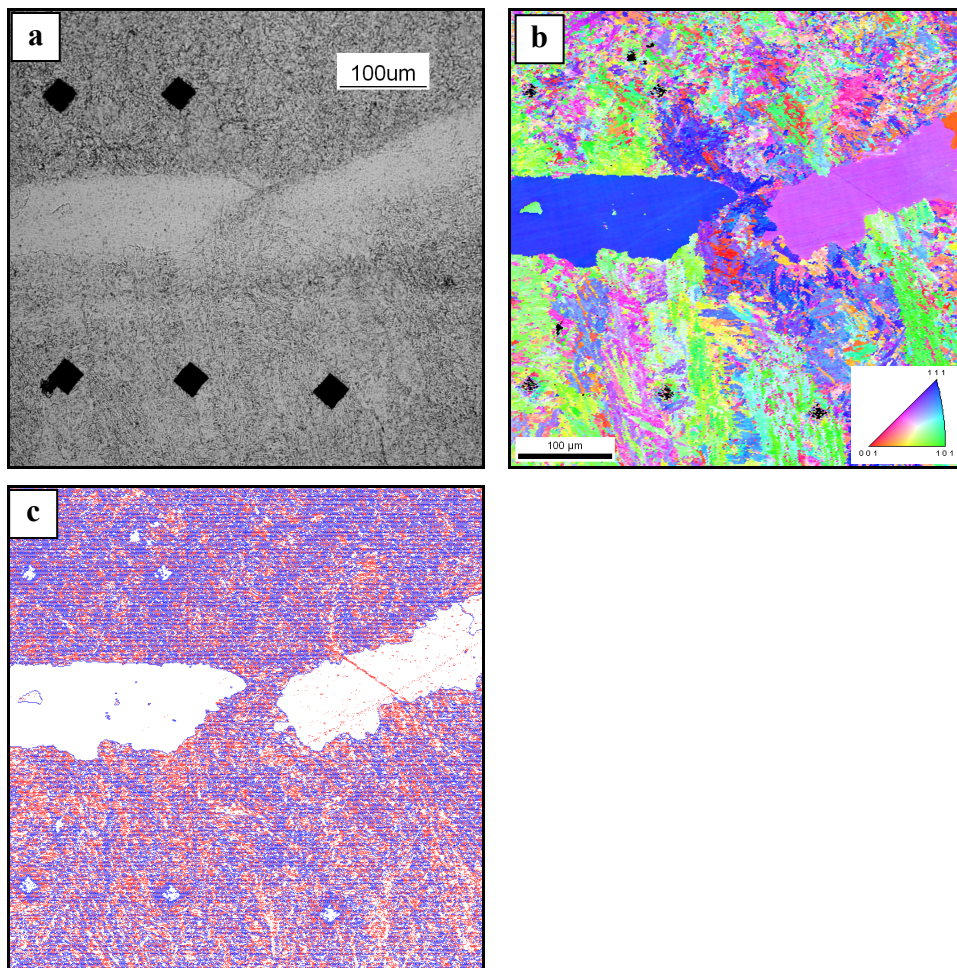


Figure 4.24 EBSD analysis on a white-band at inter-bead fusion boundary of creep tested P91 weld metal: (a) Optical micrograph of a white-band region; (b) inverse pole figure map. The unit triangles shows the crystallographic poles aligned with the specimen surface normal direction; (c) low angle boundaries (2-10°) are shown as red and high angle boundaries (10-180°) are shown as blue

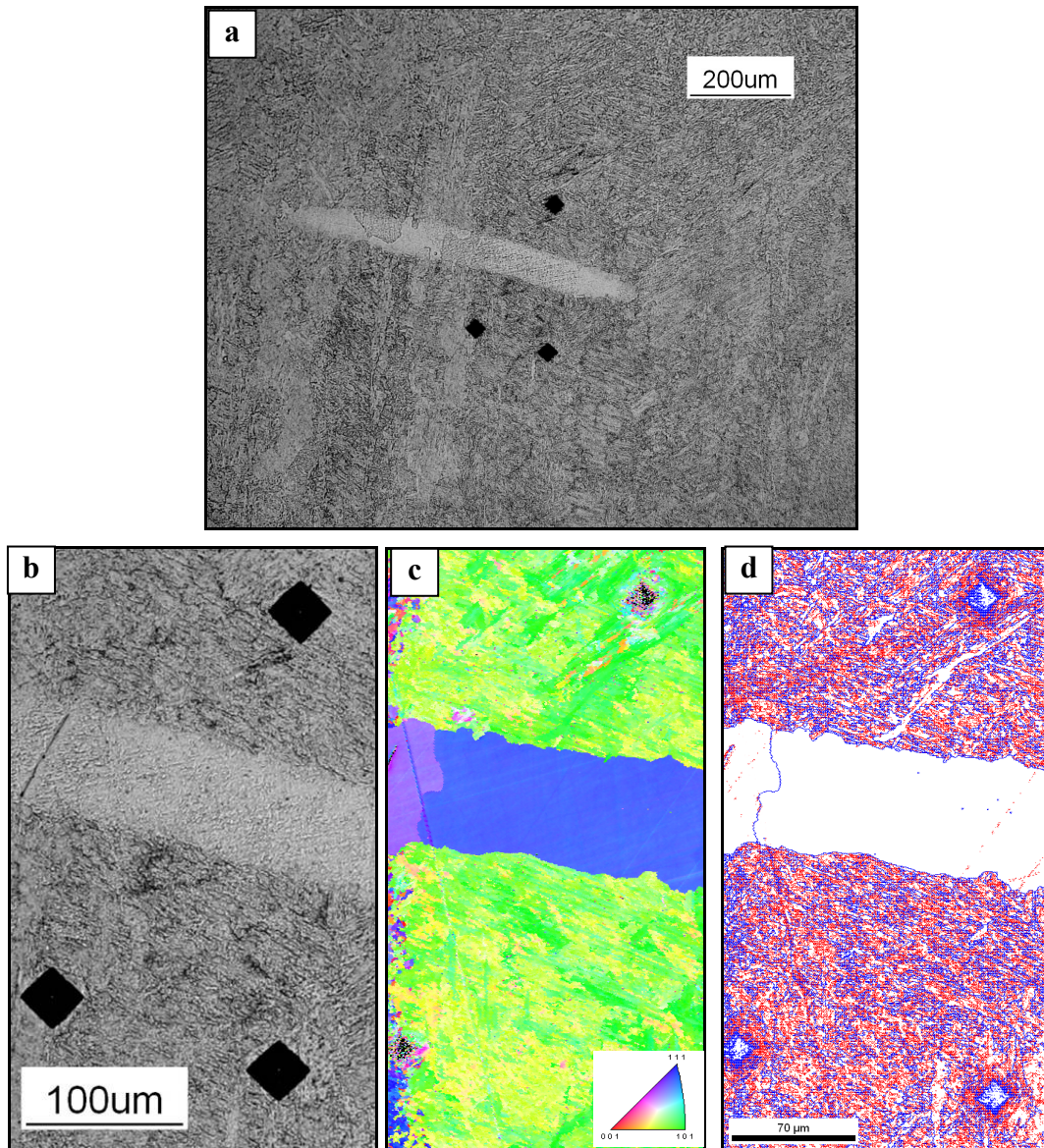


Figure 4.25 EBSD analysis on a white-band within the weld bead of P91 creep tested weld metal: (a) optical micrograph of the white-band region within the weld bead; (b) optical micrograph indicating the EBSD analysis area; (c) inverse pole figure map. The unit triangles shows the crystallographic poles aligned with the specimen surface normal direction; (d) low angle boundaries ($2-10^\circ$) are shown as red and high angle boundaries ($10-180^\circ$) are shown as blue

4.3.2 Precipitates

Figure 4.26a shows the SEM secondary electron (SE) images of a white-band region formed in creep tested P91 weld metal. The sample has been lightly etched to allow the strengthening precipitates to be observed. It is clear that the white-band region (Figure 4.26c) is significantly depleted in precipitates compared to the bulk weld metal (Figure 4.26b).

Figure 4.27 shows the micrograph montage of a creep tested P91 weld metal specimen with twelve white-bands locations as indicated, and the SEM SE images of white-bands at several locations (1, 4, 9 and 10) showing the depletion of precipitates. The examination of a number of white-bands throughout the structure revealed that in all cases, the precipitate density was reduced in the white-band when compared to the surrounding weld metal, but the level of depletion varied from one white-band to another. These large precipitates have been identified as the $M_{23}C_6$ type, rich in chromium (via TEM characterisation), located at grain boundaries and subgrain boundaries.

The volume fraction of the large precipitates was measured from the etched SEM SE micrographs, using Image J software. For all twelve white-band locations as shown in Figure 4.27, the volume fraction of the large precipitates was measured both inside and outside the white-band at each location respectively. The results are plotted in Figure 4.28a. The volume fraction of $M_{23}C_6$ carbides in bulk weld ranged from 2.1% to 3.3%, whilst that in white-band ranged from 0.1% to 1.0%. White-band locations 9 and 10 have lowest volume fraction of $M_{23}C_6$ carbides. Figure 4.28a and 4.28b are the SEM SE images of white-band location 5 and 7 respectively, with clear evidence that the white-band at location 5 possessed relatively lower precipitates than the white-band at location 7.

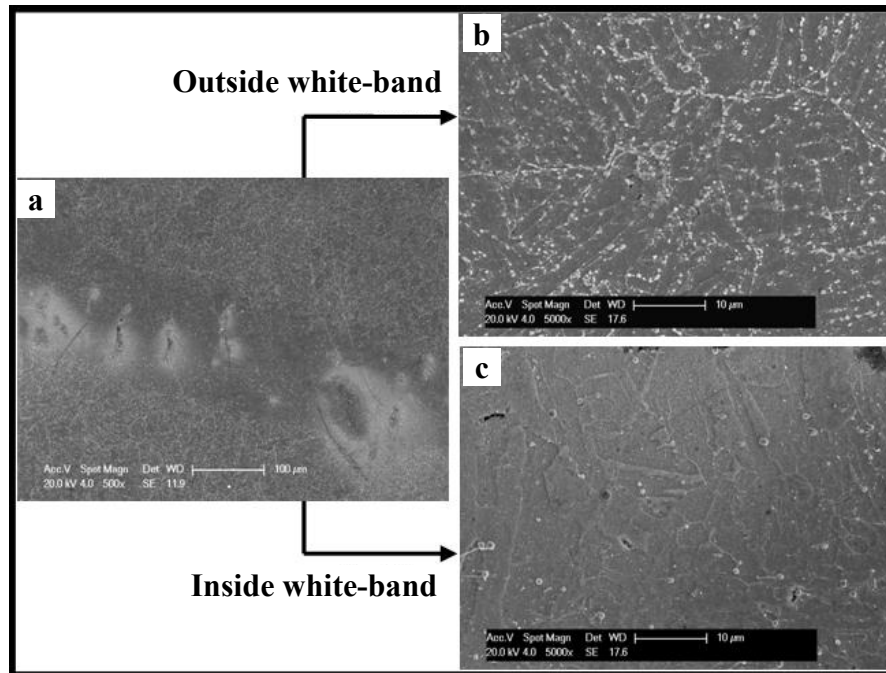


Figure 4.26 SEM images showing the depletion of precipitates in white-band of creep tested P91 weld metal. (a) SEM SE image of a white-band region; (b) SEM SE image of bulk weld (outside the white-band); (c) SEM SE image inside the white-band

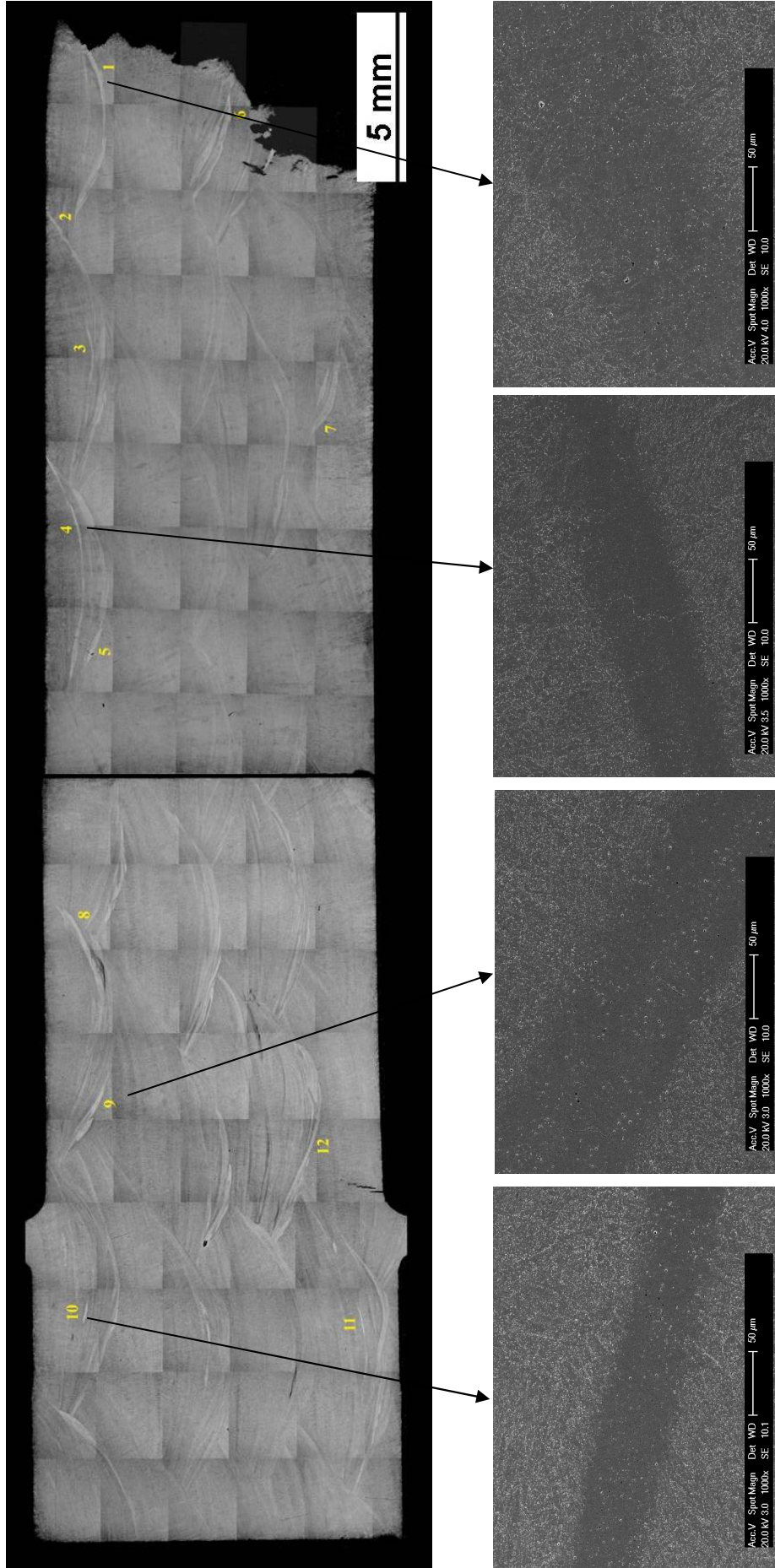


Figure 4.27 SEM SE images showing the depletion of precipitates in different white-band locations of specimen F90-90 ($\phi = 90^\circ$, transverse, 650°C , $\sigma = 90\text{ MPa}$, $t_f = 1085\text{ hrs}$).

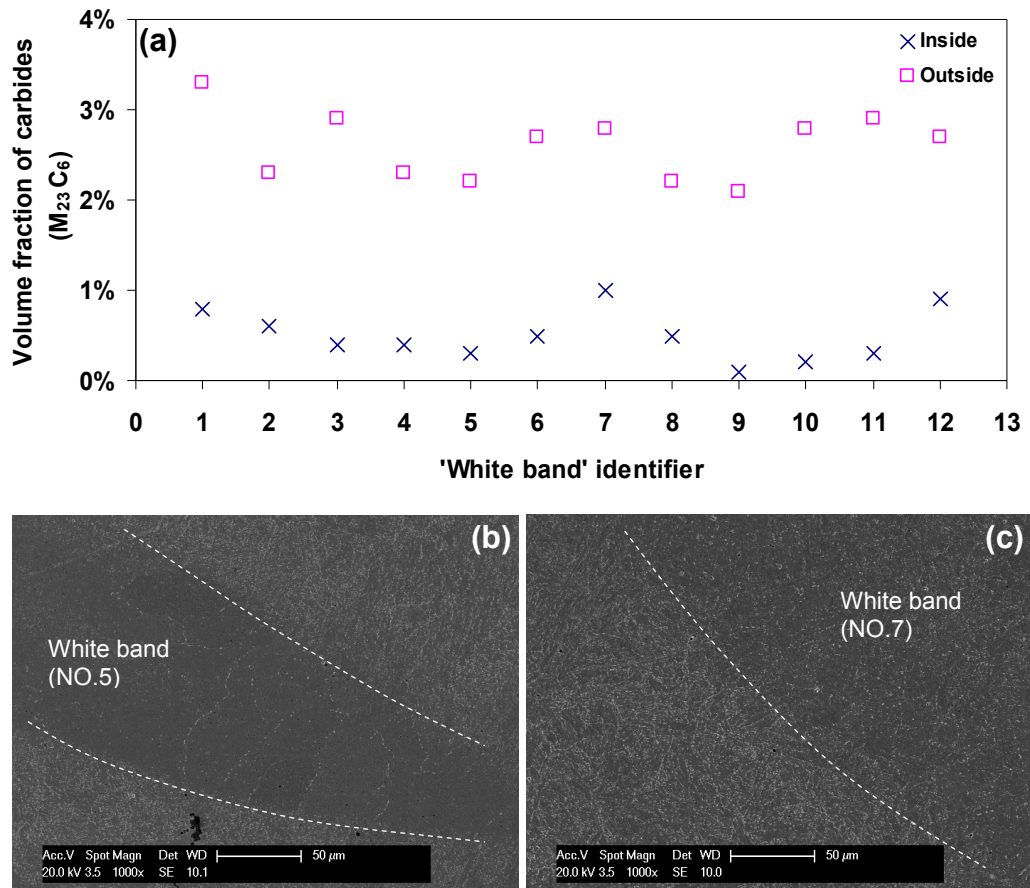


Figure 4.28 (a) Volume fraction of carbide precipitates inside and outside the white-bands in creep tested P91 weld metal (white-band locations as indicated in Figure 4.27); (b) SEM SE image of white-band location 5; (c) SEM SE image of white-band location 7

TEM samples were also produced from a number of white-band regions via FIB milling and extraction techniques. Figure 4.29 shows the position of a typical sample extraction from the white-band region. The TEM analysis confirmed that the white-band has a very low density of carbide precipitates when compared to the surrounding weld metal. Figure 4.30 shows a low magnification TEM image of a FIB-extracted foil in the mount into which it had been welded. The sample was 4 × 10 μm in size. It was typical of such samples, where the selected area diffraction patterns revealed that the whole samples were within a single grain. This is in contrast to the fine martensite structure observed in bulk weld (Figure 4.16). The fully recrystallised structure of the white-band has also been confirmed

previously by EBSD with the inverse pole figure mapping and rotation angle mapping of white-band region (Figure 4.24 and 4.25).

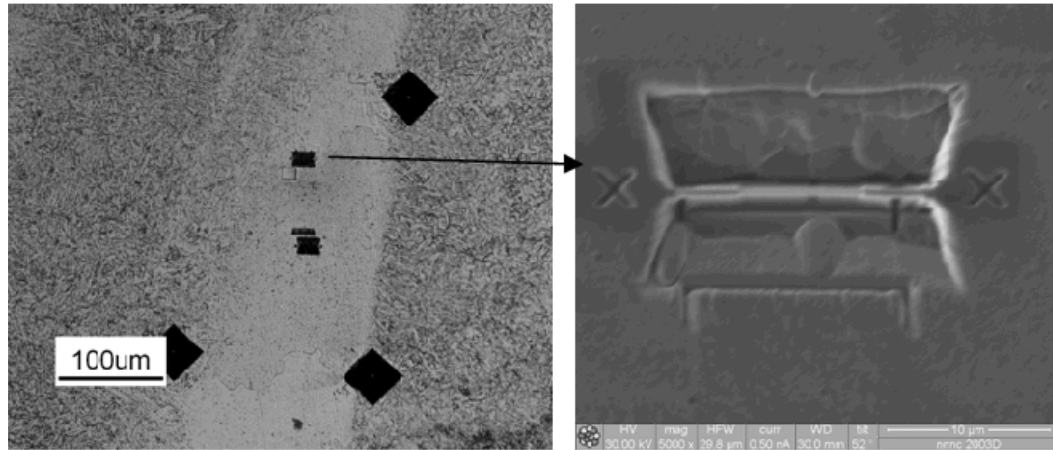


Figure 4.29 TEM thin foil sample of white band region produced by FIB

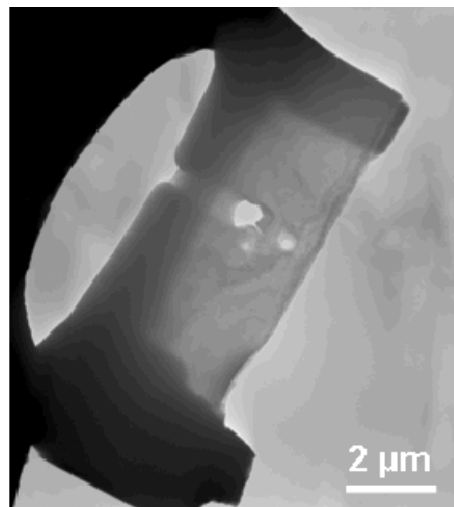


Figure 4.30 Low magnification TEM image of FIB TEM sample of white-band region

In line with the SEM observations (Figure 4.26 and 4.27) and measurement of volume fraction of carbide precipitates (Figure 4.28) in the white-band regions, the TEM analysis of the white-bands revealed an absence of the large $M_{23}C_6$ carbides. However, some small precipitates were observed, typically associated with dislocation pinning. Figures 4.31 and 4.32 show examples of small precipitates observed in the white-bands of creep tested P91 weld metal. The size of these

small precipitates is approximately in a range from 50 nm to 80 nm. The EDX analysis of such particles in the TEM revealed that they were rich in vanadium (Figure 4.31b and 4.32b); it is assumed that these are as vanadium nitride (VN) precipitates as commonly observed in P91 steels (Maruyama et al., 2001).

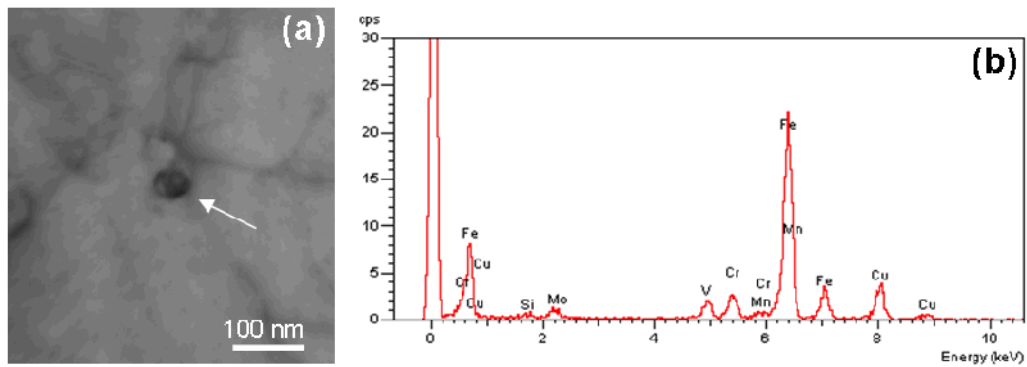


Figure 4.31 TEM image of small precipitates in white-band region: (a) bright field TEM image of small vanadium rich particle; (b) EDX spectrum of small particle in (a)

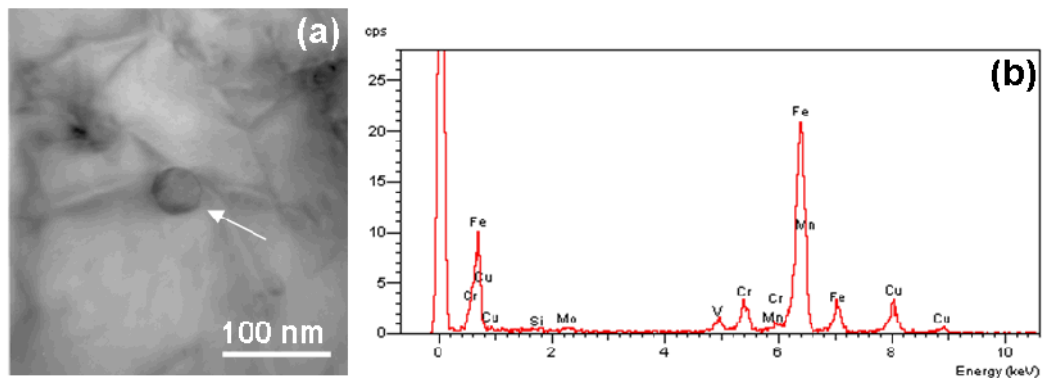


Figure 4.32 TEM image of small precipitates in white-band region: (a) bright field TEM image of small vanadium rich particle; (b) EDX spectrum of small particle in (a)

4.3.3 Hardness

The hardness testing of white-bands has been conducted in creep tested P91 weld metal. Figures 4.33 and 4.34 show the results of hardness examination in a P91 weld metal specimen creep tested at 650°C and 90 MPa. Figure 4.33a shows a micrograph of a white-band following hardness testing, with the position of the hardness indentations observable. Ten hardness indents with 50µm spacing were carried out across the white-band. Figure 4.33b shows the hardness values at the positions indicated; the fifth and sixth indents were in the white-band region, showing hardness values much lower than those of the bulk weld.

In light of the variability of carbide depletion in different bands, hardness testing was carried out in twelve different white-bands within the sample as indicated in Figure 4.27. For each white-band, three hardness indentations were placed inside the band and three outside the band respectively and the average hardness values both inside and outside each band were measured. The values of the average of the hardness values both inside and adjacent to each white-band are shown in Figure 4.34. It can be seen that the hardness values inside the white-bands are significantly lower than those outside the white-bands for all the bands examined. The difference in the hardness between the white-band and adjacent bulk weld metal ranged from ~29 to 118 kgf mm⁻². Comparing the hardness distribution (Figure 4.34) to the volume fraction of carbides (Figure 4.28) at the twelve white-band locations, a correlation can be seen (see Figure 4.35), where the white-bands with lowest hardness values (location 4, 5, 6, 9 and 10) had lowest volume fraction of M₂₃C₆ carbides. In general, a linear correlation can be seen, where white-bands with higher volume fractions of carbides exhibited higher hardness values.

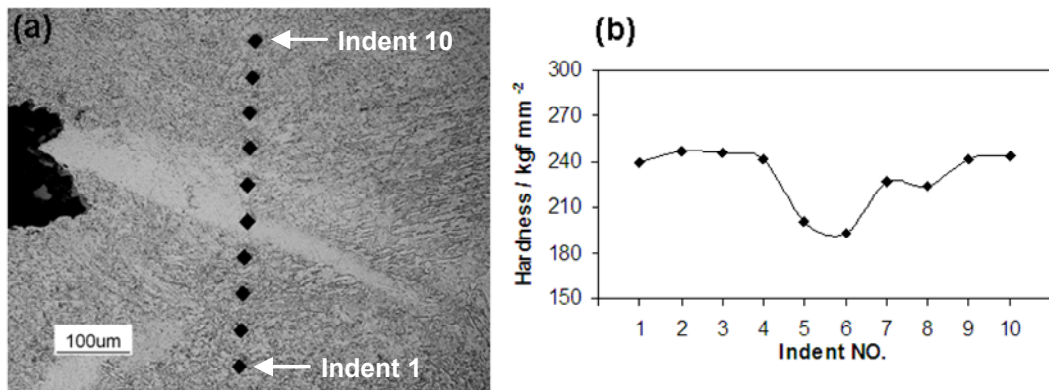


Figure 4.33 Hardness measurement of white-band in P91 weld metal creep tested at 650°C and 90 MPa (load of hardness measurement: 50 gf): (a) Optical micrograph showing hardness indents across white-band; (b) Hardness values across the white-band in (a).

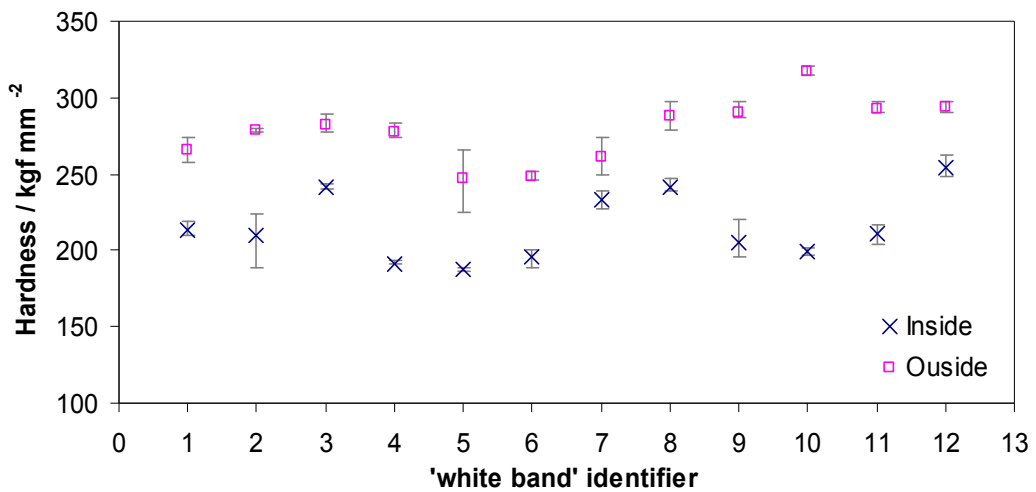


Figure 4.34 Hardness distributions inside and outside the white-band in P91 weld metal creep tested at 650°C and 90 MPa (white-band locations as indicated in Figure 4.27)

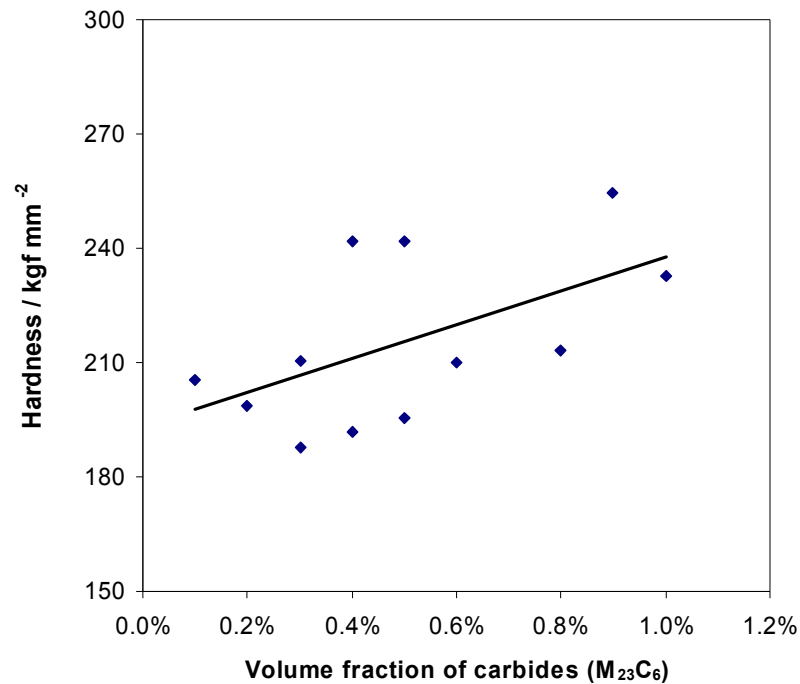


Figure 4.35 Correlation between hardness and volume fraction of carbides (M₂₃C₆) in white-bands of creep tested P91 weld metal (Specimen F90-90)

4.3.4 Element distribution

The depletion of carbide precipitates in the white-bands indicated that there is a depletion of chromium and/or carbon in the region, which are the two dominant elements in M₂₃C₆ carbides. The composition of the white-band regions were measured using EDX to compare with the surrounding bulk weld metal. Due to the limitation of EDX on carbon analysis, LIBS was also applied to measure carbon content. In addition, LIBS has also been used to provide the element mapping of a large area covering several weld beads and white-band regions, both qualitatively and quantitatively.

4.3.4.1 EDX results

Figure 4.36 shows the results of an EDX line scan across a white-band in P91 weld metal creep tested at 650°C and 115 MPa. As shown in Figure 4.36a, the line scan was carried out along a line of 362 µm long across the white-band. The position of white-band within this line can be seen, with the white-band being

approximately 130 μm wide. Figure 4.36b shows the line scan results of each element; the depletion of chromium in the white-band regions can clearly be seen. However, there is no clear evidence of depletion of other elements from the EDX line scan results.

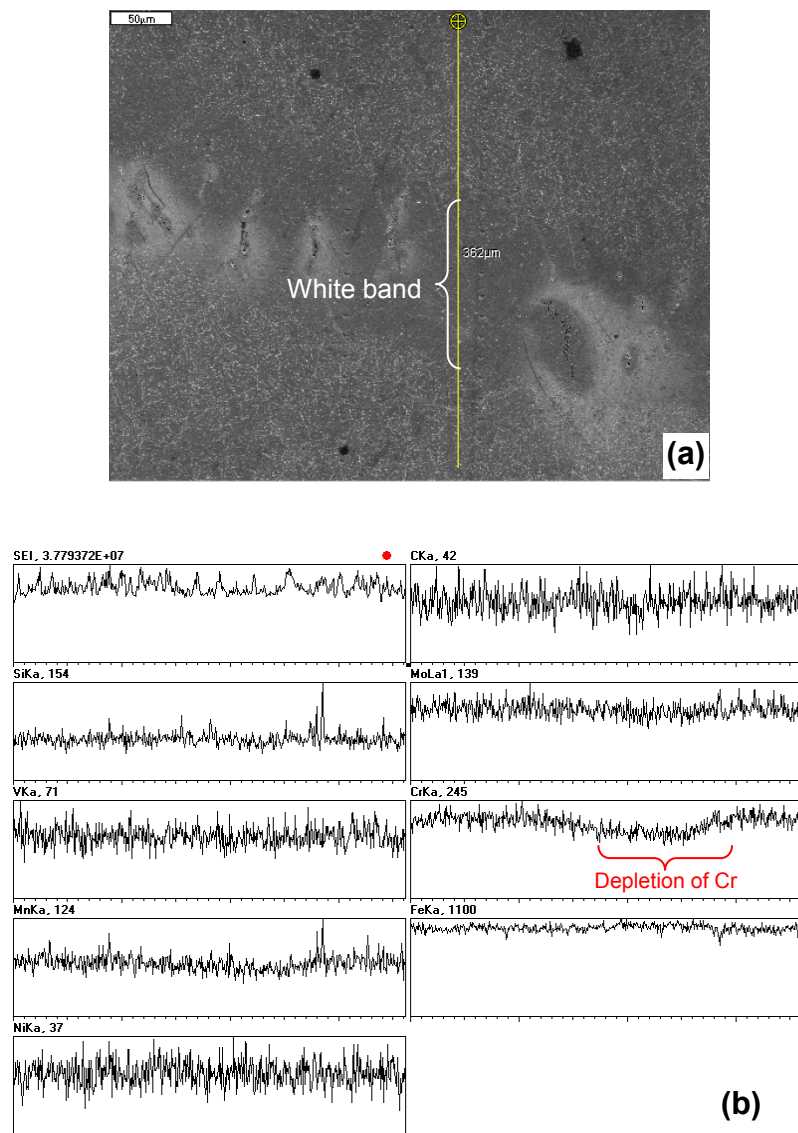


Figure 4.36 EDX line scan across the white-band in P91 weld metal creep tested at 650°C and 115 MPa: (a) SEM SE image showing the line scan position across the white-band; (b) EDX line scan results of element distribution across the white-band

In order to quantify the depletion of chromium and possibly other elements, more accurate EDX analysis was conducted by taking several long-count-time EDX measurements of small frames across the white-band, as shown in Figure 4.37a. Fifteen frames across the white-band were analysed, with each frame of $25 \times 25 \mu\text{m}$. This white-band is approximately $130 \mu\text{m}$ wide and is covered by five EDX frames from 6 to 10. The plots of Cr, Mn, Mo and V distribution across the white-band are shown in Figure 4.37b to 4.37e respectively. The depletion of chromium in white-band is confirmed again (Figure 4.37b), with the reduction of the chromium content in the white-bands compared to the surrounding bulk weld being up to 1.5 wt%. Manganese also exhibited slight depletion in the white-band (Figure 4.37c). Other elements such as molybdenum and vanadium did not show clear evidence of depletion (Figure 4.37d and 4.37e).

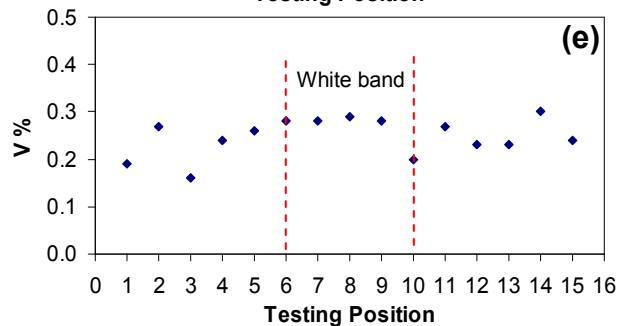
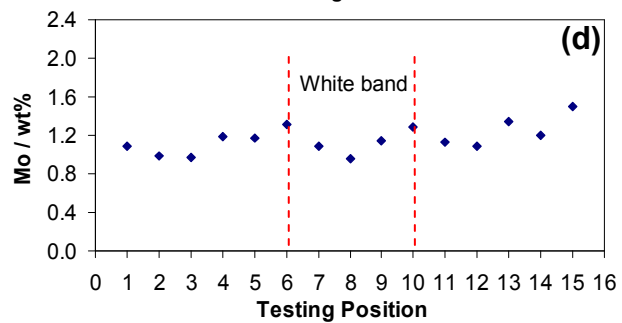
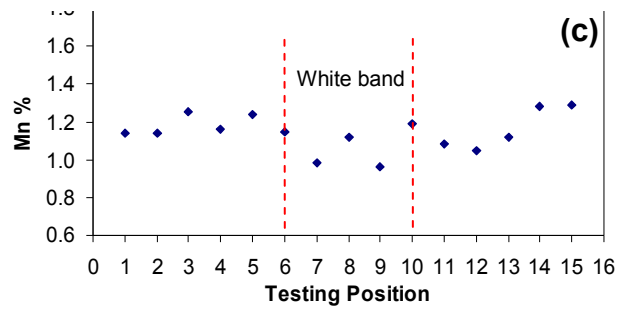
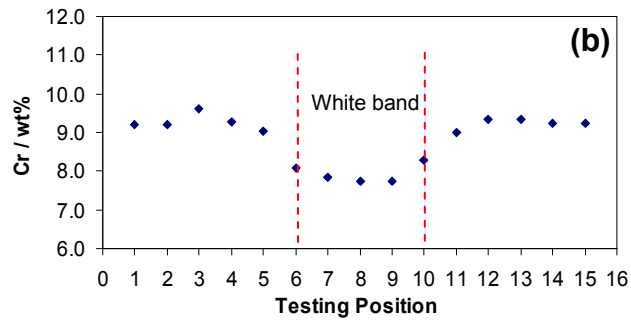
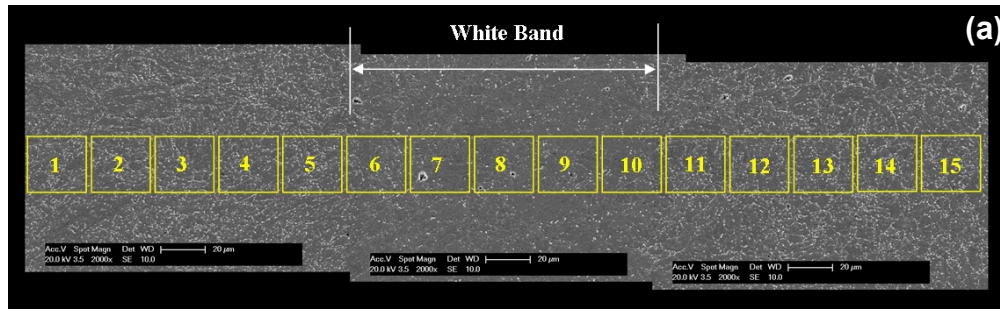


Figure 4.37 EDX analyses of element distributions across the white-band in P91 weld metal creep tested at 650°C and 90 MPa: (a) SEM micrograph montage of white-band showing the EDX analysis locations; (b) Cr distribution; (c) Mn distribution; (d) Mo distribution; (e) V distribution.

It has been shown that different white-bands exhibited different levels of depletion of carbide precipitates (Figure 4.28); hence the level of element depletion in different white-bands is expected to vary from one to another. The chemical analysis of different white-bands using EDX analysis was carried out on the P91 weld metal specimen creep tested at 650°C and 90 MPa (Figure 4.27) which is same specimen which was analysed for hardness testing (Figure 4.34). A similar data processing method as used in hardness analysis was applied to provide the distributions of main alloying elements in the twelve locations where the hardness testing was conducted, for materials both inside the white-bands and adjacent to them. The average chemical compositions inside and adjacent to each of the twelve white-bands are shown for each element in Figure. 4.38. Of all the elements, only chromium (Figure 4.38a) exhibited a consistent and significant difference between the white-band and the surrounding weld metal, with a chromium depletion in the white-band regions from 1 wt% to 2 wt% being observed. The manganese and molybdenum contents (Figure 4.38b and 4.38c) also exhibited some depletion in the white-band regions; in some locations, the depletion of these elements was large, but in other locations, the depletion was small implying that manganese or molybdenum depletion was not a necessary feature for the formation of the white-bands. No significant differences in the levels of silicon or vanadium between the white-band and the regions surrounding them were observed (Figure 4.38d and 4.38e).

Comparing the composition to the volume fraction of carbide precipitates at each of the twelve white-band locations (Figure 4.28), the chromium distribution in Figure 4.38a showed a good correlation; it can be observed that the largest difference in chromium concentration correlated with the white-band showing the most severe depletion of carbide precipitates (location 5). White-band locations 5 and 9 with lowest chromium contents were also the two locations with lowest volume fractions of carbide precipitates. In addition, the hardness of each white-band was plotted against its corresponding difference of chromium content inside and outside the white-band, as shown in Figure 4.39. It can be seen that white-bands with lower levels of chromium depletion normally exhibited higher hardness. However, there is a significant degree of scatter in the data.

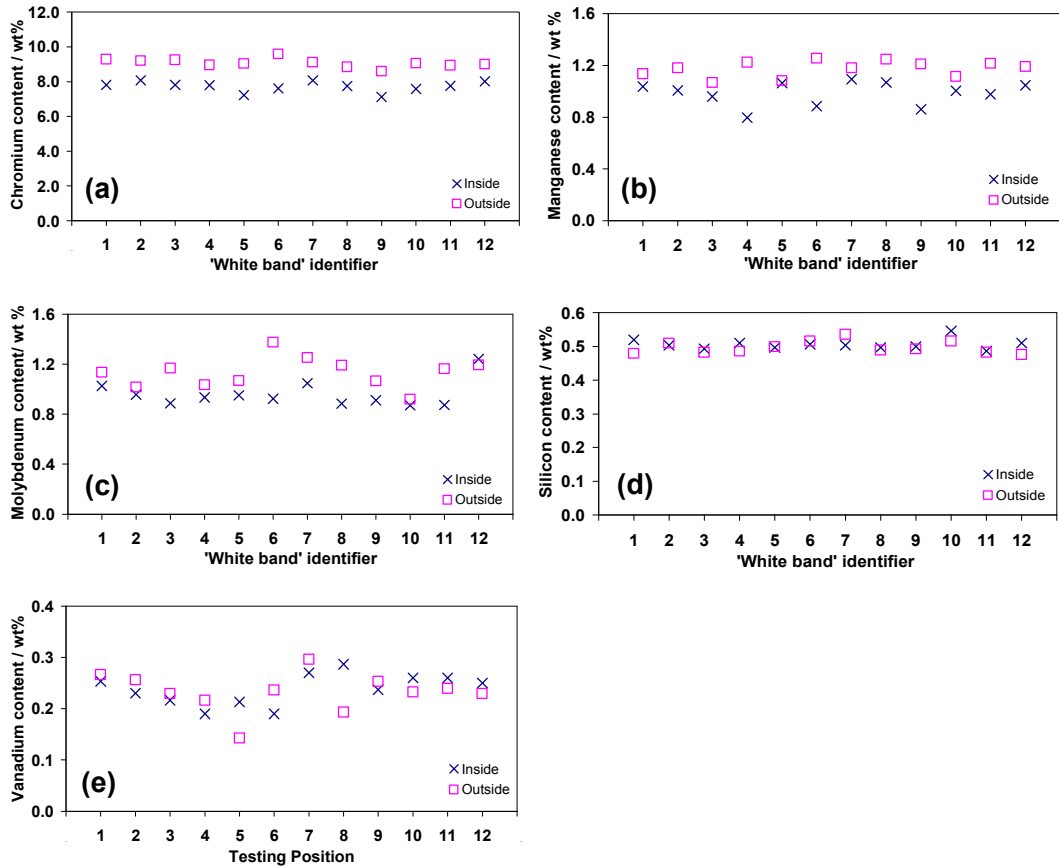


Figure 4.38 Comparison of chemical composition inside and outside the white-bands in P91 weld metal creep tested at 650°C and 90 MPa (white-band locations as indicated in Figure 4.27): (a) chromium; (b) manganese; (c) molybdenum; (d) silicon; (e) vanadium

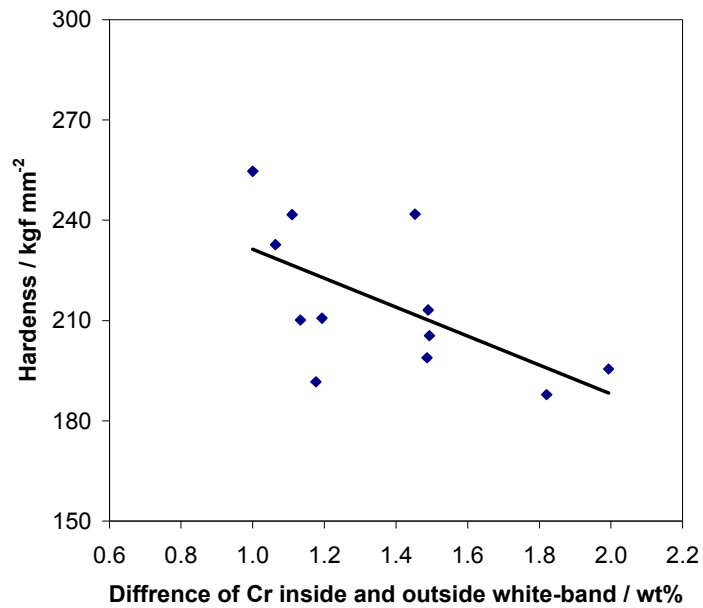


Figure 4.39 Correlation between hardness and difference of chromium inside and outside the white-bands in P91 weld metal creep tested at 650°C and 90 MPa (Specimen F90-90)

4.3.4.2 LIBS results

Due to the limitation of EDX analysis for measurement of carbon content at such low levels (<0.1 wt%), LIBS was introduced to obtain the element concentration maps of carbon along with the other alloying elements. Figure 4.40 shows an etched micrograph of a creep tested sample with the area over which the LIBS analysis was conducted (a rectangle of 12 mm × 5 mm) marked. As can be seen, several white-bands were included in this region. Figure 4.41a to 4.41e are the LIBS element concentration maps of carbon, chromium, manganese, molybdenum and nickel respectively. In addition, the concentration of the elements along a single line which traversed three of the distinct white-bands was extracted from the maps, as shown in Figure 4.42. Here, the position of the line of interest is shown in Figure 4.42a, with the concentration of the elements along that line shown in the later parts of the same figure. The depletion of carbon in the regions of the white-bands is very clear from the LIBS map (Figure 4.41a). The distribution of the carbon depleted bands and extent of depletion match exactly

with the location of the white-bands observed in the optical micrograph shown in Figure 4.40. The most distinct white-bands observed in Figure 4.40 are seen to have the most severe depletion of carbon in Figure 4.41a. The line scan of the carbon concentration (Figure 4.42b) indicated that in the most distinct white-bands, the carbon concentration can be as low as 0.02 wt%. Similarly, chromium and manganese also exhibit a clear correlation between their depletion and the position of the white-bands (cf. Figure 4.41b and 4.41c with Figure 4.40) with the most distinct white-bands again exhibiting significant depletion of chromium and manganese. Similarly to carbon, the line scan of the chromium (Figure 4.42c) and manganese (Figure 4.42d) concentrations have three regions with low element concentrations as marked, which are the three white-band positions. Molybdenum did not show any noticeable depletion in either the concentration map (Figure 4.41d) or the line scan (Figure 4.42e). For nickel, a very slight depletion in nickel at the locations corresponding to the white-bands was observed in Figure 4.41e; however, this depletion could not be clearly distinguished in the line scan (Figure 4.42f). It has also been observed that the LIBS data for each element (Figure 4.41 and 4.42) are generally consistent with the EDX data presented in Figure 4.37 and 4.38.

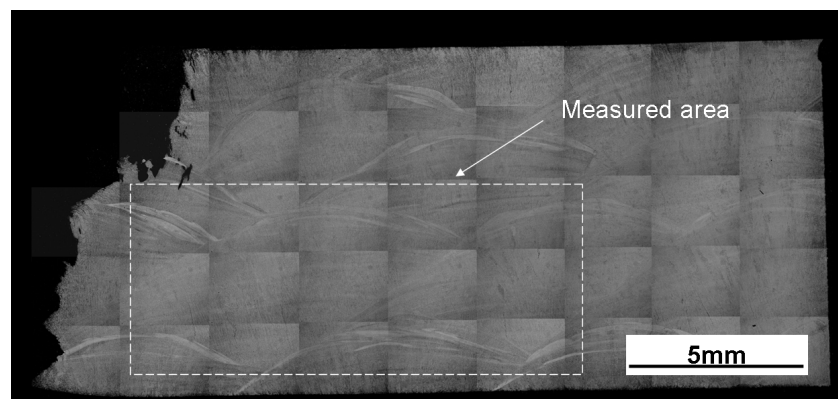


Figure 4.40 Microstructural montage of creep tested P91 weld metal F90-90 (650°C and 90 MPa) indicating area of LIBS measurement

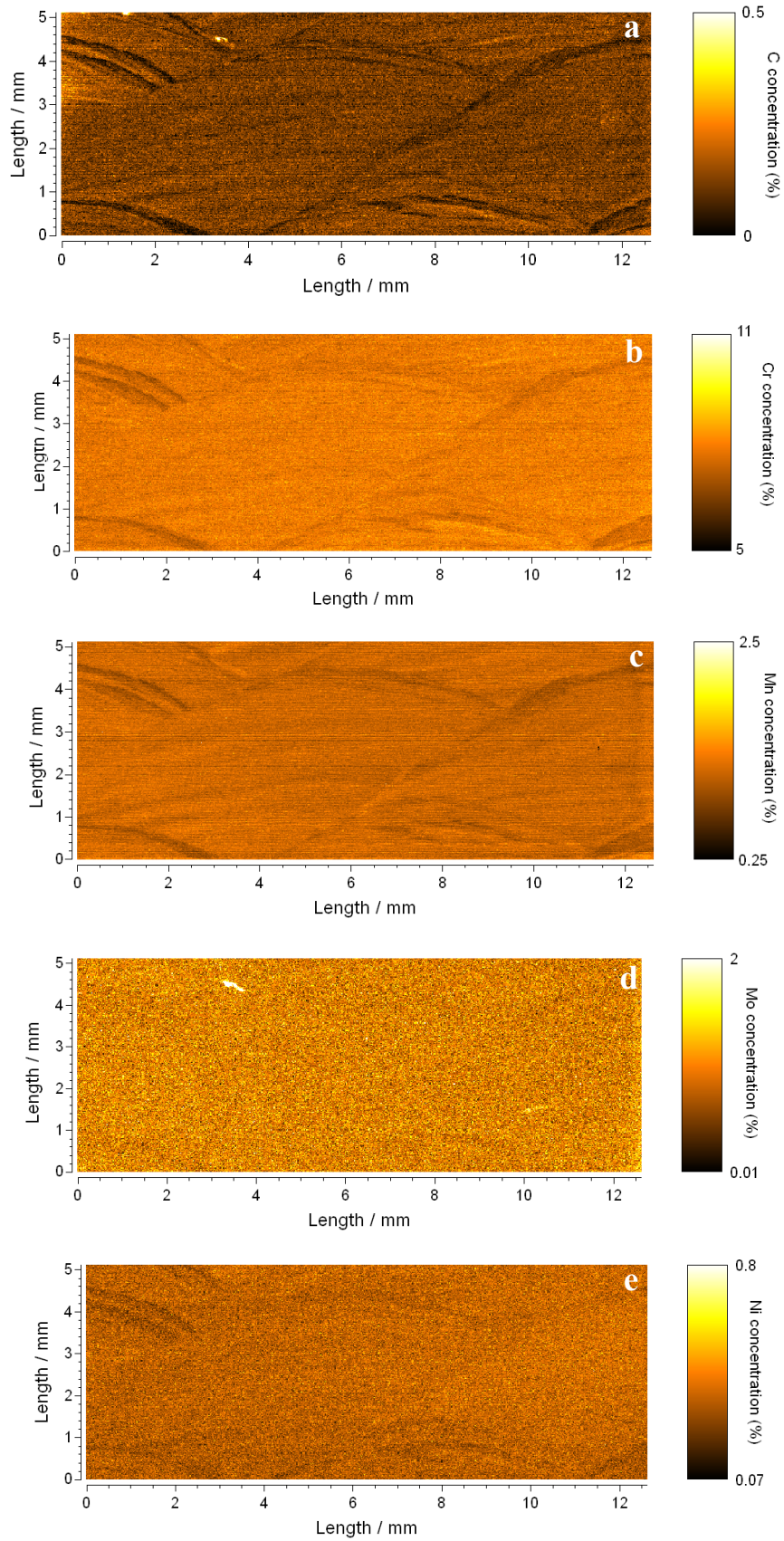


Figure 4.41 LIBS element concentration maps on creep tested P91 weld metal F90-90: (a) Carbon; (b) Chromium; (c) Manganese; (d) Molybdenum; (e) Nickel

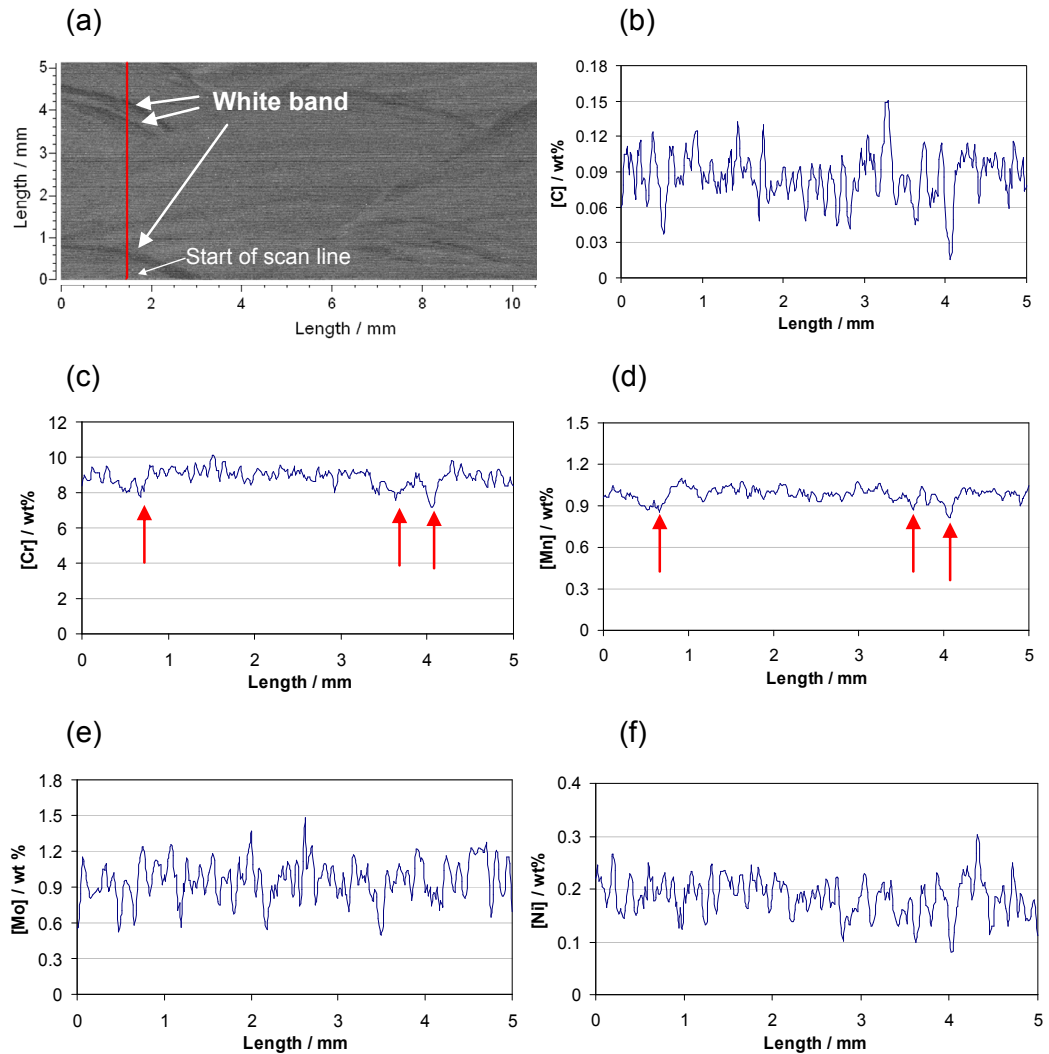


Figure 4.42 LIBS line scan of element concentration across white-bands in creep tested P91 weld metal F90-90: (a) Line-scan position indicated on grey Mn map; (b) Carbon; (c) Chromium; (d) Manganese; (e) Molybdenum; (f) Nickel

4.3.5 Development of white-bands by ageing of as-welded P91 weld metal

The full characterisation of white-bands has been carried out on creep tested P91 weld metal. Although the features of the white-band have been studied, the mechanism of white-band formation has not been fully understood. Accordingly, an as-welded P91 weld metal was examined in an attempt to trace the origin of white-band formation.

The as-welded P91 weld metal examined was extracted from a P91 pipe weld by deep hole drilling (DHD). The pipe weld was produced by the manual metal arc welding method using the same P91 Type M welding rod same as used for the deposition of weld pad studied in the rest of this work. As shown in the etched micrograph of the as-welded P91 weld metal in Figure 4.43a, this specimen covers both the parent metal and the multi-pass weld metal. The area over which the LIBS analysis was conducted is indicated (a rectangle of 22 mm × 3.5 mm marked). As can be seen, no evidence of white-bands was observed on the etched micrograph of the as-welded sample (Figure 4.43a). Figure 4.43b to 4.43f are the LIBS element concentration maps of carbon, chromium, manganese, molybdenum and nickel, respectively. At the as-welded stage, carbon was evenly distributed all over the sample from the LIBS map (Figure 4.43b). However, chromium and manganese exhibit distinct depletion along the bands at or near the fusion boundaries (Figure 4.43c and 4.43d), where the white-bands were normally observed on creep tested samples. Molybdenum did not exhibit any noticeable depletion in its LIBS concentration map (Figure 4.43e). For nickel, only slight depletion was observed at the locations corresponding to the chromium and manganese depletion (Figure 4.43f).

It can be seen that the depletion of chromium, manganese and nickel existed after the welding process, but that carbon is uniformly distributed at this stage. The depletion of carbon observed following creep testing occurred during the long-term heat exposure at those locations with the depletion of alloying elements. In light of this hypothesis, the as-welded P91 weld metal sample was heat treated at 760°C for 3 hours followed by the thermal exposure at 650°C for 30 hours, with the expectation of observing white-band development at the locations of alloying element depletion.

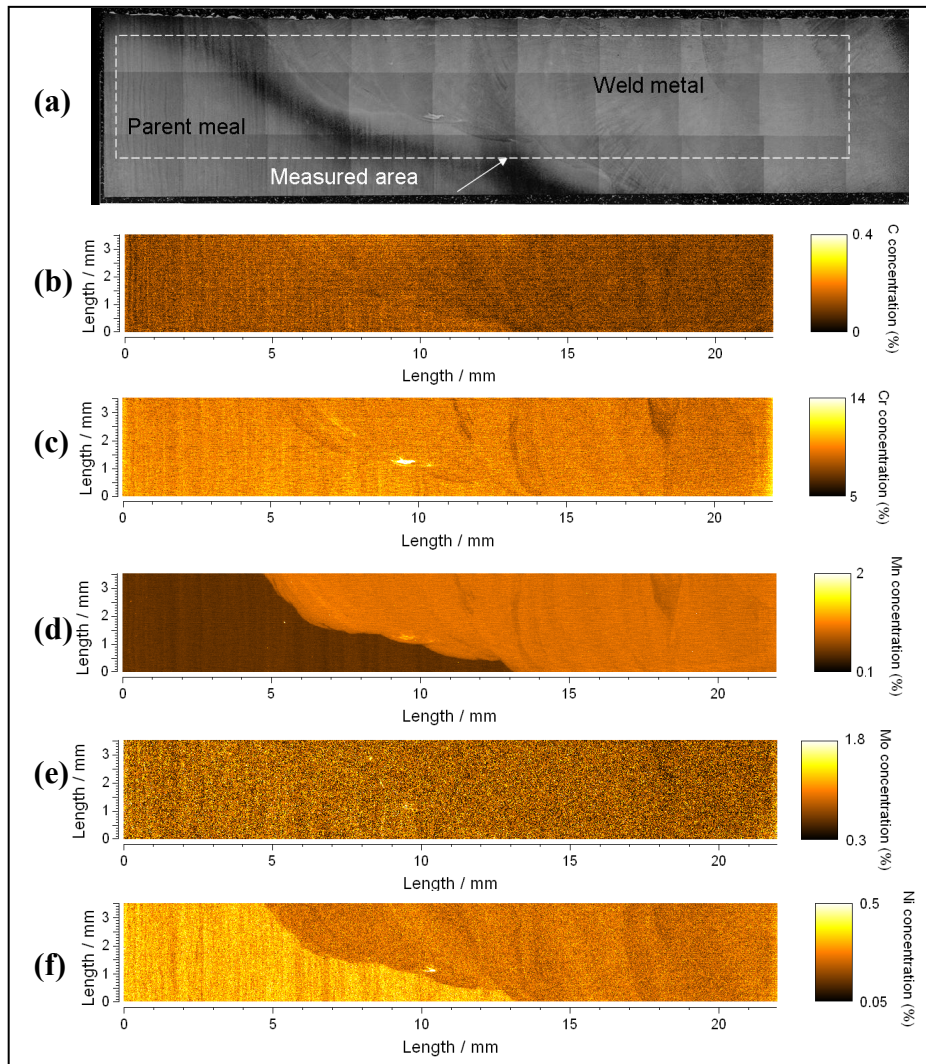


Figure 4.43 Element mapping of as-welded P91 weld metal by LIBS

The results of development of white-band during heat treatment of P91 weld metal are shown in Figure 4.44. Figure 4.44a is the LIBS chromium concentration mapping of the as-welded sample showing the locations of chromium depletion. Figure 4.44b is the optical micrograph montage of this sample after heat treatment. The formation of light etched white-bands at the locations of chromium depletion is clear. Figure 4.44c to 4.44e are the optical micrographs of the white-band locations indicated in Figure 4.44b at higher magnification. This test has confirmed that the localised depletion of alloying elements following the welding process can lead to the depletion of carbon during long-term heat exposure.

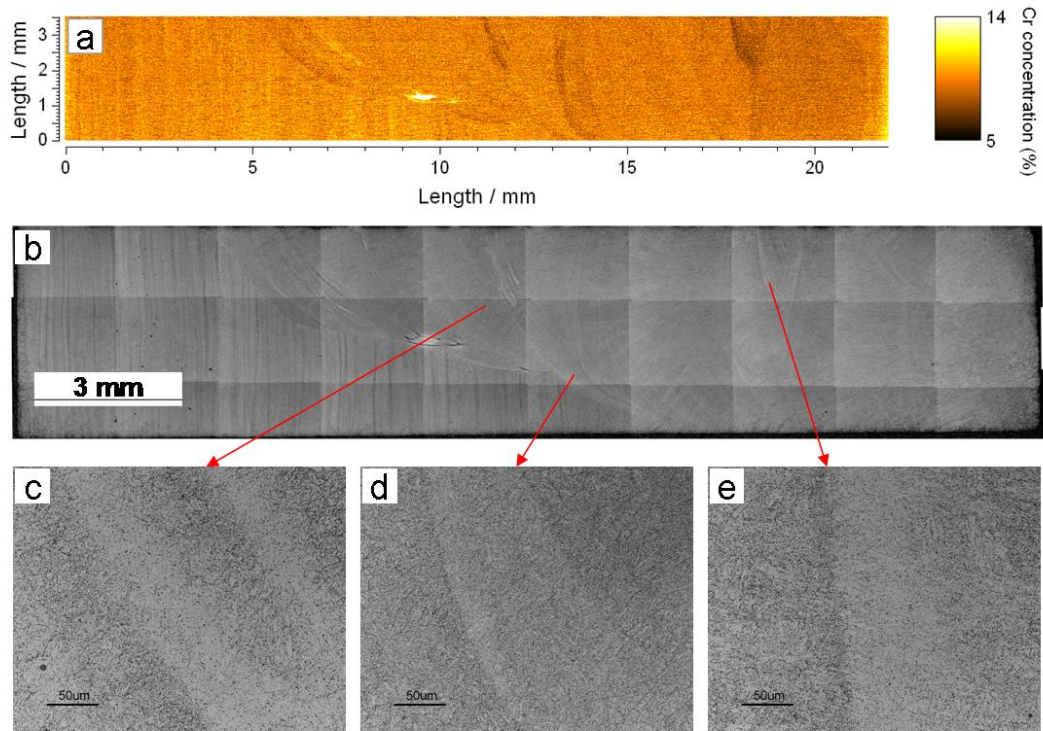


Figure 4.44 Development of white bands during heat exposure of P91 weld metal (heat treated at 760°C for 3 hours followed by heat exposure at 650°C for 30 hours): (a) LIBS chromium concentration map of as-welded P91 weld metal showing localised depletion of chromium; (b) optical micrograph montage of P91 weld metal after heat treatment; (c), (d) and (e) optical micrograph of white-bands

4.3.6. Mechanism of white-band formation

The investigation of the white-band and its formation has thus indicated a two stages process: the inhomogeneity of alloying element distribution in P91 weld metal following welding and the carbon diffusion out of the alloy-depleted regions during heat exposure. A brief discussion on the mechanism of white-band formation is given here regarding these two stages to form the basis of Thermo-Calc modelling of white-band formation in Chapter 5. The detailed discussion will be presented in Chapter 6.

The first stage is dependent upon the melting and solidification process. One possible explanation for the inhomogeneity of the alloying element distribution

following the welding process is the solution partition at the solid-liquid interface. Taking k_0 as the equilibrium partition coefficient, an alloy with nominal solute composition C_0 will begin to solidify at T_L with the formation of the first solid with the composition of k_0C_0 , as shown in Figure 2.17. A solute depleted band may then form at the weld bead boundaries. The possibility of poor mixing of liquid weld metal during the welding process may also contribute to the localised depletion of alloying elements (Savage et al., 1976; Allen et al., 2005).

The second stage is dependent upon the carbon diffusion out of the region with solute depletion. Carbon diffusion driven by a carbon activity gradient has been reported frequently in welds between dissimilar steels (Laha et al., 2001a, Laha et al., 2001b, Kasatkin and Tsaryuk, 1967, Foret et al., 2006, Foret et al., 2001) where the presence of higher chromium leads to a significant reduction in the activity of carbon, and thus carbon migration down the activity gradient towards the high chromium side has been observed during high temperature exposure of dissimilar welds and has resulted in a carbon-depleted zone on the low chromium side and carbon-rich zone on the high chromium side. The same mechanism can be applied to the case of the white-bands in the current work, where localised depletion of chromium will cause the migration of carbon during heat exposure.

4.4 CHARACTERISATION OF THE P91 TIG WELD METAL

In this work, white-bands have been frequently observed in the creep tested P91 weld metal which was made by manual metal arc (MMA) welding process. Based on the characterisation results, it was seen that white-band formation depends upon the formation of alloy-depleted regions during weld solidification and the carbon diffusion during heat exposure. However, the factors which drove the inhomogeneity in alloying element distribution are not well understood. To investigate this further, simulation P91 welds were made by the melting and resolidification of P91 parent metal using TIG welding, where no filler material was added. These welds were examined both in the as-welded condition and in the heat treated condition.

Two P91 TIG welds were made with a welding speed of 0.08 m/min and 0.04 m/min respectively. Both of them were welded with argon protection in an attempt to control the effect of oxidation. The microstructure of the P91 TIG welds in the as-welded condition is shown in Figure 4.45 (welding speed: 0.08 m/min) and Figure 4.46 (welding speed: 0.04 m/min).

There is no obvious difference in the microstructure between the P91 TIG weld with different welding speeds except that the weld beads in the weld with slower welding speed were deeper. In both cases, significant numbers of light-etched large δ -ferrite areas were observed at the fusion boundaries of the weld, which forms by the rapid solidification and cooling of the weld metal. Although in the Schaeffler diagram (Figure 2.4), the P91 composition lies within the martensite stability field, it is very close to the martensite + ferrite field. There is a high potential for the formation of ferrite, which is very sensitive to slight compositional variations reflected in chromium and nickel equivalent values and also sensitive to heat input. It was also noticed that the fusion boundary of the first bead had much less δ -ferrite, since it was reheated by the laying down of the second bead.

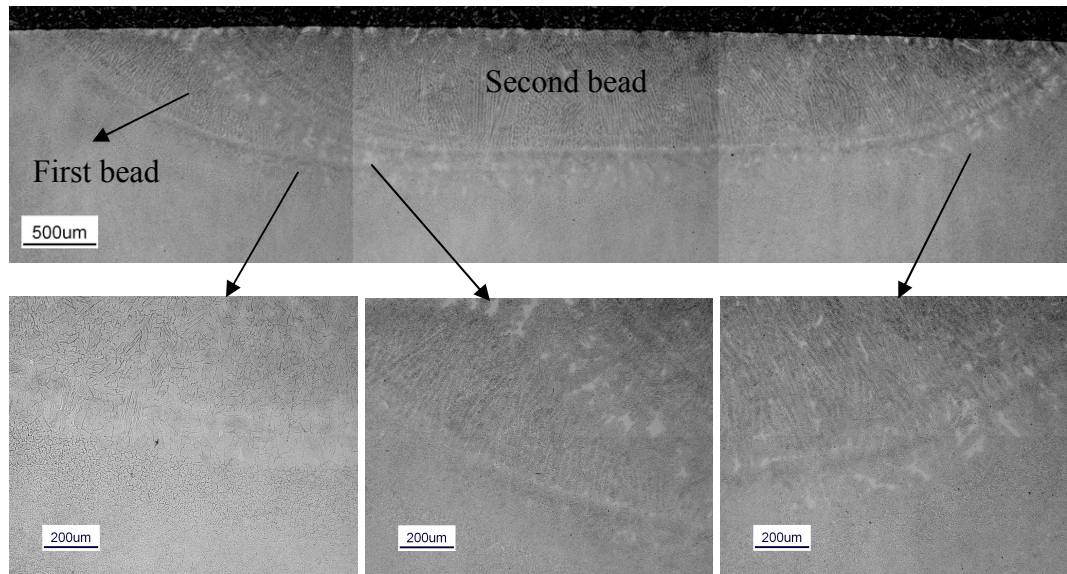


Figure 4.45 Optical micrographs of as-welded P91 TIG weld with a weld speed of 0.08 m/min

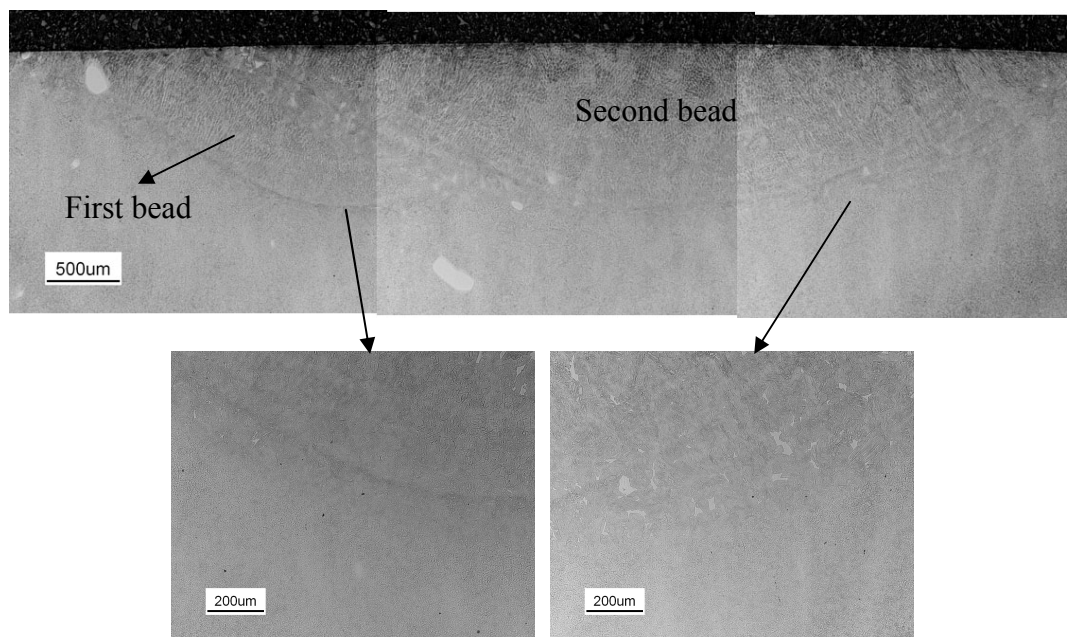


Figure 4.46 Optical micrographs of as-welded P91 TIG weld with a weld speed of 0.04 m/min

Figure 4.47 shows an optical micrograph of the fusion boundary in an as-welded P91 TIG weld, with an indication of the different microstructural zones. The region with much δ -ferrite is at the fusion boundary within the weld metal. It is approximately 200 μm wide. The SEM SE images of δ -ferrite in this region are shown in Figure 4.48. It can be seen that δ -ferrite is up to 50 μm in length, and is totally free of carbides.

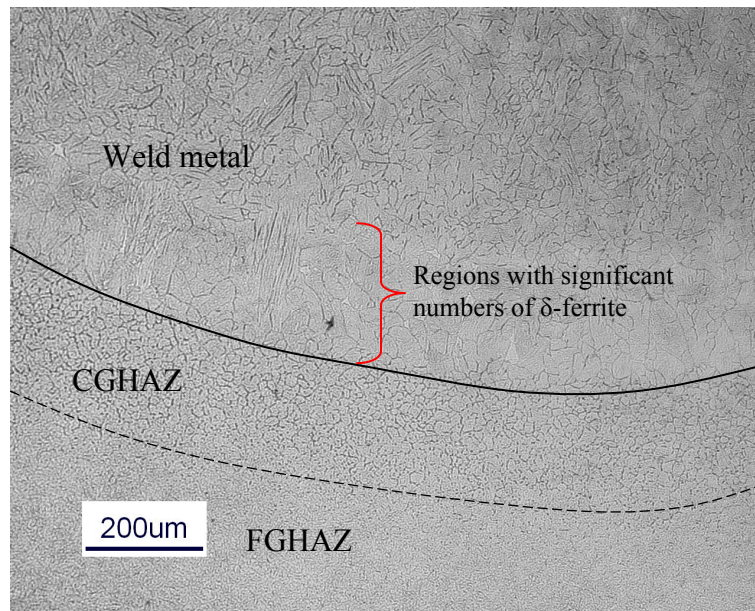


Figure 4.47 Optical micrograph of the fusion boundary in as-welded P91 TIG weld

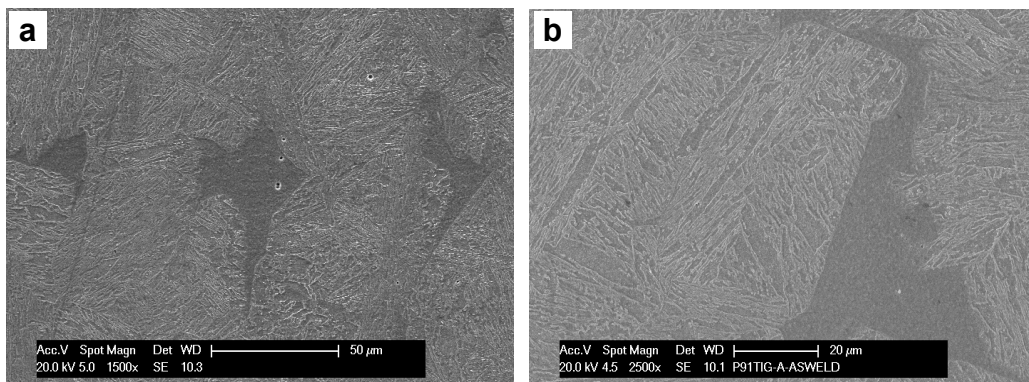


Figure 4.48 Large δ -ferrite phases free of carbides at fusion boundary

The element distribution across the fusion boundary was measured by EDX. The results are shown in Figure 4.49, where a very slight reduction of chromium concentration (approximately 0.3% wt) in regions with significant amount of δ -ferrite can be seen. However, the depletion of chromium is much less than that observed in the white-bands of P91 MMA weld metal.

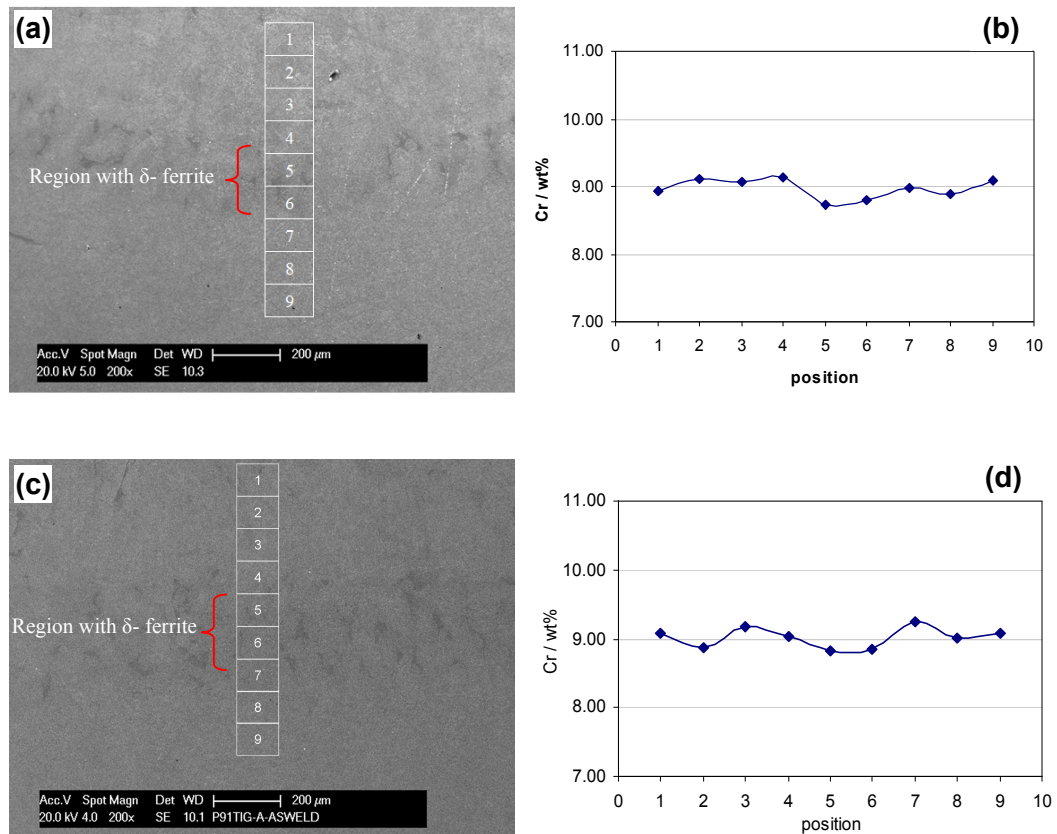


Figure 4.49 EDX analysis of chromium concentration across the fusion boundary of TIG P91 welds at as-weld condition

The P91 TIG weld was heat treated at 650°C and 760°C for 30 hours respectively to investigate the microstructural development, especially at the fusion boundaries. The optical micrograph montages of P91 TIG welds with different welding and heat treatment conditions are shown in Figure 4.50. In all the weld samples, fusion boundaries with numbers of δ -ferrite areas are seen as light-etched bands after heat treatment. The amount of δ -ferrite reduced compared to the as-welded

samples. The width of the light-etched bands is larger in the weld with lower welding speed.

Figure 4.51 shows the detailed optical micrographs and SEM SE images of the fusion boundary region, where the grain growth and the depletion of carbides due to heat treatment can be seen compared to the as-welded samples. Figure 4.52 shows a comparison of the amount and size of carbide precipitates in the fusion boundary and the bulk weld in the P91 TIG welds with different welding conditions and heat treatment conditions. The volume fraction of carbides under each condition was measured using Image J software. Under the same heat treatment condition, the carbide precipitates are coarser in the weld which was welded at a lower welding speed. Under the same welding speed, the number of the carbide precipitates is slightly less and the size of the carbide precipitates is larger with increasing heat treatment temperature. In all welding and heat treatment conditions, the light-etched fusion boundary regions contain slightly lower volume fractions of carbide precipitates compared to the bulk weld, which suggested the depletion of carbides precipitates at fusion boundary. However, the level of carbide depletion (to a volume fraction of approximately 0.8%) in the P91 TIG weld is much lower than that observed in the white-bands (to a volume fraction of 1%) of creep tested MMA P91 weld metal.

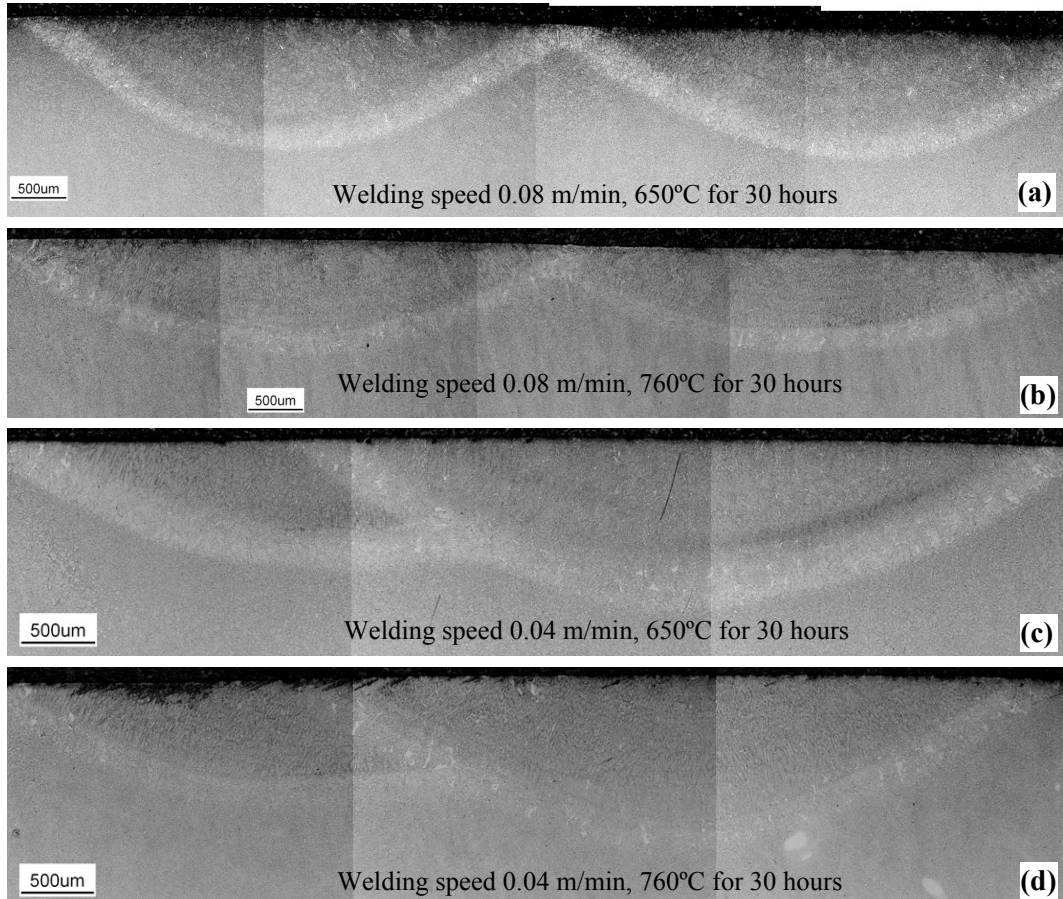


Figure 4.50 Optical micrograph montages of P91 TIG weld after heat treatment: (a) welding speed: 0.08 m/min, heat treatment at 650°C for 30 hours; (b) welding speed: 0.08 m/min, heat treatment at 760°C for 30 hours; (c) welding speed: 0.04 m/min, heat treatment at 650°C for 30 hours; (d) welding speed: 0.04 m/min, heat treatment at 760°C for 30 hours

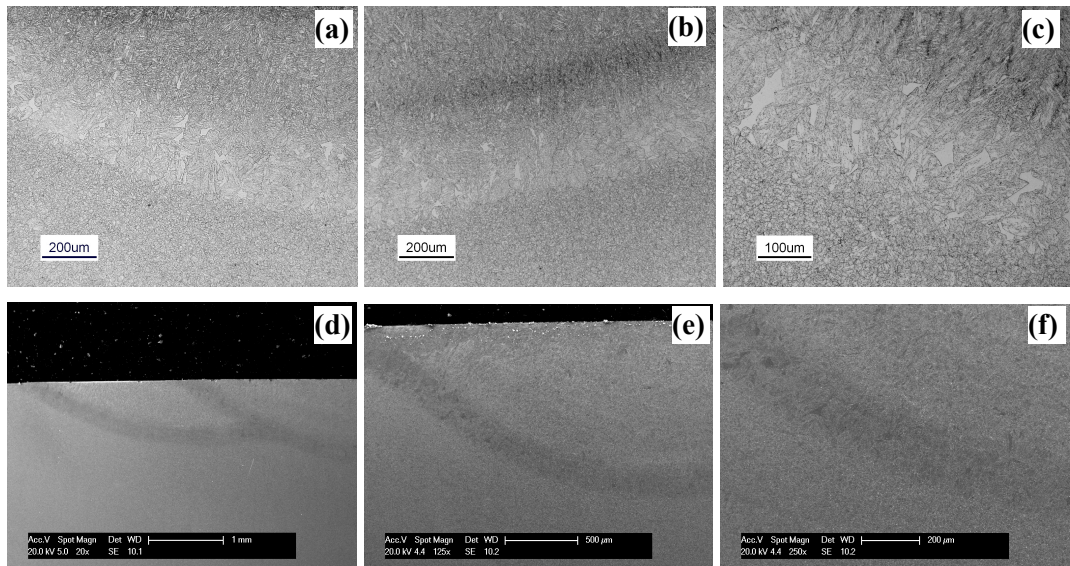


Figure 4.51 Optical micrographs (a, b and c) and SEM SE images (d, e and f) of fusion boundaries in P91 TIG weld after heat treatment.

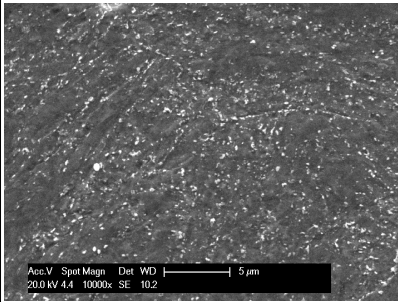
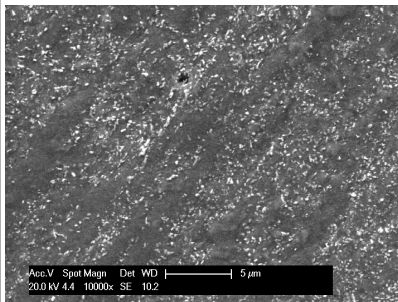
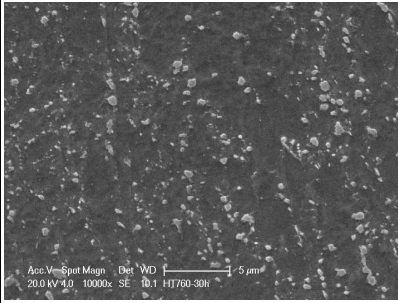
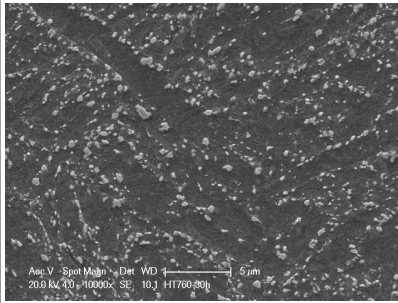
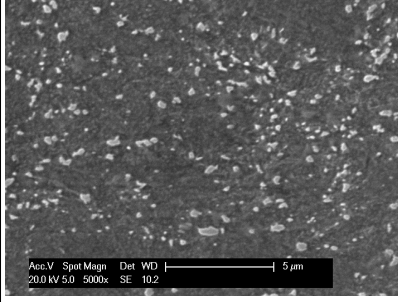
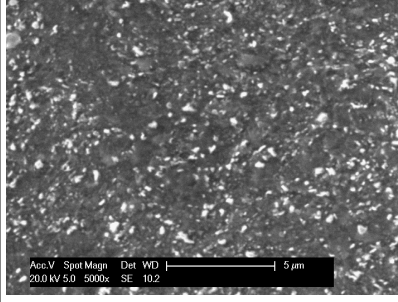
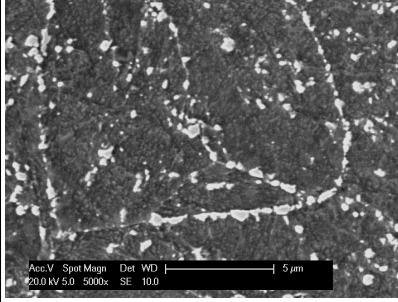
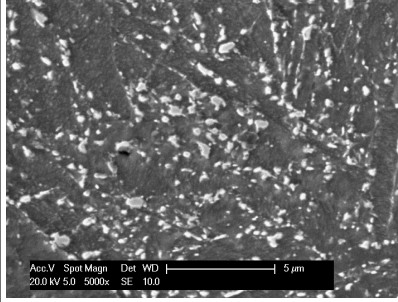
Welding speed	Heat treatment	Fusion boundary	Bulk weld
0.08 m/min	650°C 30 hours	 <p>Vol. fraction of $M_{23}C_6$ carbides: 1.7%</p>	 <p>Vol. fraction of $M_{23}C_6$ carbides: 2.7%</p>
0.08 m/min	760°C 30 hours	 <p>Vol. fraction of $M_{23}C_6$ carbides: 2.6%</p>	 <p>Vol. fraction of $M_{23}C_6$ carbides: 3.5%</p>
0.04 m/min	650°C 30 hours	 <p>Vol. fraction of $M_{23}C_6$ carbides: 2.2%</p>	 <p>Vol. fraction of $M_{23}C_6$ carbides: 3.1%</p>
0.04 m/min	760°C 30 hours	 <p>Vol. fraction of $M_{23}C_6$ carbides: 3.4%</p>	 <p>Vol. fraction of $M_{23}C_6$ carbides: 4.0%</p>

Figure 4.52 Comparison of carbide precipitates between fusion boundary and bulk weld of P91 TIG weld with different welding and heat treatment conditions (the volume fraction of carbide precipitates was measured using Image J software)

Chapter 5

Modelling of white-band formation in P91 weld metal

The modelling work aimed to produce insight into the formation of the white-bands. Experiments have indicated that the formation of white-bands depends upon two steps according to the results: (i) formation of inhomogeneity in the alloying elements; this may be due to solute partition at the bead boundary during the welding solidification; (ii) carbon diffusion out of the regions with depleted alloying elements during thermal exposure. As such, the modelling work has focused on the examination of solidification phases in the weld and their composition, and on the carbon activity as a function of chemical compositions. The modelling was carried out using the Thermo-Calc TCW4 (base on the CALPHAD method) with TCFE5 Steel and Fe-alloy Database.

The chemical compositions of P91 bulk weld metal and white-band materials used in the model were based on the measurement using EDX at the twelve white-band locations of one creep tested sample, as shown in Table 5.1. The levels of other elements such as niobium and aluminium were too low to detect. Since the composition used in the model needs to be the composition in the as-welded state, based on the experimental results, it was assumed that the chemical composition of the as-welded bulk weld is same as that of post-creep tested weld material, and that during the heat exposure only carbon diffusion occurred to any extent. Hence, the chemical composition of P91 bulk weld and white-bands used in modelling is shown as in Table 5.2. The percentage of reduction of each element is also listed, showing that chromium, manganese and molybdenum have the most significant (and similar) levels of reduction in the white-band region compared to that in the bulk weld.

	Bulk welds	white-bands
C*	0.098	N/A*
Cr	9.09	7.72
Mn	1.18	0.98
Mo	1.13	0.96
V	0.23	0.24
Ni	0.27	0.29
Si	0.5	0.51

Table 5.1 Average element composition of bulk weld and white-band of P91 creep tested sample using EDX analysis (*carbon content of bulk weld is taken from Table 3.1 since it cannot be measured using EDX)

	Bulk weld	white-bands (as-welded)	Percentage difference
C	(M2) 0.098	(A) 0.098	0.0%
Cr	(M1) 9.09	(M1) 7.72	-15.1%
Mn	(M1) 1.18	(M1) 0.98	-16.9%
Mo	(M1) 1.13	(M1) 0.96	-15.0%
V	(M1) 0.23	(M1) 0.24	4.3%
Nb	(M2) 0.08	(A) 0.08	0.0%
Ni	(M1) 0.27	(M1) 0.29	7.4%
Al	(M2) 0.01	(A) 0.01	0.0%
Si	(M1) 0.50	(M1) 0.51	2.0%
N	(M2) 0.046	(A) 0.046	0.0%

M1: Values measured by EDX

M2: Values taken from Table 3.1 since they are too low to be measured by EDX

A: The composition of these elements in as-welded white-band regions are assumed to be same as those of bulk weld since it was not possible to measure them using EDX

Table 5.2 Chemical composition of P91 bulk weld and white-band for Thermo-Calc modelling

5.1 MODELLING OF SOLUTE PARTITION DURING P91 WELD SOLIDIFICATION

5.1.1 P91 Phase content at different temperatures

The fraction of phases at all temperatures was calculated for P91 weld metal using the chemical composition of bulk weld in Table 5.2. Variables input included the chemical composition and pressure. The mole fraction of each phase was plotted against temperature (0 to 2000°C) in Figure 5.1. It can be seen that the liquid metal started to solidify at 1498°C with the formation of BCC_A2, which is the high temperature δ -ferrite (bcc). At 1433°C, FCC_A1#1 (austenite γ , fcc) starts to form with the complete solidification of liquid metal at 1430°C, and the high temperature δ -ferrite (bcc) being completely transformed to austenite at 1241°C. Austenite transforms to low temperature α -ferrite from 844°C. $M_{23}C_6$ carbides start to precipitate at 870°C.

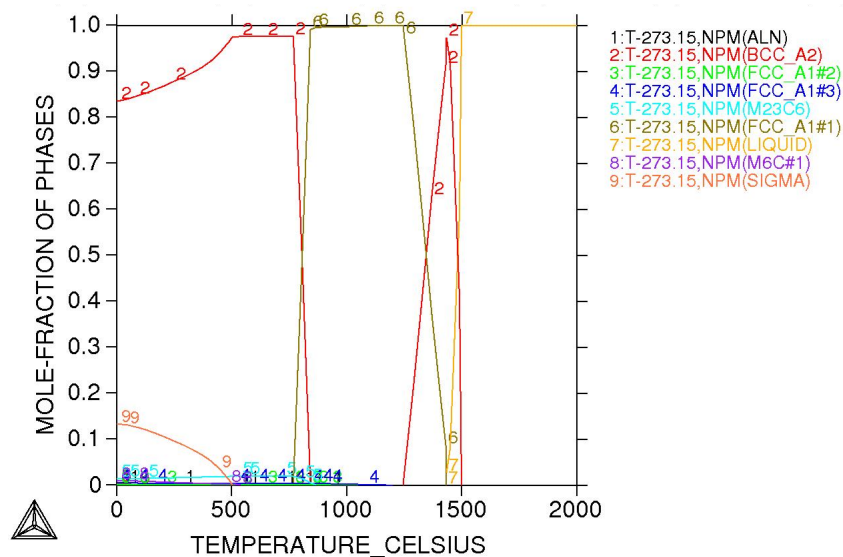


Figure 5.1 Mole-fraction of phases of P91 weld metal against temperature

5.1.2 Solute partition during weld solidification

Based on Figure 5.1 and the isopleths phase diagram in Fig 2.5, it can be known that for P91 weld metal, δ -ferrite is the first solid phase formed during solidification.

The composition of first ferrite solidified will have the lowest solute content due to the solute partition, which may lead to inhomogeneity of the weld composition. The composition of the first δ -ferrite formed was calculated and is shown in Table 5.3. The possibility of solidification to metastable austenite directly has also been considered for the P91 weld metal, since it has been argued that this can happen if the cooling rate is large enough, even when δ -ferrite is the thermodynamically favoured phase in low-alloy steel, and is especially likely when the partition coefficient k is closer to unity for solidification to austenite (Fredriksson, 1976). In addition, solidification to austenite as the initial phase becomes more feasible since the steel is alloyed with austenite stabilising elements, until the austenite eventually becomes the thermodynamically stable phase (Bhadeshia and Svensson, 1993). So the modelling has also been carried out with the BCC_A2 phase being made dormant, which means that BCC_A2 is not considered in the calculation, and liquid metal solidifies directly to austenite as the primary phase. The chemical composition of the first austenite solidified in this case is also listed in Table 5.3. Compared to the measured chemical composition of white-band, the modelled chemical composition of the first solid formed during solidification from liquid directly to δ -Fe showed generally much less depletion of alloying elements except in the cases of manganese and nickel. In the case of solidification from liquid directly into γ -Fe, the depletion of chromium and manganese in first solid formed is close to the measured values.

wt%	Bulk weld	White-band (as-weld)		
		Measured	Modelled	
			(L -> δ -Fe)	(L -> γ -Fe)
C*	0.098	0.098	0.098	0.098
Cr	9.09	7.72	8.664	7.732
Mn	1.18	0.98	0.870	0.940
Mo	1.13	0.96	0.972	0.747
V	0.23	0.24	0.191	0.147
Nb	0.08	0.08	0.015	0.008
Ni	0.27	0.29	0.221	0.257
Al	0.01	0.01	0.012	0.012
Si	0.50	0.51	0.396	0.390
N*	0.046	0.046	0.046	0.046

Table 5.3 Experimental and modelling chemical composition of white-bands (*due to the back diffusion of carbon and nitrogen, they are considered to be uniform in the as-welded stage)

5.2 MODELLING OF CARBON DIFFUSION OUT OF THE WHITE-BAND REGIONS

5.2.1 Modelling strategies

Carbon diffusion driven by activity gradient has been reported frequently in the examination of welds between dissimilar steels, where it has been noticed that the presence of higher chromium leads to a significant reduction in the activity of carbon, thus forcing carbon migration down the activity gradient towards the high chromium side during high temperature exposure (Laha et al., 2001a, Laha et al., 2001b, Kasatkin and Tsaryuk, 1967, Foret et al., 2001, Foret et al., 2006).

This mechanism is also applicable to the case of white-band formation where there was a depletion in certain alloying elements (including chromium) as shown in Table 5.2. According to this mechanism of carbon diffusion, a model of carbon diffusion out of the white-bands can be set up as described in Figure 5.2. In the as-welded stage, it is assumed the carbon concentration is uniformly distributed, whilst carbon activity in white-bands is much higher than that in bulk weld due to its depletion in alloying elements. After long-term heat exposure, a uniform carbon activity will be achieved resulting from the carbon diffusion out of the white-bands. Since the width of the white-bands is very small (typically 50 to 200 μm) compared to the bulk weld, the eventual carbon activity in white-band can be assumed to be approximately same to the carbon activity in the bulk weld in the as-welded stage. Hence, there will be a limiting carbon concentration eventually in the white-bands to achieve the uniform carbon activity. Since a white-band is only 50 to 200 μm wide, to compensate the carbon loss, the limiting carbon concentration in white-band is expected to be much lower than that observed in the carbon-depleted zone of a dissimilar weld with similar differences in alloying element compositions.

With Thermo-Calc and TCFE5 Steel and Fe-alloy Database, it is possible to calculate the equilibrium status of a certain steel composition at a pre-defined temperature and pressure, including the carbon activity. The limiting carbon concentration of the white-band can be calculated by setting the carbon activity of white-band to be the same as that of the bulk weld. The equilibrium carbon

concentration resulting will be the limiting carbon concentration to achieve uniform carbon activity between the white-band and bulk weld. The equilibrium phase contents including the $M_{23}C_6$ carbides of white-band and bulk weld can also be obtained for the given conditions.

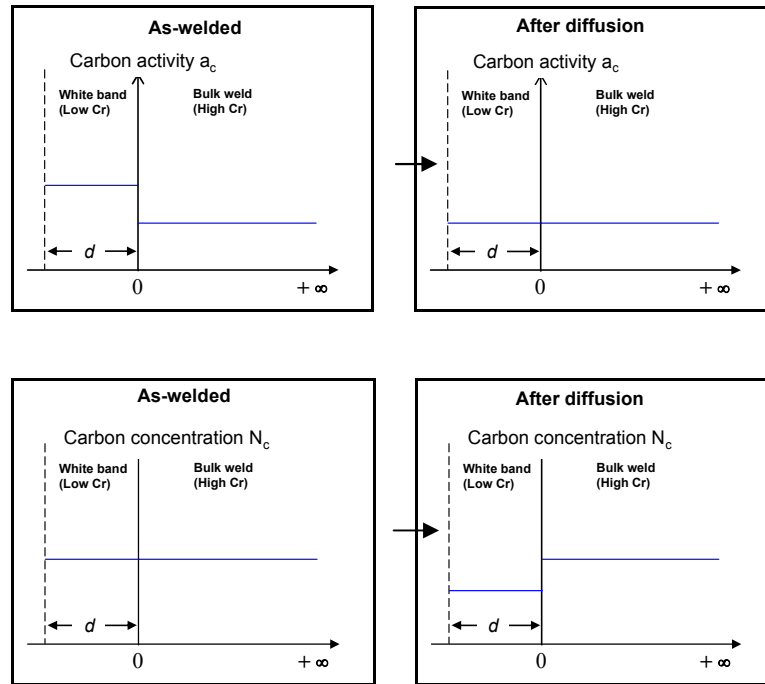


Figure 5.2 Modelling of carbon diffusion out of the white band

5.2.2 Carbon activity in P91 weld metal

The temperature dependence of carbon activity for the P91 bulk weld metal composition was modelled with Thermo-Calc. The plots of carbon activity against temperature for P91 steel on both a linear and logarithmic scale are shown in Figure 5.3a and 5.3b respectively. The discontinuities indicated (a, b, c and d) represent the phase transformations. At temperatures lower than 870°C (position a), α -ferrites are stable and carbon exists mostly in the form of $M_{23}C_6$ carbides since ferrite has very low carbon solubility. In this region, carbon activity increases with increasing temperature. However, when temperature increases, α -ferrite transform completely into austenite and $M_{23}C_6$ carbides dissolve completely. In this region, carbon activity reduced with increasing temperature. At 1241°C (position b), when austenite starts to transform into high temperature δ -ferrite, carbon activity increases again until the liquid metal forms (position c).

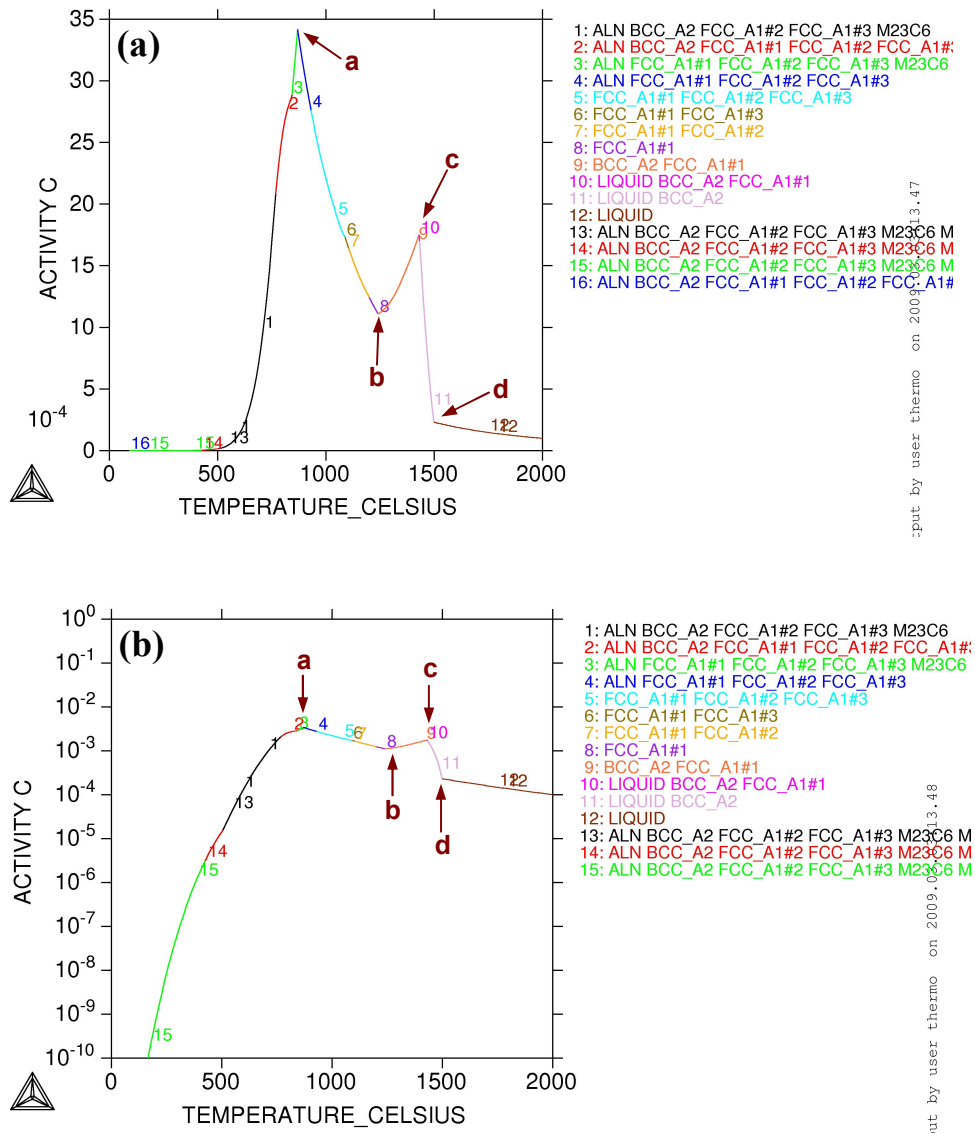


Figure 5.3 Temperature dependence of carbon activity for P91 weld metal obtained from Thermo-Calc modelling: (a) correlation between carbon activity and temperature; (b) correlation between logarithm of carbon activity and temperature

It has been noticed from Table 5.2 that chromium, molybdenum and manganese have the most significant levels of reduction in the white-band regions compared to that of bulk weld. The dependence of carbon activity on each of these elements has also been modelled for the P91 bulk weld metal composition with the single element variation in chromium or molybdenum or manganese. The plots of

logarithm of carbon activity against single variation in chromium or molybdenum and manganese at 650°C were shown in Figure 5.4.

Figure 5.4a indicates a strong dependence of carbon activity on chromium content. The carbon activities in the P91 materials with chromium only depleted to its white-band level (7.72 wt% Cr) and in the bulk weld metal (9.09 wt% Cr) at 650°C are also indicated in Figure 5.4a. With the depletion of chromium being only 1.37 wt%, the carbon activity in white-band increases to 1.5 times that of the carbon activity in the bulk weld. The dependence of carbon activity on molybdenum is shown in Figure 5.4b, which indicated that molybdenum content in P91 materials also affects the activity of carbon to some extent, but not as significantly as chromium. As indicated in Figure 5.4b, with the level of molybdenum reduction in white-band region being 0.17 wt%, the carbon activity increases to 1.1 times that of the carbon activity in the bulk weld. However, no evidence of significant dependence of carbon activity on manganese content was observed with manganese content ranging from 0 to 5 wt% (Figure 5.4c). These results indicated that the depletion of chromium and molybdenum, not manganese, in white-band can lead to a gradient of carbon activity, resulting in the carbon diffusion out of the white-bands.

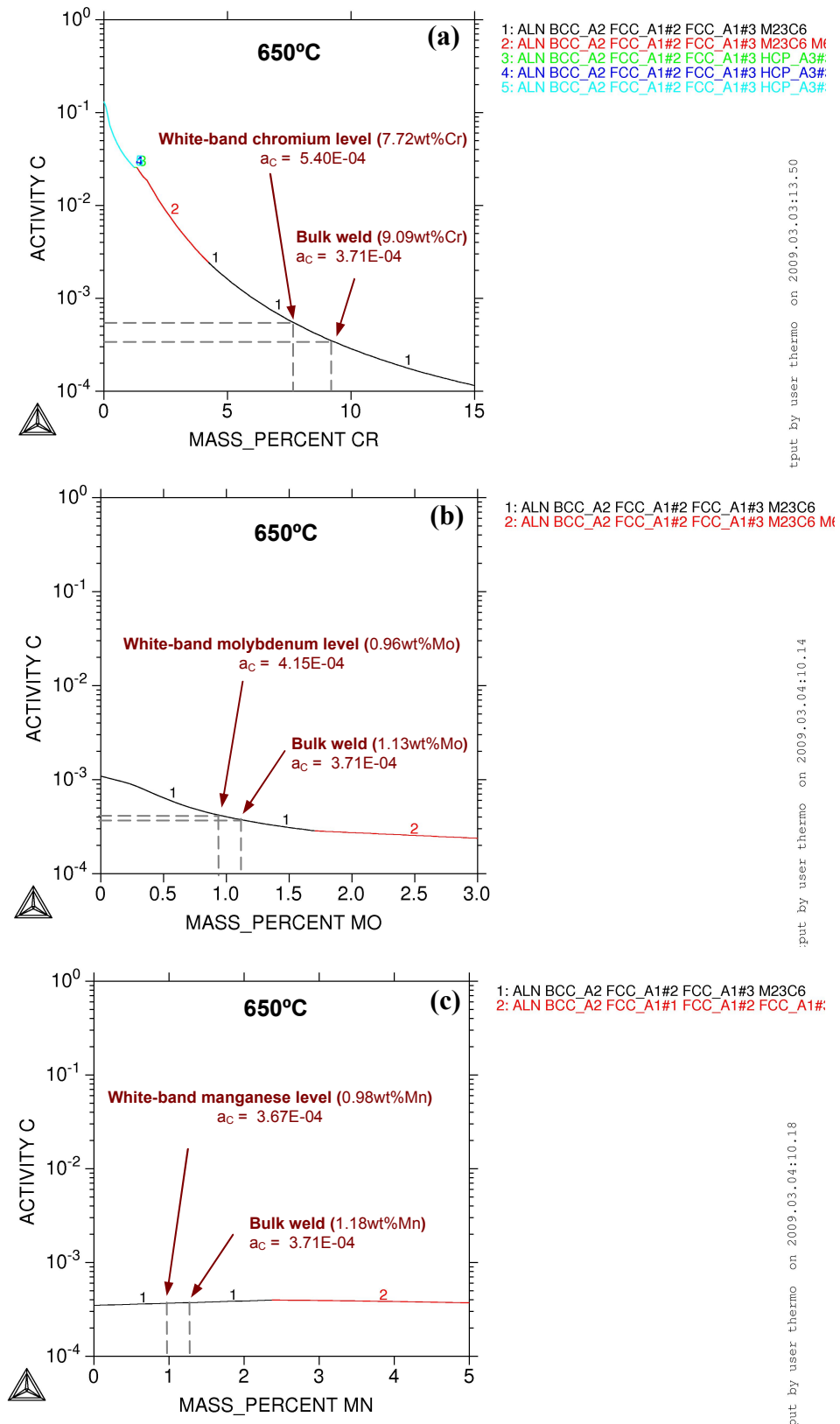


Figure 5.4 Dependence of carbon activity on single variation in (a) chromium content, (b) molybdenum content and (c) manganese content at 650°C for P91 weld metal bulk weld composition

5.2.3 Limiting carbon concentration in white-bands

It has been discussed that a limiting carbon concentration in the white-bands can be calculated with Thermo-Calc using the strategy of obtaining the uniform carbon activity between white-band materials and the bulk weld. The limiting carbon concentration in white-band regions (with as-welded white-band composition in Table 5.2) was calculated at various temperatures (550°C, 575°C, 600°C, 650°C, 700°C and 760°C) and the results are shown in Figure 5.5. With a starting carbon concentration of 0.098 wt% (the as-welded state), the limiting carbon concentration at all temperatures examined will eventually reduce to approximately 0.01 wt% in the white-band region after an extended-time thermal exposure. The results showed good correlation with the carbon concentration of the white-band region in creep tested samples measured by LIBS (< 0.01 wt%).

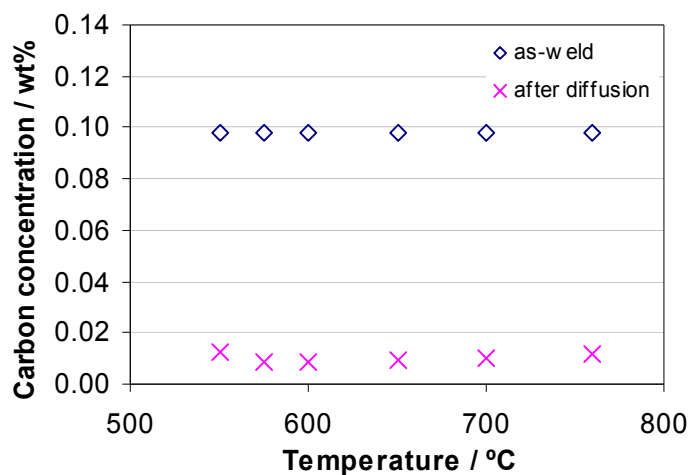


Figure 5.5 Limiting carbon concentrations in white-band at different temperatures obtained from Thermo-Calc modelling (using the as-welded white-band composition in Table 5.2)

Taking the measured composition of the as-welded white-band as 100% depletion of alloying elements (Table 5.2), the limiting carbon concentration in white-band was also calculated with various levels of depletion of alloying elements (25%, 50%, 75%, 100%, 125% and 150%) for 650°C, as shown in Figure 5.6. It was noted that with the depletion of alloying elements less than 100% (the

experimental value), the correlation between limiting carbon concentration and level of depletion is approximately linear. However, with the depletion of alloying elements greater than the experimental value (greater than 100%), the eventual limiting carbon concentration does not reduce any further.

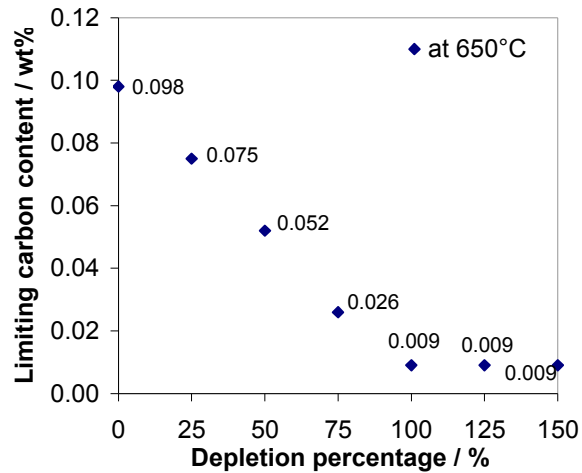


Figure 5.6 Dependence of limiting carbon content on the levels of depletion of alloying elements from Thermo-Calc modelling

5.2.4 Carbide precipitates

Carbide depletion is an important feature of the white-bands after heat exposure. The equilibrium phase contents in white-bands have been calculated using Thermo-Calc. As shown in Table 5.4, the equilibrium phase contents have been obtained using the measured white-band composition in the as-welded state in Table 5.2. It can be noticed that there are no significant changes of phases except $M_{23}C_6$ carbides in white-bands between the as-welded state and after diffusion. With 1.71 wt% of $M_{23}C_6$ in the white-band in the as-welded state, the depletion of carbon out of the white-band at 650°C will eventually result in a white-band being totally free of carbides to achieve uniform carbon activity. This is in accordance with the observation of carbide content in white-bands of creep tested P91 weld metal (Figure 4.26).

The dependence of phase contents on single depletion of Cr, Mn or Mo has also been investigated without any change in other elements but only the examined element. As shown in Table 5.4, the depletion of chromium only in white-bands

resulted in a significant depletion of $M_{23}C_6$ carbides to less than 10% of the $M_{23}C_6$ carbide content in the as-welded state, whilst depletion of molybdenum only also lead to the depletion of $M_{23}C_6$ carbides to 76% of that in the as-welded state. The depletion of manganese only did not cause any significant depletion of $M_{23}C_6$ carbides, or other phases. These results showed good correlation with the results of dependence of carbon activity on Cr, Mo and Mn (Figure 5.4), where depletion of alloying elements affecting carbon activity actually accounts for the depletion of carbon and carbides from the white-band region.

650°C		Equilibrium phase content / mass fraction					
		Steel matrix	$M_{23}C_6$	VN	NbC	AIN	
Measured composition	as-weld	9.80E-01	1.71E-02	2.27E-03	8.39E-04	1.04E-04	
	after diffusion	9.97E-01	0	2.27E-03	7.94E-04	1.00E-04	
Modelled	Only Cr depletion	as-weld	9.80E-01	1.72E-02	2.27E-03	8.32E-04	1.04E-04
		after diffusion	9.95E-01	1.66E-03	2.27E-03	7.95E-04	1.00E-04
	Only Mn depletion	as-weld	9.80E-01	1.73E-02	2.27E-03	7.96E-04	9.97E-05
		after diffusion	9.79E-01	1.77E-02	2.27E-03	7.97E-04	9.97E-05
	Only Mo depletion	as-weld	9.80E-01	1.72E-02	2.27E-03	8.08E-04	9.98E-05
		after diffusion	9.84E-01	1.31E-02	2.27E-03	7.97E-04	9.88E-05

Table 5.4 Equilibrium phase contents in white-bands obtained from Thermo-Calc modelling using experimental white-band composition and model compositions with single element depletion (Cr / Mn / Mo)

Similarly to Figure 5.6, the dependence of limiting $M_{23}C_6$ carbide content on the levels of depletion of alloying elements was also calculated and plotted in Figure 5.7. The correlation between limiting $M_{23}C_6$ carbide content and levels of depletion is linear with depletion less than 100% (i.e. less than the experimentally observed value), and the limiting $M_{23}C_6$ carbide content reached to 0 with 100% depletion and onwards. Compared to Figure 5.6, it indicates that the depletion of $M_{23}C_6$ carbides and the depletion of carbon are strongly linked.

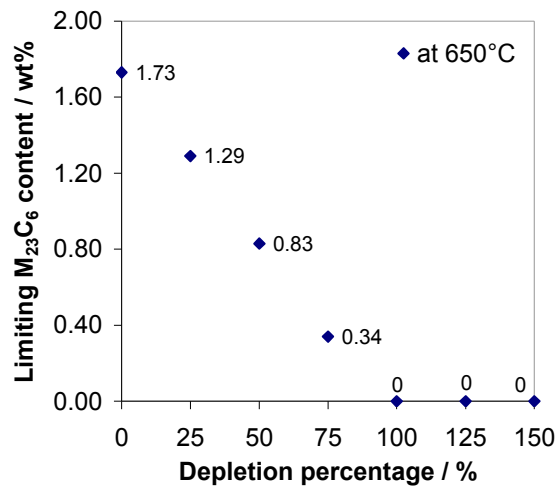


Figure 5.7 Dependence of limiting $M_{23}C_6$ carbide content on the levels of depletion of alloying elements from Thermo-Calc modelling

The equilibrium $M_{23}C_6$ carbide content has also been calculated using the modelled first-solidified composition in the cases of solidification from liquid to δ -Fe and γ -Fe (Table 5.3) at various temperatures. The comparison of results is shown in Table 5.5. Since the modelled first-solidified composition during solidification from liquid to γ -Fe showed similar level of Cr depletion and more significant Mo depletion compared to the measured white-band composition (carbon activity strongly depends on these two elements), both of them showed total depletion of $M_{23}C_6$ carbides in white-bands at all temperatures examined. In the case of solidification from liquid to δ -Fe, there is approximately 60% of depletion of $M_{23}C_6$ carbides at all temperatures examined.

T / °C	status	M ₂₃ C ₆ content in white-bands / mass fraction		
		measured ¹	L to δ-Fe ²	L to γ-Fe ³
550	as-weld	1.74E-02	1.91E-02	1.91E-02
	after diffusion	0	1.13E-02	0
575	as-weld	1.73E-02	1.91E-02	1.91E-02
	after diffusion	3.31E-05	1.12E-02	0
600	as-weld	1.73E-02	1.90E-02	1.90E-02
	after diffusion	0	1.11E-02	0
650	as-weld	1.71E-02	1.89E-02	1.89E-02
	after diffusion	0	1.08E-02	0
700	as-weld	1.68E-02	1.88E-02	1.88E-02
	after diffusion	0	1.05E-02	0
760	as-weld	1.63E-02	1.84E-02	1.82E-02
	after diffusion	0	9.19E-03	0

1. Calculated using measured white-band composition at as-weld status (Table 5.3)
2. Calculated using modelled white-band composition when liquid solidifies to δ-Fe (Table 5.3)
3. Calculated using modelled white-band composition when liquid solidifies to γ-Fe (Table 5.3)

Table 5.5 Modelled contents of M₂₃C₆ carbide in white-band at as-weld stage and after diffusion at various temperatures

Chapter 6

Discussion

This chapter is divided into four major themes of discussion as follows, based on the experimental results and modelling results in chapters 4 and 5:

i. Microstructure and properties of P91 weld metal

The creep failure of complex weld structures consisting of different microstructural zones has been regarded as the primary life-limiting issue of the power plant components. In this work, full characterisation of P91 weld metal in isolation has been carried out on as-welded, PWHT and creep tested samples together with the P91 flux coated welding rod. A preliminary discussion will be conducted in this section (6.1) regarding the degradation of the microstructure and properties of P91 weld metal during creep exposure.

ii. Creep fracture modes and their effects on anisotropic creep behaviour of P91 weld metal

Based on the examination of the creep fractures on creep tested P91 weld metal, two modes of creep fracture were identified: creep fractures along columnar grain boundaries and creep fractures along white-bands. The mechanism of creep failure of P91 weld metal resulting from these two modes of initial failure will be discussed in this section (6.2). In addition, the anisotropic creep behaviour of P91 weld metal was also discussed in terms of a microstructural study of features of creep fractures and their distribution.

iii. The mechanism of formation of white-bands

This section (6.3) is the main discussion focusing on the formation mechanism of white-bands in P91 weld metal during creep. Full characterisation of white-bands has been carried out and the features of white-bands were investigated in section 4.3. In light of this, the formation of white-band has been proposed to consist of two processes: localised depletion of alloying elements at inter-bead boundaries during welding and carbon diffusion out of the region with

depletion of alloying elements during heat exposure. Full discussion will be carried out regarding the mechanisms of these two processes in this section.

iv. Use of thermodynamic modelling to understand white-band formation

Based on the understanding of formation of white-bands discussed in section 6.4, both depletion of alloying elements at inter-bead bead boundaries during welding and the carbon diffusion out of region with depletion of alloying elements during heat exposure were modelled using Thermo-Calc. This section seeks to compare the modelling results against the experimental results.

6.1 MICROSTRUCTURE AND PROPERTIES OF P91 WELD METAL

6.1.1 Microstructural features

Welding with an intense heat source can result in unique microstructural features in different regions of the weld. The classical definition of a weld structure includes unaffected parent metal, the heat-affected zone (HAZ) and weld metal (Lancaster, 1993), whilst Savage et al. (1976) introduced a more complicated metallurgical description of the weld interface region comprising two additional zones: the unmixed zone and partially melted zone. Both definitions are based on the welds covering both parent metal and weld metal. However, in this work, the P91 welds examined are the weld metal in isolation produced by the laying down of weld passes onto steel plates using Type M P91 weld rod, not involving any parent metal. Thus, the microstructural regions formed are slightly different from the above definitions.

Upon the microstructural examination of as-PWHT (Figure 4.1) and creep-tested (Figure 4.8 to 4.12) P91 multi-pass weld metal, two main microstructural regions were observed: a coarse columnar region and a recrystallised region (equi-axed region). The coarse columnar region, as in above definitions (Lancaster, 1993; Savage et al., 1976), comprises a martensite lath structure formed by the rapid directional solidification of liquid weld metal. The recrystallised region is formed by the recrystallisation of such columnar material during the reheating process associated with the deposition of the next bead onto a previously deposited bead, which takes the material back into the austenite region and creates an equi-axed structure. Similar to the HAZ between unaffected parent metal and weld metal, this region can be divided into two regions consisting of a coarse recrystallised region and a fine recrystallised region (Figure 4.2) due to the different peak temperatures experienced.

In addition to the columnar regions and recrystallised regions, some light-etched white-bands have been commonly observed on creep tested P91 weld metal (Figure 4.9 to 4.11), but not on as-welded P91 weld metal (Figure 4.43a) or PWHT P91 weld metal (Figure 4.2). As seen, these white-bands were mostly observed at the inter-bead fusion boundaries, but occasionally found within the

weld beads. It was noticed that some creep fractures formed along these white-bands, indicating their significant effect on the creep failure of P91 weld metal. Characterisation of white-bands indicated that they are recrystallised soft ferrite, with a much lower volume fraction of $M_{23}C_6$ carbides than the surrounding weld metal. It has also been noticed that not every inter-bead fusion boundary has developed to form a white-band during creep exposure. The detailed discussion about the features of white-bands and the mechanism of their formation will be presented in the Section 6.3.

The microstructural distributions in longitudinal creep specimens and transverse creep specimens are very different. As schematically shown in Figure 6.1, longitudinal specimens have a banded structure containing columnar regions and refined region, whilst the transverse specimens are made up of overlapped typical-shape beads.

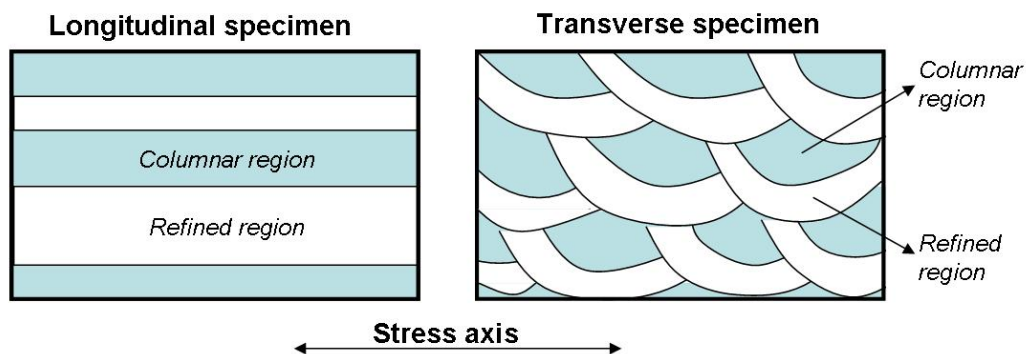


Figure 6.1 Microstructural distribution of longitudinal and transverse P91 weld metal creep test specimens

6.1.2 Hardness degradation

Inhomogeneity of microstructural distribution inevitably created the inhomogeneity of materials properties between columnar region and recrystallised region, such as hardness. As shown in Figure 4.4, the hardness of columnar region (260 to 285 kgf mm⁻²) is higher than that of recrystallised region (230 to 260 kgf mm⁻²) in the as-PWHT P91 weld metal. Columnar microstructures are creep-strong but

lack ductility, whereas the refined microstructures are more creep-weak but with a higher ductility.

The hardness of creep tested P91 weld metal was reduced greatly compared to that of as-PWHT P91 weld metal, to a range from 195 to 270 kgf mm⁻² (Figure 4.20) after creep testing at 650°C until failure. It suggests that the hardness of P91 weld metal reduces with longer heat exposure and with increased creep strain. Agyakwa (2004) has plotted the hardness against the Hollomon-Jaffe Parameter (HJP) of P91 weld metal after stress-free ageing showing the decrease of hardness with increasing exposure time and/or temperature. However, in this work, the effect of the stress and strain on hardness can be clearly observed, as shown in Figure 4.19. The gauge section and grip section of the creep tested specimen have experienced same thermal condition, but gauge section was under a stress load of 115 MPa (and this experienced strain) whilst the grip section is stress-free (and thus exhibited no creep strain). The hardness of the gauge section is much lower than that of grip section. The significant effect of stress and strain on hardness degradation has been documented (Watanabe et al., 2004), and it was also suggested that higher strain normally leads to more rapid degradation of hardness (Tanaka et al., 2001). The recovery of dislocations under stress has been regarded as the source of such hardness differences (Watanabe et al., 2004; Fujiyama et al., 1990). It was believed that strain aids the diffusion of species by providing an additional route along the core of dislocations (pipe diffusion), resulting in the more rapid precipitate coarsening, and therefore the reduction in the number of precipitates encouraged subgrain growth (recovery of martensite) (Agyakwa, 2004).

6.1.3 Precipitate coarsening

The primary precipitate observed in P91 weld metal is M₂₃C₆ carbide phase rich in chromium; this is typical of 9-12%Cr steels in a quenched and tempered condition. As shown in Figure 4.16 to 4.17, M₂₃C₆ carbides precipitated mainly on prior austenite grain boundaries and subgrain boundaries. The TEM EDX analysis indicated that M₂₃C₆ precipitates in P91 weld metal contain high chromium with iron and molybdenum. The size of M₂₃C₆ observed in the creep tested P91 weld metal ranges from 100 nm to 300 nm. The comparison of the precipitates in creep

tested samples to as-PWHT samples indicated the coarsening of the $M_{23}C_6$ carbides during creep exposure, but no noticeable increase in the numbers of precipitates. The $M_{23}C_6$ precipitates act to retard the subgrain growth and therefore increase the creep strength of the materials (Ennis et al., 1998), but their coarsening after long time exposure at high temperature can give rise to the initiation of creep cavities resulting in a reduction in creep strength (Anderson et al., 2003; Yin and Faulkner, 2005).

6.2 CREEP FRACTURE MODES AND THEIR ROLE IN ANISOTROPIC CREEP BEHAVIOUR OF P91 WELD METAL

6.2.1 Creep fracture modes of P91 weld metal

The observation of creep fractures in failed creep tested specimens (Figure 4.9 to 4.11) suggest that there are two type of creep fracture formation according to their locations: (i) creep fractures in the columnar regions and (ii) creep fractures along the white-band at or near the inter-bead fusion boundaries, with the former type being much more common than those of the latter type. Sources of creep fractures were not observed in the refined region since it has much higher creep ductility.

The creep fractures in the columnar regions are the most typical weld metal fracture type, generally termed type I failure (Francis et al., 2004; Fujibayashi et al., 2004). This type of fracture initiates as creep cavities and links up to form fractures on the prior austenite grain boundaries. As seen, creep fractures along columnar grain boundaries are generally constrained by the refined region adjacent to the weld beads, which are more ductile and resistant to cracking. However, fractures that extend past this stage can grow to the full weld dimension, leading to final rupture of the weld metal. The coarsening of the precipitates was found to give rise to the formation of the creep cavities along the columnar grain boundaries. These precipitates are primarily $M_{23}C_6$ carbides, which coarsen rapidly after long-term creep exposure (Orlova et al., 1998). In other work, most of creep tests on cross welds covering both parent metal and weld metal have shown Type IV failure occurring in intercritical heat-affected zone (ICHAZ) (Francis et al., 2004; Issler et al., 2004). However, in this work, creep testing was carried out on P91 weld metal in isolation. Hence, the creep fractures along the columnar grain boundaries are the primary type of creep fractures observed in this work. In addition, even in creep tests of cross welds covering parent metal and weld metal, weld metal failures in coarse columnar regions have also been reported by some researchers (Watanabe et al., 2006, Fujibayashi et al., 2004). This indicates the importance of understanding the creep response of P91 weld metal itself.

In this work, another type of creep fracture was observed to form along the light-etched white-bands at or near the inter-bead fusion boundaries. It has been noticed that the white-band regions are creep-weak due to their fully recrystallised, carbide-free microstructure and their much lower hardness. However, although white-bands have been frequently observed on creep tested P91 weld metal in this work, they did not necessarily lead to creep cracks. It was found that most creep fractures have formed along white-bands at an angle of approximately 45° to the stress axis. It is unlikely to see creep fractures along white-bands on longitudinal specimens even though the white-band regions are weak, since white-bands on longitudinal specimens are normally parallel to the stress axis. In contrast, white-bands on transverse specimens are more likely to lead to the formation of creep cracks, especially for the white-bands located at an angle of approximately 45 ° to the stress axis. The white-bands at this angle are where the highest shear stress occurs during creep. Such cracks are also easier to propagate into a refined region which then fails by plastic shear.

The creep fractures along white-band regions are much less common than the creep fractures in columnar regions in creep tested P91 weld metal specimens, and seem to be less significant in the direct failure of the materials. However, some of creep fractures in columnar regions were observed to propagate along white-bands at fusion boundaries when they were constrained by the refined microstructures. Creep fractures along white-bands thus have the effect of linking the fractures in the columnar regions during creep, contributing significantly to the final rupture of P91 weld metal, especially in the case of the transverse specimens.

6.2.2 Anisotropic creep behaviour of P91 weld metal

By comparing the creep testing results of P91 weld metal from both the longitudinal and transverse orientations at 650°C and various stress levels in Table 4.2, it is clear that the longitudinal specimens had much longer creep lives than the transverse specimens at all applied stress levels, and the strain to failure of longitudinal specimens were all much higher than those of transverse specimens. This anisotropic creep behaviour of P91 weld metal has also been observed by Hyde et al (2003; 2004; 2005). Their creep tests on 9CrMoNbV weld

metal demonstrated a significant difference in creep behaviour of the weld metal from two orientations, with the longitudinal specimens exhibiting a longer failure life and larger strain to failure than the transverse one.

To investigate the anisotropic creep behaviour of P91 weld metal, most previous work focused on the creep test data (strains, creep lives etc.), whereas the investigation on microstructure evolution and creep fracture modes are seldom related to the anisotropic creep behaviour. Based on the microstructural examination of creep tested P91 weld metal in this work, some correlation can be made between their anisotropic creep behaviour and microstructural distributions and creep fractures modes.

As previously discussed (Figure 6.1), the longitudinal specimens had a banded structure containing columnar and refined bands. Due to the strain compatibility, during creep the stress will be increased in the columnar regions (creep-strong regions) and reduced in the refined regions (creep-weak regions). When its relatively lower ductility is exhausted, the stress will be concentrated on the refined region which is creep-weak but with higher ductility, until it fails by plastic shear. In contrast, transverse specimens are made up of overlapped typical-shape beads. During creep, the stress is applied on both the creep-strong columnar region and creep-weak refined region, so transverse specimens normally have shorter creep life and lower creep strain to failure. In addition, creep fracture along white-bands, which has been frequently observed on transverse creep tested specimens, is also regarded as another factor contributing to the shorter creep life of transverse specimens, since these premature creep fractures acted as a linkage between the creep fractures along the columnar grain boundaries. The effect of white-band creep fractures can be significant on creep failure of transverse weld metal. Allen et al. (2005) have reported the creep failure of P92 weld metal in some cross-weld creep specimens, which took place dominantly by the linkage of severe white-band fractures.

The strain to failure and reduction in area of longitudinal P91 weld metal specimens were also much higher than those of transverse P91 weld metal specimens (Table 4.2 and Figure 4.20). This can also be attributed to their different distribution of columnar regions and refined regions. The longitudinal

specimens, which have banded ductile refined region along the stress axis, accounted for the large deformation of creep specimens.

6.3 MECHANISM OF WHITE-BAND FORMATION

A preliminary discussion regarding the mechanism of white-band formation has been given in Section 4.3.6, indicating a two-stage process: (i) the inhomogeneity of alloying element distributions in P91 weld metal following welding and (ii) carbon diffusion out of the alloy-depleted regions during heat exposure. The mechanisms of these two processes will be discussed in this section based on the characterisation of white-bands.

6.3.1. Features of white-bands

Light etched white-bands were not present in the as-welded and as-PWHT P91 weld metal, but were commonly observed following creep exposure of the specimens. Most of them formed at the inter-bead fusion boundaries, but they were also occasionally observed within the weld bead near to the fusion boundaries (Figure 4.9 to 4.11).

All the white-bands examined showed different levels of $M_{23}C_6$ depletion, with some of them being almost free of such carbide particles altogether (Figure 4.26 and 4.28). Without the pinning effect of these precipitates on grain boundaries during creep exposure, these regions recrystallised into large ferrite grains (Figure 4.24 and 4.25) having the light-etching characteristics (compared with surrounding martensite) which lead to them being described as 'white-bands'. The hardness of the white-band regions was found to be much lower than that of the hardness of the bulk weld metal (Figure 4.33 and 4.34). The absence of the pinning effect of carbide particles together with the loss of the martensite lath structure and the formation of the large, soft ferrite grains has led to the significant reduction in creep strength of these regions. However, small MX type precipitates such as VN particles were observed in white-bands within the subgrain interior.

Chemical analysis on as-welded samples and creep tested samples using EDX and LIBS techniques suggested the inhomogeneity of the element distribution in P91 weld metal. The localised depletion of alloying elements (chromium, manganese and molybdenum) existed at inter-bead fusion boundaries following

the welding process whilst carbon was uniformly distributed at this stage (Figure 4.43); hence no evidence of light-etching white-bands was observed in as-welded P91 weld metal. However, chemical analysis on creep tested P91 weld metal indicated that not only the depletion of alloying elements at the inter-bead fusion boundaries but also the severe depletion of carbon at same regions (Figure 4.41). It is suggested that carbon diffused out of the pre-existing alloy-depleted regions during creep exposure. This was also confirmed by the observation of white-bands on the P91 weld metal after ageing (at 760°C for 3 hours followed by 650°C for 30 hours), where light-etching white-band started to appear (Figure 4.44) in the alloy-depleted regions. The depletion of $M_{23}C_6$ carbide particles observed in white-band regions during creep indicated that the continuity of carbon diffusion out of the white-band was supported by the dissolution of carbide particles. Carbon concentration in white-band regions can reach a very low value (< 0.01 wt%), which explains why some of the white-bands were free of carbide particles.

White-bands, although not well documented, have been found on P92 weld metal, leading to final rupture of specimens (Allen et al., 2005), as shown in Figure 2.26. In this work, they were also identified as carbon-depleted microstructural bands having different composition from the bulk weld.

6.3.2 Inhomogeneity of alloying element distributions in as-welded state

Two mechanisms by which the alloy-depleted regions may have formed are discussed.

6.3.2.1 Poor mixing

Savage et al (1976) have proposed the existence of a thin, melted but unmixed layer at the fusion boundaries of the weld (Figure 2.10b). They argued that, while molten, the materials in this region only experienced lamellar flow indicating that the liquid here did not experience convective mixing but only diffusion mixing. Allen et al (2005) also mentioned that this layer is prevented from being stirred into the upper bead weld pool by the viscous resistance. The P91 weld metal in this work was made using flux-coated type M P91 weld rods, with a mild steel core coated by a flux containing the necessary alloying elements in the form of

ferro-alloy metallic particles. As such, the presence of the unmixed layer at inter-bead fusion boundaries may not have experienced full mixing of mild steel core materials and alloying elements contained in ferro-alloy particles, resulting in the depletion of alloying elements in this layer.

6.3.2.2 Solute partition during weld solidification

The simulation P91 TIG welds were made by melting and resolidification of P91 steel plate, where no filler material was added during welding so that there will not be a difference in chemical composition of the unmixed zone and bulk weld metal. However, depletion of alloying elements (mainly chromium) has been observed at the fusion boundaries of P91 TIG weld (Figure 4.49), but the level of depletion is much lower than that observed in P91 MMA weld metal using Type M consumables. The depletion of carbides in the alloy-depleted regions was also observed on heat-treated P91 TIG weld (Figure 4.52), but only at a very low level. It suggested that there are reasons other than poor mixing of weld pool materials which may contribute to the localised depletion of alloying elements at the levels observed in P91 MMA weld metal using Type M consumables.

Solute partition during weld solidification has also been considered as a possible mechanism resulting in the formation of localised alloy-depleted region at the fusion boundaries. Savage (Savage, 1978) and Porter (Porter, 1992) have described the mechanism of weld solidification as (i) no diffusion in the solid; (ii) no mechanical mixing in the liquid; (iii) only diffusion mixing in the liquid. During weld solidification, there is always a stagnant unmixed zone without convective mixing in the liquid at the advancing solid-liquid interface. Since the extent of the diffusion zone in the liquid is small compared to the thickness of this unmixed layer, no convective mixing at the advancing solid-liquid interface is proposed. Due to the high temperature gradient and low solid growth rate at the fusion boundary on the two sides of the weld bead (Figure 2.15), planar front solidification normally occurs in this region as shown schematically in Figure 2.16 (David and Vitek, 1989), which can result in the solute partition at the advancing solid-liquid interface (Figure 2.17). This means that an alloy with nominal solute composition C_0 will begin to solidify with the formation of first solid with the composition of k_0C_0 , where k_0 is the equilibrium partition coefficient. Since $0 < k_0 < 1$, the first solid formed will be depleted in solute (i.e. alloying elements in P91

weld metal). However, it has also been argued that in the case of interstitial atoms (such as carbon and nitrogen), the solute atoms can diffuse away from the solidifying interface back into the solid, with the result that after solidification these solute atoms are more uniformly distributed (Porter, 1992). This indicates why only depletion in alloying elements was observed at the inter-bead fusion boundaries whilst carbon was uniformly distributed in as-welded P91 weld metal (Figure 4.43a).

David and Vitek (1989) have also indicated that solute inhomogeneities over a large scale can be referred to as macrosegregation, which can be produced by sudden changes in the growth velocity, or by bulk flow of solute enriched or depleted liquid caused by convection. A schematic diagram showing compositional fluctuations resulting from changes in growth rate is shown in Figure 6.2. In the solidification of P91 weld metal made by the manual metal arc (MMA) method, sudden changes in the welding speed may have occurred, which result in the changes in the growth rate of solid-liquid interface. This could explain why white-bands have also been occasionally observed within the weld beads themselves. In contrast, the P91 TIG weld was welded with a robot under a pre-set steady welding speed and as such, no such changes in growth rate may occur, thus explaining why no any evidence of solute segregation within the weld bead was observed. Flemings et al. (1967; 1968) have also shown that changes in the size of the mushy zone (due to thermal conditions being affected by convection within the mushy zone) can result in solute enriched or depleted banding. Figure 6.3 shows an example of such variations in the form of banding in an Al-Li alloy GTA weld.

The equilibrium partition coefficient of chromium between solid (δ) and liquid in binary iron alloys is 0.94 (Table 2.4), which is only able to cause a chromium partition to approximately 8.5 wt% for the P91 weld metal, which is much higher than the chromium content actually measured in the white-bands. It is suggested that solute partition on its own cannot induce the depletion of alloying elements in the level observed.

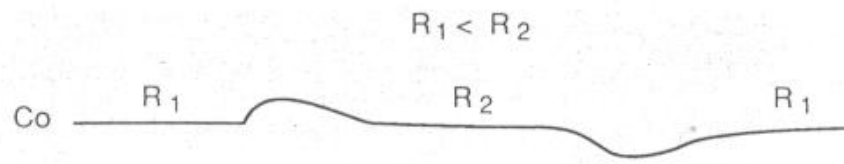


Figure 6.2 Schematic diagram showing compositional fluctuations resulting from changes in growth rate (David and Vitek, 1989)

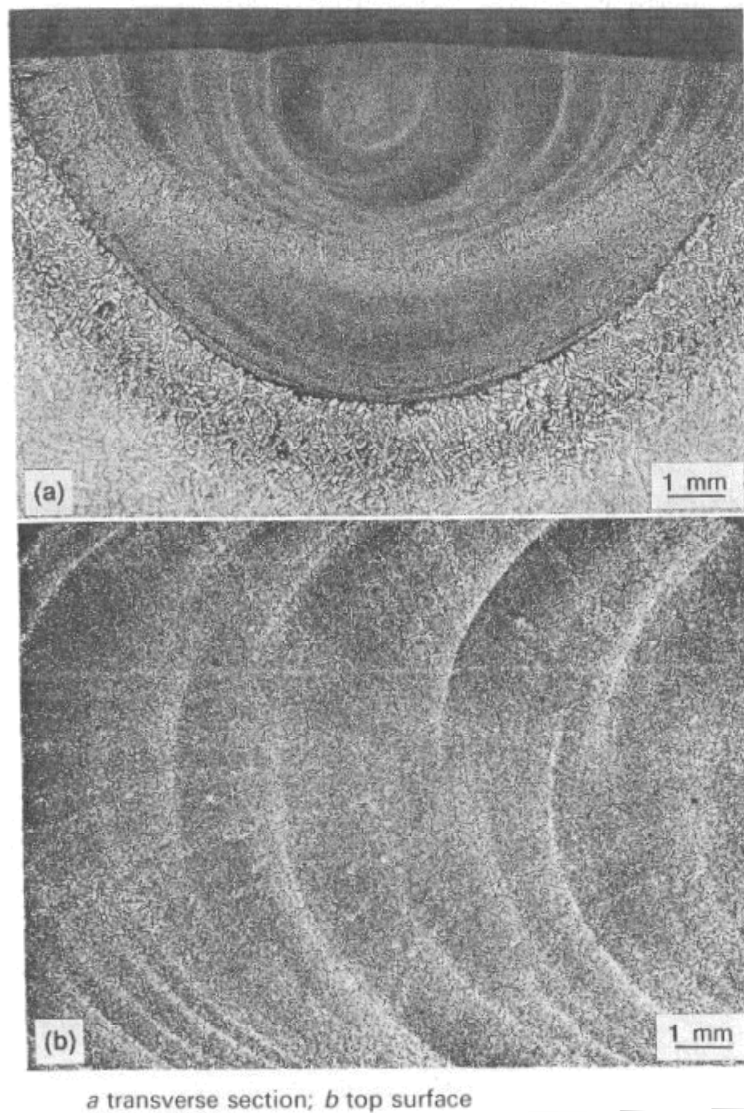


Figure 6.3 Photomicrographs showing banding in Al-Li alloy GTA weld (David and Vitek, 1989)

6.3.2.3 Summary

In a summary, the formation of alloy-depleted regions at inter-bead fusion boundaries in P91 weld metal may result from both the poor mixing in an unmixed zone close to the fusion boundaries and solute depletion at the solid-liquid interface during weld solidification. In addition, the changes in welding speed and convection flow during MMA welding may result in the occasional presence of alloy-depleted bands within the weld beads.

6.3.3 Carbon diffusion out of the alloy-depleted regions

The LIBS analysis has indicated that the white-band regions following creep testing are significantly depleted in carbon (and carbides), these regions being depleted in alloying elements in the as-welded condition (Figure 4.41). Given that there was no evidence of white-bands being present before creep testing (and thus that carbon was evenly distributed across the welds in the form of carbides), it implies that carbon diffusion out of the alloy-depleted regions is the mechanism which promotes carbide dissolution and hence recrystallisation into the large ferrite grains. This has also been mentioned by Allen et al. (2005) for the white-bands in their creep tested P92 weld metal.

Although the carbon concentration and carbide distributions are uniform in the as-welded microstructure, there will have been a gradient in the activity of carbon due to the inhomogeneity of the other alloying elements (such as chromium, manganese and molybdenum). Diffusion driven by an activity gradient was first reported in Darken's experiment (Stark, 1980) and has been reported frequently in the examination of carbon diffusion in welds between dissimilar steels. Creep failure of dissimilar welds is commonly observed at the weld metal / HAZ interface (which is termed as type IIIa creep failure) (Schuller et al., 1974). This type of failure is associated with carbon migration across the weld interface, a process which starts during PWHT and continues with operation at service temperature (Brett, 2004; Mannan and Laha, 1996; Fujibayashi et al., 2004; You et al., 2001). It was noticed that carbon diffusion across the weld interface will result in a carbon-depleted region on the low chromium side and a carbon-rich region on the

high chromium side. Laha et al. (2001a; 2001b) have observed the carbon depleted zone in 2.25Cr-1Mo/9Cr-1Mo dissimilar weld joint where the carbon content was the same in parent metal and the weld metal (0.12 wt%) before thermal exposure. Hence, carbon migration across the interface of dissimilar welds is actually driven by carbon activity gradient which is caused by differences in alloy content (mainly the difference in chromium content in this case) in parent metal and weld metal. Carbon activity can be calculated using following equation,

$$a_c = N_c \gamma_c \quad [6.1]$$

where a_c is the carbon activity; γ_c is carbon activity coefficient, which can be expressed by Wagner's relationship (Pilous and Stransky, 1998),

$$\gamma_c = \exp(\varepsilon_C^{Cr} N_{Cr(eq)}) \quad [6.2]$$

where ε_C^{Cr} is the Cr-C thermodynamic interaction coefficient (*at. fraction*⁻¹), which is temperature dependent only (Million et al., 1995). According to Table 2.5 and 2.6 in section 2.3.4 (Pilous and Stransky, 1998), the chromium equivalent $N_{Cr(eq)}$ for P91 weld metal can be expressed as following equation,

$$N_{Cr(eq)} = N_{Cr} + 0.386N_{Mn} + N_{Mo} + 2.08N_{Nb} - 0.442N_{Ni} - 0.574N_{Cu} - 0.673N_{Si} \quad [6.3]$$

(at. fraction)

This indicates that carbon activity is significantly affected by a number of elements, but since chromium is the main alloying element in creep resistant ferritic steels, it has made biggest contribution to the difference of carbon activity in dissimilar welds. It can also be noticed that among the elements (Cr, Mn and Mo), which showed the most severe depletion in white-bands, the contribution of Mn content to the chromium equivalent is much less than that of Cr and Mo; Nb content can make the biggest contribution to chromium equivalent but its content is normally very low in ferritic steels; whilst Ni, Cu and Si contents in fact reduce the chromium equivalent. Most of work on carbon migration between dissimilar welds mentioned above only suggested the effect of chromium on the carbon activity. Sopusek and Foret (2004; 2008) have calculated the carbon activities of steels

with different chromium contents using CALPHAD method, indicating that the chromium content significantly affected the carbon activity in steels. However, it needs to be realised that other alloying elements can also contribute more or less to the migration of carbon depending on the steel composition.

In the weld interface of dissimilar welds, it was also usually observed that there are less carbide precipitates in carbon-depleted zone and more carbide precipitates in the carbon-rich zone, as in Figure 2.25, indicating that the loss of carbon in the carbon-depleted zone will cause the dissolution of carbide precipitates. The recrystallisation caused by the lack of the pinning effect of these precipitates resulted in a much softer carbon-depleted zone. In contrast, a carbon-rich zone is much harder with high content of carbide precipitates and original martensitic microstructure. The mismatch of microstructure and properties of materials on these two adjacent zones will eventually result in the failure at the weld interface.

Based on the understanding of carbon migration between dissimilar welds, it is proposed that this mechanism is also applicable to the current case of relatively local inhomogeneities in substitutional element concentrations within the weld metal itself, which produces the diffusion of carbon and dissolution of the carbides. In the case of white-bands, which are normally 50 to 200 μm wide, the volumes of materials from which the carbon is diffusing (the alloy-depleted regions) are small; this means that the source volume of the carbon is small, resulting in rapid diffusion out of the white-band region and also rapid attainment of local equilibrium in carbon. This explains why most of the white-bands observed in creep tested P91 weld metal were almost free of carbides and had very low carbon levels (< 0.01 wt%), even with only 1 wt% to 2 wt% of chromium depletion. Hence, these white-bands in creep tested P91 weld metal are expected to have much lower hardness and to be more creep-weak compared to the carbon-depleted region at the interface of dissimilar welds, even with same level of chromium difference; the formation of white-bands will also occur in a shorter period. As a result, some creep fractures will form in white-band regions, which can cause or contribute to the pre-mature creep failure of the P91 weld metal. This also explains additionally why transverse specimens with more creep fractures in white-band regions have shorter creep lives.

6.4 USE OF THERMODYNAMIC MODELLING TO UNDERSTAND WHITE-BAND FORMATION

The Thermo-Calc modelling of white-band formation involved two main processes: the modelling of solute partition during weld solidification of P91 weld metal and the modelling of carbon diffusion out of the alloy-depleted regions during heat exposure. As shown in chapter 5, work has been done in understanding the equilibrium phase of P91 weld metal, the composition of first solid during solidification, the correlation of carbon activity with temperature and alloying element content, and the limiting carbon concentration and carbide content in white-bands of P91 weld metal. It also needs to be realised that the Thermo-Calc modelling in this work only considers the effects of thermal exposure but not the creep strains since although it is known that creep strain enhances diffusion, this kinetic effect cannot be simply incorporated into the thermodynamic model.

6.4.1 Solute partition during weld solidification of P91 weld metal

The vertical section (isopleth) of the T/P91 phase diagram with constant chromium content in Figure 2.5 (Ayala et al., 1999) showed a line with corresponding carbon content (0.1 wt%) of T/P91 steel, indicating the evolution of phases with temperature. In the current work, the equilibrium phases of P91 weld metal with measured bulk weld composition specified in Table 5.2 were calculated against temperature. As shown in Figure 5.1, the first solid formed will be δ -ferrite, which will transform to austenite with decreasing temperature.

The composition of the first solid during solidification from liquid to δ -ferrite was calculated. The depletion of alloying-elements can be seen as the modelled first-solid composition ($L \rightarrow \delta\text{-Fe}$) in Table 5.3. Compared to the measured composition of white-bands in P91 weld metal, the modelled composition showed a much lower level of alloy-depletion, with chromium depletion being only 0.4 wt%. This suggested that the solute partition on solidification cannot result in the levels of alloy-depletion observed in P91 weld metal. It either has not contributed to the localised alloy depletion of the white-band in P91 weld metal or has only contributed as a minor factor.

In contrast, the analysis of P91 TIG weld indicated a slight depletion of chromium of approximately 0.3 wt% at the weld interface. Since the P91 TIG weld was actually made by a simple process of melting and resolidification of P91 parent metal with a similar chemical composition to the MMA P91 weld metal, and did not involve any addition of weld consumables, the depletion of alloying elements at this weld interface will result from only the solute partition without the possibility of poor mixing in the stagnant layer at the weld interface during solidification. The measured level of chromium depletion (0.3 wt%) in P91 TIG weld is very similar to the modelled first-solid composition ($L \rightarrow \delta\text{-Fe}$) of P91 weld metal, confirming the localised depletion of chromium in P91 TIG weld is solely caused by solute partition. Since chromium existed in type M P91 consumables mostly in the form of ferro-chromium particles, it is very likely that the poor mixing in the stagnant layer at the weld interface reduced the transportation of chromium from weld pool into this layer, resulting in the level of depletion as measured (1.3 wt%).

The Thermo-Calc modelling results also showed that Mn should experience a high level of partition during solidification ($L \rightarrow \delta\text{-Fe}$) from 1.18 wt% to 0.87 wt%, which is even lower than the measured Mn content in the white-bands (0.98 wt%). The prediction of Mo partition to 0.972 wt% is similar to the measured Mo content in white-bands (0.96 wt%). Although in the P91 welds, Cr, Mn and Mo all experienced a similar level of depletion in white-bands of approximately 15%, the prediction from Thermo-Calc modelling indicated that they should experience different levels of solute partition. However, the formation mechanism of the alloy-depletion region observed in P91 weld metal can be very complex. Other than solute partition, poor mixing in the stagnant layer is also significant. However, it is difficult to evaluate the effects of poor mixing on each element in this work.

In addition to the solidification from liquid into δ -ferrite as first solid assumed above, Fredriksson (1976) has also argued concerning the possibility of solidification from liquid into austenite (γ). This can happen if the cooling rate is large enough, even when δ -ferrite is the thermodynamically favoured phase, and if the steel is alloyed with austenite stabilising elements. During the Thermo-Calc modelling of solidification directly into austenite as primary phase, the ferrite phase was made dormant. As shown in Table 5.3, the calculated chemical composition of first solid formed during $L \rightarrow \gamma\text{-Fe}$ solidification showed much higher partition in Cr and Mo than that during $L \rightarrow \delta\text{-Fe}$ solidification, whilst Mn

was predicted to have lower partition during $L \rightarrow \gamma\text{-Fe}$ solidification than $L \rightarrow \delta\text{-Fe}$ solidification. In this case, the predicted Cr and Mn contents in first solid ($L \rightarrow \gamma\text{-Fe}$) are about same as the measured Cr and Mn content in white-bands, whilst the predicted Mo content is much lower than the measured Mo content in white-bands. It has been noticed from the modelling results that Cr and Mo as ferrite stabilisers experience higher partition during $L \rightarrow \gamma\text{-Fe}$ solidification, and Mn as an austenite stabiliser experiences higher partition during $L \rightarrow \delta\text{-Fe}$ solidification. Compared to the chemical composition of grade 91 specified by ASTM standards in Table 2.2 (0.3 to 0.6 wt% Mn), the P91 weld metal in this work contains higher Mn (1.18 wt%). As an austenite stabiliser, higher Mn was added into the weld metal to ensure 100% austenite transformation (without δ -ferrite) during solidification, thus ensuring 100% martensite when cooled (Hayashi et al., 1999). Hence, it is possible that liquid P91 weld metal will solidify (either partially or wholly) into austenite directly. Again, the poor mixing of weld metal in the stagnant layer is still important in the formation of localised alloy-depleted region at fusion boundaries, which is the prerequisite of white-band development.

6.4.2 Parameters affecting the carbon activity in P91 weld metal

The dependence of carbon activity on chromium content in steels has been discussed extensively in previous work on the carbon migration in dissimilar welds, suggesting that chromium can reduce carbon activity. Foret et al. (2001) and Million et al. (1995) have confirmed the suitability of using a stationary model to predict carbon diffusion in dissimilar welds (section 2.3.4). Sopousek and Foret (Sopousek and Foret, 2008) have calculated the carbon activity of steels with different chromium contents using the CALPHAD method (Figure 6.4) showing the large effect of chromium content on the carbon activity, and also modelled the correlation between carbon activity and temperature (Figure 6.5) for different steels demonstrating an approach in selecting material for dissimilar welds to reduce the carbon migration. In this work, the carbon activity of P91 weld metal was calculated against temperature, and the dependence of carbon activity on chromium, manganese and molybdenum was calculated respectively to understand the effects of their depletion on the development of white-bands.

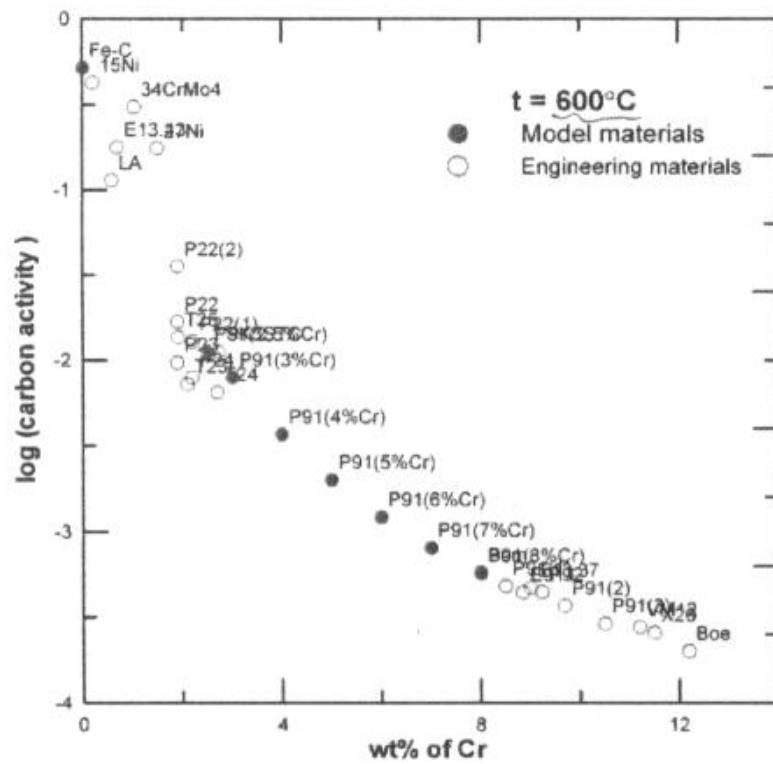


Figure 6.4 Correlation between logarithm of carbon activity and chromium content for different materials (Sopousek and Foret, 2008)

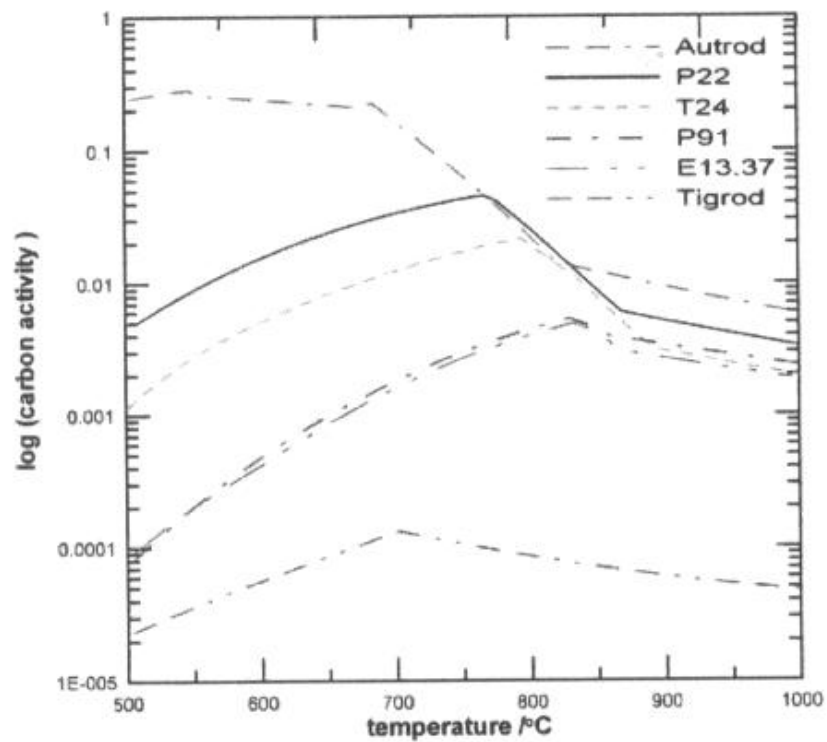


Figure 6.5 Temperature dependence of carbon activity for different steels: dependence breaks represent phase transformation (Sopousek and Foret, 2008)

The plot of carbon activity of P91 weld metal against temperature (Figure 5.3) indicated that within the temperature range where low temperature α -ferrite and $M_{23}C_6$ carbides are stable, carbon activity increases with increasing temperature. In contrast, carbon activity at higher temperature range where austenite is stable and $M_{23}C_6$ carbides completely dissolve decreases with increasing temperature. This results is consistent with the prediction from Sopousek and Foret's work (2008) as in Figure 6.5.

Comparing the three plots of carbon activity against chromium content, molybdenum content and manganese content in Figure 5.4, it can be seen that chromium has biggest effect on carbon activity, where higher chromium content will result in lower carbon activity. A reduction of chromium of only 1.37 wt% in P91 weld metal will result in an increase of carbon activity to 1.5 times. Mo has similar effect on carbon activity, but to a relatively lower level due to its lower level of presence in P91 weld metal. However, carbon activity is not significantly influenced by manganese content. This is in agreement with the calculation of chromium equivalent as in equation [6.3]. Manganese does not contribute to the chromium equivalent, whilst although molybdenum has same contribution (same ratio) to the chromium equivalent as chromium, its contribution in the case of P91 weld metal is smaller than that of chromium due to its much lower additional level (1.13 wt%). It suggested that although chromium, molybdenum and manganese had similar levels of depletion (15% reduction) in the white-bands, their contributions to the carbon activity gradient are different. Hence their effects on the development of carbon migration during heat exposure are also different.

6.4.3 Carbon and carbide depletion in white-bands during heat exposure

The modelling strategy described in section 5.3.1 was built upon the premise that since white-bands are very small in thickness (typically 50 to 200 μm) compared to the bulk weld, a limiting carbon concentration can be calculated by assuming the carbon activity in white-bands to develop to a value approximately the same as that in the bulk weld in the as-welded condition. With the depletion of alloying elements as measured, the predicted limiting carbon concentrations in white-bands at all temperatures examined will eventually reduce to about 0.01 wt%, and at these concentrations, the models predict that (at all temperature examined),

there will be no $M_{23}C_6$ carbides present. Both results showed good correlation with experimental measurements of carbon concentration and $M_{23}C_6$ carbide content of the white-band regions in creep tested P91 weld metal.

The calculation of the equilibrium phase content with single depletion of Cr, Mn or Mo is in agreement with the previous results on effects of these elements on carbon activity (Table 5.4): depletion of Cr only will still result in high level of carbide depletion to 10% of its original value; depletion of Mn only will not result in any significant depletion of carbides; depletion of Mo only will result in the carbide depletion to 76% of its original value.

The calculation of equilibrium phase content in white-bands using predicated first-solidified composition in the cases of both $L \rightarrow \delta\text{-Fe}$ and $L \rightarrow \gamma\text{-Fe}$ solidification suggested that the level of solute partition during $L \rightarrow \delta\text{-Fe}$ solidification will not cause the complete dissolution of $M_{23}C_6$ carbides in these regions, whilst the level of solute partition during $L \rightarrow \gamma\text{-Fe}$ solidification will result in a complete dissolution of $M_{23}C_6$ carbides. It also implied that if the depletion of alloying elements is small, a white-band with complete dissolution of carbides will never form regardless the time of diffusion. The calculation of limiting carbon concentration and carbide content in white-bands has been carried out with various levels of depletion of alloying element (25%, 50%, 75%, 100%, 125% and 150% of measured composition of the as-welded white-band), as shown in Figure 5.6 and 5.7. These results indicated the linkage between carbon depletion and carbide depletion in white-bands: with alloy-depletion less than 100% of the average white-band depleted level, the $M_{23}C_6$ carbide level will not be reduced to zero. This clearly indicates that there will be a range of levels of alloy depletion throughout the weld metal, but that only in regions where its depletion is greater than a certain value will the area recrystallise (due to loss of carbides) and the white-bands form in a microstructurally obvious manner. This indicates why the white-bands only form sporadically throughout the weld.

6.4.4 Summary

Thermo-calc modelling of solute partition during solidification of P91 weld metal has indicated that solute partition will contribute to the formation of localised alloy-depleted regions in P91 weld metal in addition to poor mixing in the stagnant layer at weld interface. The dependence of carbon activity on Cr, Mo and Mn was also investigated. The predicted limiting carbon concentration and $M_{23}C_6$ carbide content in white-bands showed good correlation to the measured values. In addition, it was also suggested that depletion of carbides and carbon are strongly linked and that depletion of alloying elements only above a critical value will result in total carbide loss and thus recrystallisation into a white-band.

Chapter 7

Conclusions

This research work has concentrated on the investigation of microstructure and mechanical properties of the P91 weld metal during creep exposure in the aspects of microstructural degradation, anisotropic creep behaviour, mechanisms of creep failure and formation of creep weak zones. The major conclusions drawn can be summarised as follows,

- i. The hardness of the P91 weld metal decreased after creep exposure. In addition to the thermal effect, strain also had very strong effect on the reduction of hardness since the gauge section of creep specimens with high creep strain exhibited a much more severe reduction in hardness than the strain-free grip end of the specimens.
- ii. The microstructural regions observed in P91 weld metal included coarse columnar regions and refined (equi-axed) regions, with different distribution of these regions in the longitudinal and transverse specimens. The creep exposure have caused the evolution of the microstructural features such as precipitate coarsening (mainly $M_{23}C_6$) and formation of creep-weak regions (termed white-bands) at inter-bead fusion boundaries. Two types of creep fracture modes were observed in P91 weld metal: creep fractures along coarse columnar grain boundaries and creep fractures along creep-weak white-bands (mostly observed in transverse specimens).
- iii. White-band regions observed in creep tested P91 weld metal were characterised as being fully recrystallised to large ferrite grains and almost free of $M_{23}C_6$ carbides, but with the presence of vanadium nitride precipitates. These white-band regions exhibited much lower hardness than that of the surrounding bulk weld metal due to the fully recrystallised microstructure and depletion of $M_{23}C_6$ carbides.
- iv. The anisotropic creep response of P91 weld metal is apparent in that longitudinal specimens had longer creep lives than transverse specimens. It can be correlated with the microstructural distribution of columnar regions and

refined regions. Formation of creep fractures along creep-weak white-bands has been regarded as an additional contribution to the shorter creep life of transverse specimens.

- v. The inhomogeneity of the element distribution in P91 weld metal was confirmed with LIBS element analysis, showing the localised depletion of alloying elements (mainly Cr, Mn, and Mo) at weld metal inter-bead boundaries. It is argued that the inhomogeneity is partially attributed to the poor mixing of a base steel (the core rod in the weld consumable) and particles of various ferro-alloys (delivered into the weld pool from the flux) in the stagnant layer (unmixed zone) at the solid-liquid interface during weld solidification. In addition, solute partitioning of substitutional alloying elements such as Cr, Mn and Mo has been regarded as a part of the contribution to the formation of alloy-depleted regions, being confirmed by the characterisation of simulation P91 TIG weld metal and the results of Thermo-Calc modelling.
- vi. Based on the literature survey of carbon migration in dissimilar welds, a similar mechanism can be established for the carbon depletion in the white-band regions during creep exposure. Carbon activity in the white-band region and bulk weld metal can be very different, even with a low level of alloying-element depletion, which drives the carbon diffusion out of the alloy-depleted regions to form white-bands with less than 0.01 wt% of carbon and almost no carbides.
- vii. With Thermo-Calc modelling, it was found that carbon activity is strongly dependent on chromium and molybdenum, but less so on manganese. The predicted limiting carbon concentration and $M_{23}C_6$ carbide content in the white-bands showed good correlation to the measured values. It was also suggested that depletion of carbides and carbon are strongly linked and that depletion of alloying elements only above a critical value will result in total carbide loss and thus recrystallisation into a white-band.

It was thought that the formation of creep-weak white-bands could be further investigated with examination of various 9-12%Cr steel welds made with different welding consumables and methods in an attempt to avoid the poor mixing which could have occurred in the deposition of this P91 weld metal. In addition, based

on these experimental studies, the modelling of white-band formation should be optimised and extended to predict the formation of white-bands in welds in terms of the levels and kinetics of carbide dissolution and depletion. Ultimately, alloys or consumables should be designed that are not prone to white-band formation.

References:

- AGYAKWA, P. A. (2004), Creep and microstructure development in P91 weldments at Elevated temperature. *School of Mechanical, Materials and Manufacturing Engineering*, University of Nottingham, PhD thesis
- AGYAKWA, P. A., SHIPWAY, P. H., WILLIAM, J. A. & HYDE, T. H. (2003) Effect of thermal ageing on microstructure and creep properties of a welded 9% chromium steel structure. In: Hyde, T.H., et al, eds. *Proceedings of 2nd International Conference of Integrity of High Temperature Welds*. London, IOM Communications, 135-145.
- ALBERT, S. K., MATSUI, M., WATANABE, T., HONGO, H., KUBO, K. & TABUCHI, M. (2003) Variation in the Type IV cracking behaviour of a high Cr steel weld with post weld heat treatment. *International Journal of Pressure Vessels and Piping*, 80, 405-413.
- ALLEN, D. J., HARVEY, B. & BRETT, S. J. (2005) FOURCRACK Advanced coal-fired power plant steels-avoidance of early weld failure by 'type IV' failure. *DTI Cleaner Coal Project 225*, E.ON UK plc.
- ANDERSON, P., BELLGARDT, T. & JONES, F. L. (2003) Creep deformation in a modified 9Cr-1Mo steel. *Materials Science and Technology*, 19, 207-213.
- AYALA, E., ROMAN, M., VEGA, J., GOMEZ, X., GENEZ-ACEBO, T. & ECHBERRIA, J. (1999) Delta ferrite formation in 9-12% chromium steel weldments, In: Viswanathan, R. and Nutting, J., eds. *Advanced Heat Resistant Steels for Power Generation*, London, The Institute of Materials, 633-643
- BERGQUIST, E. L. (1999) Consumables and welding modified 9Cr-1Mo steel. *Svetsaren*, 54(1-2), 22-25
- BHADESHIA, H. K. D. H. & SVENSSON, L. E. (1993) Modelling the evolution of microstructure in steel weld metals, In: Cerjak, H. and Easterling, K.E., eds. *Mathematical Modelling of Weld Phenomena*. London, Institute of Materials, 109-182
- BRETT, S. J. (1994) Cracking experience in steam pipework welds in national power. *VGB Conf. on Materials and Welding Technology in Power Plants*. Essen, Germany.
- BRETT, S. J. (2004) Type IIIa cracking in 1/2CrMoV steam pipework systems. *Science and Technology of Welding and Joining*, 9, 41-45.
- BRETT, S. J., BATES, J. S. & THOMSON, R. C. (2004) Aluminium nitride precipitation in low strength grade 91 power plant steels. In: Viswanathan, R., Gandy, D. and Koleman, K.,

eds. *Proceeding of 4th International Conference on Advances in Materials Technology for Fossil Power Plants*, EPRI. S. Carolina, USA, Electrical Power Research Institute (EPRI), 1183-1197

BRODY, H. D. & FLEMINGS, M. C. (1966) Solute redistribution in dendritic solidification. *Transactions of the AIME*, 236, 615.

BUCHMAYR, B., CERJAK, H., WITWER, M. & KIRKALDY, J. S. (1990) Carbon diffusion and microstructure in dissimilar Cr-Mo-V-Welds and their influence on the mechanical-properties. *Recent Trends in Welding Science and Technology*, *Twr*, 89, 237-242.

CERJAK, H. & LETOFSKY, E. (1998) The effect of welding on the microstructure development of advanced 9-12% Cr steels. In: Strang, A., Cawley, J. and Greenwood, G. W., eds. *International Conference on Microstructural Stability of Creep Resistant Alloys for High Temperature Plant Application*. London, The Institute of Materials, 323-337.

CHEN, C. & POLLACK, A. (1993) Influence of welding on steel weldment properties. IN OLSON, D. L. (Ed.) *ASM Hand Book*. ASM International, 416-428.

COLEMAN, M. C. (1981) Creep crack growth in a CrMoV throttle valve pressure vessel. In: Francois, D., eds. *Proceeding of 5th International Conference on Fracture*. Cannes, France, Pergamon Press, 1235-1244.

DAVID, S. A. & VITEK, J. M. (1989) Correlation between Solidification Parameters and Weld Microstructures. *International Materials Reviews*, 34, 213-245.

ENNIS, P. J. & CZYRSKA-FILEMONOWICZ, A. (2003) Recent advances in creep-resistant steels for power plant applications, *Sadhana-academy Proceedings in Engineering Science*, 28 (3-4), 709-730.

ENNIS, P. J., ZIELINSKA-LIPIEC, A. & CZYRSKA-FILEMONOWICZ, A. (1998) Quantitative comparison of the microstructures of high chromium steels for advanced power stations. In: Strang, A., Cawley, J. and Greenwood, G. W., eds. *International Conference on Microstructural Stability of Creep Resistant Alloys for High Temperature Plant Application*. London, The Institute of Materials, 135-143.

EVANS, H. E. (1984) *Mechanisms of Creep Fracture*, London and New York, Elsevier Applied Science Publisher.

EVANS, R. W. & WILSHIRE, B. (1985) *Creep of Metals and Alloys*, London, The Institute of Metals.

- EVANS, R. W. & WILSHIRE, B. (1993) *Introduction to Creep*, London, The Institute of Materials.
- FLEMINGS, M. C., MEHRABIAN & NEREO, G. E. (1968) Macrosegregation .2. *Transactions of the Metallurgical Society of AIME*, 242, 41-&.
- FLEMINGS, M. C. & NEREO, G. E. (1967) Macrosegregation .1. *Transactions of the Metallurgical Society of AIME*, 239, 1449-&.
- FOLDYNA, V., JAKOBOVA, A., RIMAN, R. & GEMPERLE, A. (1991) Effect of structural factors on the creep-properties of modified chromium Steels. *Steel Research*, 62, 453-458.
- FOLDYNA, V., PURMENSKY, J. & KUBON, Z. (1996) Development of advanced 9-12% Cr creep resistant steels with respect to structural stability. In: Earthman J.C. and Mohamed F.A., eds. *7th International Conference on Creep and Fracture of Engineering Materials and Structures*, Canada, Minerals, Metals & Materials Soc., 587-597.
- FORET, R., MILLION, B., SVOBODA, M. & STRANSKY, K. (2001) Structural stability of dissimilar weld joints of steel P91. *Science and Technology of Welding and Joining*, 6, 405-411.
- FORET, R., ZLAMAL, B. & SOPOUSEK, J. (2006) Structural stability of dissimilar weld between two Cr-Mo-V steels - Results are presented of an experimental study and modeling of the structural stability of 6Cr-Mo-V 8-3-2 and X12Cr-Mo-Nb 10-1 steels in a temperature interval from 600 degrees to 900 degrees C. *Welding Journal*, 85, 211S-217S.
- FRANCIS, J. A., MAZUR, W. & BHADSHIA, H. (2004) Estimation of type IV cracking tendency in power plant steels. *ISIJ International*, 44, 1966-1968.
- FREDRIKSSON, H. (1976) Segregation phenomena in iron-base alloys. *Scandinavian Journal of Metallurgy*, 5, 27-32.
- FUJIBAYASHI, S., KAWANO, K., KOMAMURA, T. & SUGIMURA, T. (2004) Creep behavior of 2.25Cr-1Mo steel shield metal arc weldment. *ISIJ International*, 44, 581-590.
- FUJIYAMA, K., KIMURA, K., MURAMATSU, M. & YAMADA, M. (1990) Evaluation of Creep-Properties of Degraded Cr-Mo-V Turbine Cast Steels through Hardness Measurement and Its Application to Life Assessment. *ISIJ International*, 30, 869-874.
- GAFFARD, V., GOURGUES-LORENZON, A. F. & BESSON, J. (2005) High temperature creep flow and damage properties of the weakest area of 9Cr1Mo-NbV martensitic steel weldments. *ISIJ International*, 45, 1915-1924.

- GARRISON, W. & BUCK, R. F. (1999) An overview of the development of advanced 9-12% Cr steels. *ASM Symposium on Materials for Rotating Machinery*. Cincinnati.
- GIAMEI, A. F., KRAFT, E. H. & LEMKEY, F. D. (1976) *New Trends in Materials Processing*, ASM, Metals Park, OH, 48-97.
- GLADMAN, T. (1998) Principles of microstructural stability in creep resistant alloys. In: Strang, A., Cawley, J. and Greenwood, G. W., eds. *International Conference on Microstructural Stability of Creep Resistant Alloys for High Temperature Plant Applications*, London, The Institute of Materials, 49-68.
- GOCMEN, A., UGGOWITZER, P. J., SOLENTHALER, C., SPEIDEL, M. O. & ERNST, P. (1998) Alloy design for creep resistant martensitic 9-12% chromium steels, In: Strang, A., Cawley, J. and Greenwood, G. W., eds. *International Conference on Microstructural Stability of Creep Resistant Alloys for High Temperature Plant Application*, London, The Institute of Materials, 311-322.
- GOOCH, D. J. & KING, B. L. (1978) High temperature crack propagation in 2.25Cr1Mo MMA weld metals. *Weldments, Physical Metallurgy and Failure Phenomena*. N.Y., Bolton Landing, 393-408.
- HAARMANN, K., VAILLANT, J. C., VANDENBERGHE, B., BENDICK, W. & ARBAB, A. (2002) *The T91/P91 Book*, Vallourec & Mannesmann Tubes.
- HALD, J. & STRAUB, S. (1998) *Materials for Advanced Power Engineering*, Julich, Forschungszentrum Julich GmbH, 155-&
- HAYASHI, T., KOJIMA, T. & MINAMI, Y. (1999) Development of 12% Cr heat resistant steel plate. In: Viswanathan, R. and Nutting, J., eds. *Advanced Heat Resistant Steel for Power Generation*, London, The Institute of Materials, 51-64
- HYDE, T. H. & SUN, W. (2005) A study of anisotropic creep behaviour of a 9CrMoNbV weld metal using damage analyses with a unit cell model. *Proceedings of the Institution of Mechanical Engineers Part L-Journal of Materials-Design and Applications*, 219, 193-206.
- HYDE, T. H., SUN, W., AGYAKWA, P. A., SHIPWAY, P. H. & WILLIAMS, J. A. (2003) Anisotropic creep and fracture behaviour of a 9CrMoNbV weld metal at 650 degrees C. *Anisotropic Behaviour of Damaged Materials*, 9, 295-316.
- HYDE, T. H., SUN, W., BECKER, A. A. & WILLIAMS, J. A. (2004) Creep properties and failure assessment of new and fully repaired P91 pipe welds at 923 K. *Proceedings of the Institution of Mechanical Engineers Part L-Journal of Materials-Design and Applications*, 218, 211-222.

- ISSLER, S., KLENK, A., SHIBLI, A. A. & WILLIAMS, J. A. (2004) Weld repair of ferritic welded materials for high temperature application. *International Materials Reviews*, 49, 299-324.
- KANEKO, R., NAKAMURA, S., WATANABE, Y., TANAKA, Y. & FUJITA, T. (1995) *Therm. Nucl. Power*, 46, 968.
- KASATKIN, B. S. & TSARYUK, A. K. (1967) Formation of Fusion Boundary Structure in Welded Joints. *Automatic Welding Ussr*, 20, 20-&.
- KLUEH, R. L. (2005) Elevated temperature ferritic and martensitic steels and their application to future nuclear reactors. *International Materials Reviews*, 50, 287-310.
- KLUEH, R. L. & BLOOM, E. E. (1985) The development of ferritic steels for fast induced-radioactivity decay for fusion-reactor applications. *Nuclear Engineering and Design-Fusion*, 2, 383-389.
- KOHLHOFER, W. & PENNY, R. K. (1996) Hardness testing as a means for creep assessment. *International Journal of Pressure Vessels and Piping*, 66, 333-339.
- KOU, S. (1987) *Welding Metallurgy*, New York, John Wiley & Sons.
- KOZESCHNIK, E., POLT, P., BRETT, S. & BUCHMAYR, B. (2002) Dissimilar 2.25Cr/9Cr and 2Cr/0.5CrMoV steel welds - Part 1: Characterisation of weld zone and numerical simulation. *Science and Technology of Welding and Joining*, 7, 65-68.
- KRUZ, W. & FISHER, D. J. (1989) *Fundamentals of Solidification*, Switzerland, Trans Tech Publications.
- KUBON, Z., FOLDYNA, V. & VODAREK, V. (1998) Analysis of strengthening mechanisms in 9 to 12% chromium steels. In: Strang, A., Cawley, J. and Greenwood, G. W., eds. *International Conference on Microstructural Stability of Creep Resistant Alloys for High Temperature Plant Applications*, London, The Institute of Materials, 257-269.
- KUCERA, J., MILLION, B. & STRANSKY, K. (1985) Stationary and quasi-stationary models of carbon redistribution in austenitic steel weldments, 1. Ternary-Systems. *Czechoslovak Journal of Physics*, 35, 1355-1361.
- LAGNEBORG, R. (1979) *Creep Deformation Mechanisms*, London, Applied Science Publisher.
- LAHA, K., CHANDRAVATHI, K. S., RAO, K. B. S., MANNAN, S. L. & SASTRY, D. H. (2001a) An assessment of creep deformation and fracture behavior of 2.25Cr-1Mo similar

and dissimilar weld joints. *Metallurgical and Materials Transactions a-Physical Metallurgy and Materials Science*, 32, 115-124.

LAHA, K., LATHA, S., RAO, K. B. S., MANNAN, S. L. & SASTRY, D. H. (2001b) Comparison of creep behaviour of 2 center dot 25Cr-1Mo/9Cr-1Mo dissimilar weld joint with its base and weld metals. *Materials Science and Technology*, 17, 1265-1272.

LANCASTER, J. F. (1993) *Metallurgy of Welding*, London, Chapman & Hall.

LUNDIN, C. D. (1982) Dissimilar metal welds - transition joints literature-review. *Welding Journal*, 61, S58-S63.

MANNAN, S. L. & LAHA, K. (1996) Creep behaviour of Cr-Mo steel weldments. *Transactions of the Indian Institute of Metals*, 49, 303-320.

MARUYAMA, K., SAWADA, K. & KOIKE, J. (2001) Strengthening mechanisms of creep resistant tempered martensitic steel. *ISIJ International*, 41, 641-653.

MASUYAMA, F. (1999) New developments in steels for power generation boilers. In: Viswanathan, R. and Nutting, J., eds. *Advanced Heat Resistant Steel for Power Generation*. London, IOM Communications Ltd, 33-48.

MAYER, K. H., BENDICK, W., HUSEMANN, R. U., KERN, T.-U. & SCARLIN, R. B. (1998) New materials for improving the efficiency of fossil-fired thermal power station. *International Joint Power Generation Conference*. PWR-Vol33, ASME, 831-841

MESSLER, R. W. (1999) *Principles of Welding: Processes, Physics, Chemistry, and Metallurgy*, New York, John Wiley & Sons.

MILLION, B., BACILEK, K., KUCERA, J., MICHALICKA, P., REK, A. & STRANSKY, K. (1995) Carbon Diffusion and Thermodynamic Characteristics in Chromium Steels. *Zeitschrift Fur Metallkunde*, 86, 706-712.

NAWROCKI, J. G., DUPONT, J. N. & MARDER, A. R. (2000) A study on the carbide precipitation in a ferritic steel. In: Williams, D.B. and Shimizu, R., eds. *Proceedings of Microbeam Analysis 2000*, IOP Publishing, 175-176.

NUTTING, J. (1999) The structural stability of low alloy steels for power generation applications. In: Viswanathan, R. and Nutting, J., eds. *Advanced Heat Resistant Steels for Power Generation*, London, IOM Communications Ltd, 12-30.

- OKADA, H., MUNEKI, S., YAMADA, K., OKUBO, H., IGARASHI, M. & ABE, F. (2002) Effects of alloying elements on creep properties of 9Cr-3.3W-0.5Pd-V, Nb, N, B steels. *ISIJ International*, 42, 1169-1174.
- ORLOVA, A., BURSIK, J., KUCHAROVA, K. & SKLENICKA, V. (1998) Microstructural development during high temperature creep of 9% Cr steel. *Materials Science and Engineering a-Structural Materials Properties Microstructure and Processing*, 245, 39-48.
- PARK, K. S., CHUNG, H. S., LEE, K. J., JUNG, Y. G., KANG, C. Y. & ENDO, T. (2005) Effect of hardness changes and microstructural degradation on creep behavior of a Mod.9Cr-1Mo steel. *International Journal of Automotive Technology*, 6, 45-52.
- PILOUS, V. & STRANSKY, K. (1998) *Structural Stability of Deposits and Welded Joints in Power Engineering*, Cambridge International Science Publishing.
- PORTER, D. A., EASTERLING, K. E., (1992) *Phase transformations in metals and alloys*, London, Chapman & Hall.
- RAJ, S. V. & PHARR, G. M. (1986) A Compilation and Analysis of Data for the Stress Dependence of the Subgrain Size. *Materials Science and Engineering*, 81, 217-237.
- SANCHEZ-HANTON, J., THOMSON, R. C. & BRETT, S. J. (2008) The role of AlN on the microstructural evolution of ex-service P91 steel. In: Coleman, K. & Gandy, D., eds. *EPRI Workshop on Grade 91/92 Steels 2008*. Florida, USA, Electrical Power Research Institute (EPRI).
- SATO, M., HASEGAWA, Y., MURAKI, T. & MARUYAMA, K. (2000) Correlation between creep strength and stability of subgrain structure in high chromium ferritic heat resistant steel with tungsten. *Journal of the Japan Institute of Metals*, 64, 371-374.
- SAVAGE, W. F. (1978) Solidification, segregation and weld defects. In: Christoffel, R. J., Nipples, E.F., Solomon, H.D., eds. *Weldments: Physical Metallurgy and Failure Phenomena, Proc. of the 5th Bolton Landing Conference*. General Electric, Schenectady, NY, 1-18.
- SAVAGE, W. F., NIPPES, E. F. & SZEKERES, E. S. (1976) Study of weld interface phenomena in a low-alloy steel. *Welding Journal*, 55, S260-S268.
- SAWADA, K., TAKEDA, M., MARUYAMA, K., ISHII, R., YAMADA, M., NAGAE, Y. & KOMINE, R. (1999) Effect of W on recovery of lath structure during creep of high chromium martensitic steels. *Materials Science and Engineering a-Structural Materials Properties Microstructure and Processing*, 267, 19-25.

- SCHULLER, H. J., HAGN, L. & WOITSCHECK, A. (1974) Cracking in the weld region of shaped components in hot steam pipe lines. *Materials Investigation*, 47, P. 1.
- SCHWIND, M., HATTESTRAND, M. & ANDREN, H. O. (1998) High resolution microanalysis of ferritic steel HCM12A. *In: Strang, A., Cawley, J. and Greenwood, G. W., eds. International Conference on Microstructural stability of creep resistant alloys for high temperature plant applications*, London, The Institute of Materials, 197-213.
- SMITH, C. S. (1948) Grains, phases, and interfaces: an interpretation of microstructure. *Transactions of the AIME*, 175, 15.
- SOPOUSEK, J. & FORET, R. (2008) More sophisticated thermodynamic designs of welds between dissimilar steels. *Science and Technology of Welding and Joining*, 13, 17-24.
- SOPOUSEK, J., FORET, R. & JAN, V. (2004) Simulation of dissimilar weld joints of steel P91. *Science and Technology of Welding and Joining*, 9, 59-64.
- SOURMAIL, T. (2001) Precipitation in creep resistant austenitic stainless steels. *Materials Science and Technology*, 17, 1-14.
- SPIGARELLI, S. & QUADRINI, E. (2002) Analysis of the creep behaviour of modified P91 (9Cr-1Mo-NbV) welds. *Materials & Design*, 23, 547-552.
- STARK, J. P. (1980) An Approximate Analytical Demonstration of the Famous Darken Experiment. *Metallurgical Transactions A-Physical Metallurgy and Materials Science*, 11, 1797-1798.
- STEFANESCU, D. M. (2002) *Science and Engineering of Casting Solidification*, NY, Kluwer Academic / Plenum Publishers.
- STRANG, A. & VODAREK, V. (1998) Microstructural stability of creep resistant martensitic 12% Cr steels. *In: Strang, A., Cawley, J. and Greenwood, G. W., eds. International Conference on Microstructural Stability of Creep Resistant Alloys for High Temperature Plant Applications*, London, The Institute of Materials, 117-133.
- SUDHA, C., TERRANCE, A. L. E., ALBERT, S. K. & VIJAYALAKSHMI, M. (2002) Systematic study of formation of soft and hard zones in the dissimilar weldments of Cr-Mo steels. *Journal of Nuclear Materials*, 302, 193-205.
- TAMURA, M., SAKASEGAWA, H., KOHYAMA, A., ESAKA, H. & SHINOZUKA, K. (2003) Effect of MX type particles on creep strength of ferritic steel. *Journal of Nuclear Materials*, 321, 288-293.

- TANAKA, H., MURATA, M., ABE, F. & IRIE, H. (2001) Microstructural evolution and change in hardness in type 304H stainless steel during long-term creep. *Materials Science and Engineering A-Structural Materials Properties Microstructure and Processing*, 319, 788-791.
- TILLER, W. A., JACKSON, K. A., RUTTER, J. W. & CHALMERS, B. (1953) The redistribution of solute atoms during the solidification of metals. *Acta Metallurgica*, 1, 428.
- TILLER, W. A. & RUTTER, J. W. (1956) The effect of growth conditions upon the solidification of a binary alloy. *Canadian Journal of Physics*, 33, 723.
- VISWANATHAN, R. & BAKKER, W. (2001) Materials for ultrasupercritical coal power plants-boiler materials: Part 1. *Journal of Materials Engineering and Performance*, 10, 81-95.
- VISWANATHAN, R. & BAKKER, W. T. (2000) Materials for boilers in ultra supercritical power plant. Proceedings of *2000 International Joint Power Generation Conference*. Miami Beach, Florida, ASME, 1-22.
- VISWANATHAN, R., COLEMAN, K. & RAO, U. (2006) Materials for ultra-supercritical coal-fired power plant boilers. *International Journal of Pressure Vessels and Piping*, 83, 778-783.
- VODAREK, V. & STRANG, A. (2000) Compositional changes in minor phases present in 12CrMoVNb steels during thermal exposure at 550 degrees C and 600 degrees C. *Materials Science and Technology*, 16, 1207-1213.
- WATANABE, T., TABUCHI, M., YAMAZAKI, M., HONGO, H. & TANABE, T. (2006) Creep damage evaluation of 9Cr-1Mo-V-Nb steel welded joints showing Type IV fracture. *International Journal of Pressure Vessels and Piping*, 83, 63-71.
- WATANABE, T., YAMAZAKI, M., HONGO, H., TABUCHI, M. & TANABE, T. (2004) Effect of stress on microstructural change due to aging at 823 K in multi-layer welded joint of 2.25Cr-1Mo steel. *International Journal of Pressure Vessels and Piping*, 81, 279-284.
- CALLISTER, W.D., JR., (1997) *Materials Science and Engineering: An Introduction*, Cannada, John Wiley & Sons.
- WU, R., SANDSTROM, R. & SEITISLEAM, F. (2004) Influence of extra coarse grains on the creep properties of 9 percent CrMoV (P91) steel weldment. *Journal of Engineering Materials and Technology-Transactions of the ASME*, 126, 87-94.

YIN, Y. F. & FAULKNER, R. G. (2005) Creep damage and grain boundary precipitation in power plant metals. *Materials Science and Technology*, 21, 1239-1246.

YOU, Y. Y., SHIUE, R. K., SHIUE, R. H. & CHEN, C. (2001) The study of carbon migration in dissimilar welding of the modified 9Cr-1Mo steel. *Journal of Materials Science Letters*, 20, 1429-1432.

ZHANG, Y., SHIPWAY, P. H., HYDE, T. H. & SUN, W. (2007) Anisotropic creep behaviour of P91 weld Metal - a microstructural study. In: Allen, D.J., et al. eds. *Proceedings of 3rd Intl. Conf. on Integrity of High Temperature Welds*. London, UK, IOM Communications Ltd., 373-388.